DEVELOPMENT OF MICROANALYTICAL METHODS FOR SOLVING SAMPLE LIMITING BIOLOGICAL ANALYSIS PROBLEMS

by

EVE C. METTO

B.Ed., Egerton University, 2001

AN ABSTRACT OF A DISSERTATION

submitted in partial fulfillment of the requirements for the degree

DOCTOR OF PHILOSOPHY

Department of Chemistry
College of Arts and Sciences

KANSAS STATE UNIVERSITY
Manhattan, Kansas

2013

Abstract

Analytical separations form the bulk of experiments in both research and industry. The choice of separation technique is governed by the characteristics of the analyte and purpose of separation. Miniaturization of chromatographic techniques enables the separation and purification of small volume samples that are often in limited supply. Capillary electrophoresis and immunoaffinity chromatography are examples of techniques that can be easily miniaturized with minimum loss in separation efficiency. These techniques were used in the experiments presented in this dissertation. Chapter 1 discusses the underlying principles of capillary electrophoresis and immunoaffinity chromatography.

In the second chapter, the results from immunoaffinity chromatography experiments that utilized antibody-coated magnetic beads to purify serine proteases and serine protease inhibitors (serpins) from *A. gambiae* hemolymph are presented and discussed. Serine proteases and serpins play a key role in the insect innate immunity system. Serpins regulate the activity of serine proteases by forming irreversible complexes with the proteases. To identify the proteases that couple to these serpins, protein A magnetic beads were coated with SRPN2 antibody and then incubated with *A. gambiae* hemolymph. The antibody isolated both the free SRPN2 and the SRPN2-protease complex. The purified proteases were identified by ESI-MS from as few as 25 insects.

In Chapter 3, an integrated glass/PDMS hybrid microfluidic device was utilized for the transportation and lysis of cells at a high throughput. Jurkat cells were labeled with 6-CFDA (an internal standard) and DAF-FM (a NO specific fluorophore). Laser-induced fluorescence (LIF) detection was utilized to detect nitric oxide (NO) from single Jurkat cells. The resulting

electropherograms were used to study the variation in NO production following stimulation with lipopolysaccharide (LPS). 3 h LPS-stimulation resulted in a two fold increase in NO production in both bulk and single cell analysis. A comparison of bulk and single cell NO measurements were performed and the average NO production in single cells compared well to the increase measured at the bulk cell level.

Chapter 4 discusses the preliminary experiments with a T-shaped microfluidic device that exploit the property of poly(dimethylsiloxane) (PDMS) as an electroactive polymer (EAP), to enhance fluid mixing. EAPs deform when placed in an electric field. A thin layer of PDMS was sandwiched between chrome electrodes, positioned on the horizontal arms of the T design, and the electrolyte-filled fluidic channel. A potential difference across the PDMS layer caused it to shrink and stretch, thereby increasing the channel volume. The electrodes were actuated at 180^{o} out of phase and this caused the fluid stream in the vertical channel to fold and stretch resulting in enhanced contact surface area and shorter diffusion distances of the fluid, thereby improving mixing efficiency.

All the experiments presented in this dissertation demonstrate the application of miniaturized chromatographic techniques for the efficient analysis of small volume biological samples.

DEVELOPMENT OF MICROANALYTICAL METHODS FOR SOLVING SAMPLE LIMITING BIOLOGICAL ANALYSIS PROBLEMS

by

EVE C. METTO

B.Ed., Egerton University, 2001

A DISSERTATION

submitted in partial fulfillment of the requirements for the degree

DOCTOR OF PHILOSOPHY

Department of Chemistry
College of Arts and Sciences

KANSAS STATE UNIVERSITY
Manhattan, Kansas

2013

Approved by:

Major Professor
Christopher T. Culbertson

Abstract

Analytical separations form the bulk of experiments in both research and industry. The choice of separation technique is governed by the characteristics of the analyte and purpose of separation. Miniaturization of chromatographic techniques enables the separation and purification of small volume samples that are often in limited supply. Capillary electrophoresis and immunoaffinity chromatography are examples of techniques that can be easily miniaturized with minimum loss in separation efficiency. These techniques were used in the experiments presented in this dissertation. Chapter 1 discusses the underlying principles of capillary electrophoresis and immunoaffinity chromatography.

In the second chapter, the results from immunoaffinity chromatography experiments that utilized antibody-coated magnetic beads to purify serine proteases and serine protease inhibitors (serpins) from *A. gambiae* hemolymph are presented and discussed. Serine proteases and serpins play a key role in the insect innate immunity system. Serpins regulate the activity of serine proteases by forming irreversible complexes with the proteases. To identify the proteases that couple to these serpins, protein A magnetic beads were coated with SRPN2 antibody and then incubated with *A. gambiae* hemolymph. The antibody isolated both the free SRPN2 and the SRPN2-protease complex. The purified proteases were identified by ESI-MS from as few as 25 insects.

In Chapter 3, an integrated glass/PDMS hybrid microfluidic device was utilized for the transportation and lysis of cells at a high throughput. Jurkat cells were labeled with 6-CFDA (an internal standard) and DAF-FM (a NO specific fluorophore). Laser-induced fluorescence (LIF) detection was utilized to detect nitric oxide (NO) from single Jurkat cells. The resulting

electropherograms were used to study the variation in NO production following stimulation with lipopolysaccharide (LPS). 3 h LPS-stimulation resulted in a two fold increase in NO production in both bulk and single cell analysis. A comparison of bulk and single cell NO measurements were performed and the average NO production in single cells compared well to the increase measured at the bulk cell level.

Chapter 4 discusses the preliminary experiments with a T-shaped microfluidic device that exploit the property of poly(dimethylsiloxane) (PDMS) as an electroactive polymer (EAP), to enhance fluid mixing. EAPs deform when placed in an electric field. A thin layer of PDMS was sandwiched between chrome electrodes, positioned on the horizontal arms of the T design, and the electrolyte-filled fluidic channel. A potential difference across the PDMS layer caused it to shrink and stretch, thereby increasing the channel volume. The electrodes were actuated at 180^{o} out of phase and this caused the fluid stream in the vertical channel to fold and stretch resulting in enhanced contact surface area and shorter diffusion distances of the fluid, thereby improving mixing efficiency.

All the experiments presented in this dissertation demonstrate the application of miniaturized chromatographic techniques for the efficient analysis of small volume biological samples.

Table of Contents

List of Figures

List of Tables

Acknowledgements

I would like to thank the department of Chemistry, Kansas State University, for offering me admission to the Chemistry graduate program and supporting me as a Graduate Teaching Assistant in my first two years at Kansas State in which I gained valuable experience in teaching practical chemistry. Thank you for the grants and scholarships that comfortably saw me through the graduate program.

Christopher Culbertson, thank you for the precious opportunity you gave me to work in your group. For the 5 years I worked with you, I have grown exponentially in my knowledge in analytical chemistry. Thanks for all the opportunities you provided. Thanks to the Culbertson group members, past and present, who have made the lab a fun place to work in. Thanks Scott and Alex, for helping me get comfortable with the instruments in the lab. The discussions on exotic cuisines from all parts of the world; Nepal, Kenya, Sri Lanka, Eritrea and USA did not always make me hungry but surely spiced the mood…

To the ladies at the Chemistry Department office; Mary, Donna, Connie, Kim, Lisa, Earline, it was wonderful knowing and working with you. To the gentlemen at the technical workshops and storeroom, Tobbe, Ralph, Ron and Jim, thanks for all your help.

I would also like to thank Dr. Kristin Michel and Prof. Mike Kanost for allowing me to work in their labs and for providing direction and ideas with the insect hemolymph experiments. I am particularly grateful to their post doctoral fellows: Drs. Maurine Gorman, Neil Dittmer, Xin Zhang and Di Wu, for training me in hemolymph collection and routine biochemistry procedures (SDS-PAGE, gel staining, etc) and all the helpful discussions we had.

My dear friends, Janet and Pernilla, my big sissies, thanks for all your love and friendship.

My dear husband David, thanks for being there for me and urging me on. *Tumetoka mbali.* My sisters, Natalie, Barbara, Judith and Maryanne, thanks for all the calls, messages and for being my best friends. Cousin Mark and Flo, I appreciate all your help in getting me settled in USA. Mum and dad, I never take for granted all the sacrifices you made for us to have a decent life and education. God bless you abundantly.

Last but certainly not least, I would like to thank my families, *Kap Mukunya* and *Kap Tapkure* for all the love, prayers and support.

Dedication

Salina and Paul, the best parents in the world.

Chapter 1 - Introduction

1.1 Analytical Separations

Most experiments and procedures performed in chemical laboratories, both in research and industry involve isolation and purification of chemical or biological compounds. The choice of separation method used is governed by the characteristics of the species to be separated. Many separation techniques are available including distillation, high- and ultra- performance liquid chromatography (HPLC and UPLC), gas chromatography, electrophoresis, solvent phase extraction, affinity chromatography and gas chromatography (GC). Thermodynamics and transport phenomena are the main principles underlying the separation mechanisms.[1] Chromatographic techniques are usually carried out in a column packed with a stationary phase. The sample mixture, dissolved in a mobile phase, is then applied at the head of the column and forced through the packed column. Individual components in the sample mixture interact with the stationary phase with varying affinities, and as a consequence, some components get retarded by the stationary phase longer than others, resulting in a separation. Fluid transport in chromatographic columns is achieved by pressure driven flow.

Affinity chromatography is a unique type of chromatography that generally exploits biological interactions in separating out specific species from often complex matrices. These interactions may be mono-specific or group-specific. Mono-specific interactions include antibody-antigen and enzyme-substrate interactions where only one species is recognized by the ligand. On the other hand, group-specific interactions involve interactions of more than one species that have strong affinity for the same ligand. An example of such an interaction is lectin affinity for sugar groups in different biomolecules.[1] More details on the mechanism of affinity chromatography will be discussed later in this chapter. In chapter 2, I will discuss experiments

that utilized immunoaffinity chromatography to isolate and identify proteins involved in the innate immune response system of *Manduca sexta* and *Anopheles gambiae.* Antibodies against the proteins of interest were immobilized onto a stationary phase that was then used to isolate the desired proteins from insect hemolymph samples. The isolated proteins were then analyzed with sodium dodecyl sulphate- (poly) acrylamide gel electrophoresis (SDS-PAGE) and mass spectrometry.

Capillary electrophoresis (CE) is another separation technique capable of very high separation efficiency of small volume samples. Further, CE can be utilized on microfluidic devices, which greatly reduces analysis times thanks to the scaled-down dimensions of these devices. Sample volumes equivalent to that of a single mammalian cell can be routinely analyzed on these devices. In CE, ionic analytes are separated based on their charge to hydrodynamic drag ratio. The plug flow profile generated by electroosmosis plays a significant role in minimizing analyte band broadening, and this makes CE a powerful tool in the separation and analysis of samples at low concentrations. In chapter 3, the study of nitric oxide expression from single mammalian cells will be discussed. The experiments utilized an improved microfluidic device to transport and lyse cells and subsequently electrophoretically analyze the lysate in a separation channel. Laser induced fluorescence (LIF) was used to detect the fluorescently labeled NO from the cell lysate. In chapter four, the use of poly(dimethylsiloxane) (PDMS) as a dielectric elastomer is exploited in designing a micromixing device. Preliminary results of these experiments will be discussed.

1.2 Fluid Transport in Capillaries and Microfluidic Devices

Fluid flow in microfluidic devices and capillaries is accomplished by either of two means; electroosmotic flow or pressure-driven flow with the former preferred for microfluidic devices.[2]

1.2.1 Electroosmotic Flow

The surface of a fused silica capillary possesses a net negative charge when in contact with an aqueous solution. The charged surface contains silanol groups that are ionized at pH > 2, giving rise to an electric double layer. The inner layer, also called compact, Helmholtz or Stern layer, is comprised of immobile cations that are strongly adsorbed onto the surface of fused silica. An imaginary plane parallel to the capillary surface and cutting across the innermost adsorbed cations is called the inner Helmholtz plane. The outer Helmholtz plane (OHP) is the imaginary line that consists of hydrated immobile ions adjacent to the inner Helmholtz plane. A second more diffuse layer consists of hydrated mobile cations that neutralize the residual negative charges. The diffuse layer lies between the OHP and the bulk liquid neutral. The region between these two layers is called the slipping plane. Figure 1.1 is an illustration of the electric double layer. The electrostatic potential across the diffuse double layer is referred to as the zeta potential, ζ. In the presence of an electric field applied parallel to the surface of the channel, the ions in the diffuse layer are attracted towards the oppositely charged electrode. In this process, these solvated ions drag with them the bulk fluid of the buffer due to viscous forces, resulting in a pumping action called *electroosmosis*. The electroosmotic velocity, v_{eo} is determined by the Smoluchowski equation (Equation 1.1)[2]

$$\boldsymbol{v_{eo} = -\frac{\varepsilon\zeta}{\eta}E = \mu_{eo}E} \qquad \textbf{(1.1)}$$

Where ε is the permittivity of the solution, η is the viscosity, E is the field strength and μ_{eo} is the electroosmotic mobility. The negative sign is included because the surface charge on silica or glass is negative and movement of the positive ions is towards the cathode. Electroosmotic velocity is constant across the cross section of the channel and consequently, the fluid flow

profile is planar and perpendicular to the plane of the channel, (figure Figure 1.2). This is very advantageous in electrophoretic separations because band broadening is tremendously reduced.

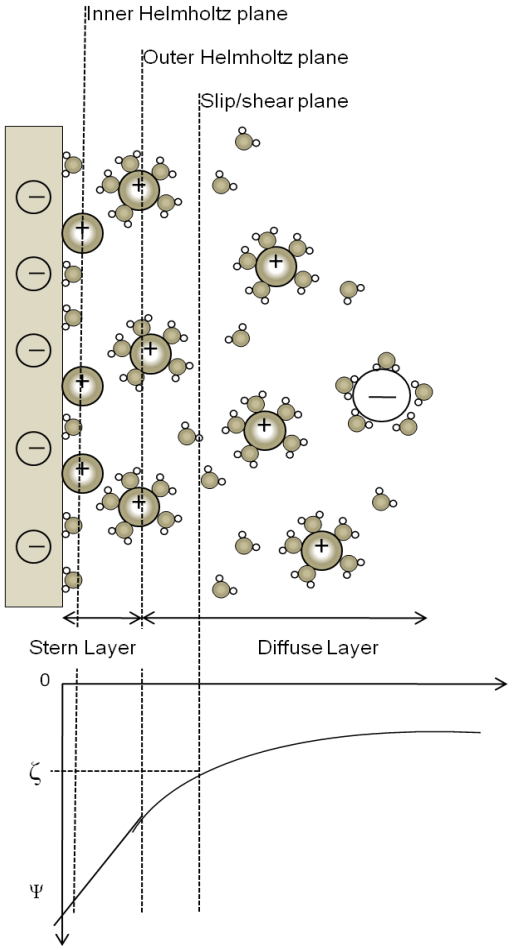

Figure 1.1. A schematic diagram of the electric double layer. Ψ is the potential due to the surface charge density and ζ is the potential across the diffuse layer.

1.2.2 Pressure Driven Flow

The application of pressure is another popular technique of inducing flow in capillaries and microfluidic devices. Fluid flow is maintained by a steady pressure difference between the inlet and outlet of the capillary tube.

When pressure is applied, the fluid accelerates to a point where the pressure forces, calculated by multiplying the cross sectional area by the pressure difference, are equal to the drag forces exerted by the capillary wall as shown in equation 1.2 below; [3]

$$\pi r_c^2 \triangle p = -2\pi r_c L\eta \left(\frac{dv}{dr}\right)_0 \qquad \textbf{(1.2)}$$

where r_c is the radius of the capillary, L is the length of the capillary over which pressure is applied, η is the viscocity. - $(dv/dr)_o$ is the shear rate on the capillary wall. The expression 1.2 above can be rearranged as follows;

$$-\left(\frac{dv}{dr}\right)_o = \frac{r_c \triangle p}{2L\eta} \qquad \textbf{(1.3)}$$

A similar treatment is applied to adjacent fluid layers that are imagined as cylinders with radii *r*. Equation 1.3 then becomes;

$$dv = \frac{-\triangle p r^2}{4L\eta} + const. \qquad \textbf{(1.4)}$$

At the capillary surface, $dv = 0$ and the value of the constant can be solved. Integration of equation 1.4 yields an expression that can be used to determine the velocity of the fluid at any point within the radius of the capillary (equation 1.5).

$$v = \frac{\Delta p}{4L\eta}(r_c^2 - r^2) \qquad \textbf{(1.5)}$$

At the center of the capillary, $r = 0$ and the velocity is maximum. Equation 1.5 then becomes;

$$v = \frac{\Delta p}{4L\eta} r_c^2 \qquad \textbf{(1.6)}$$

The average value of *v* is determined by integrating expression (1.6) above to botain;[2,3]

$$\langle v \rangle = \frac{v_{msx}}{2} = \frac{\Delta p}{8L\eta} r_c^2 \qquad \textbf{(1.7)}$$

The equations show that the fluid velocity in pressure driven flow is dependent on the distance from the wall of the capillary. The flow profile is parabolic with the highest fluid velocity at the

center of the capillary and lowest velocity at the capillary wall. Figure 1.2 shows a comparison between electroosmotic and pressure-driven flow profiles.

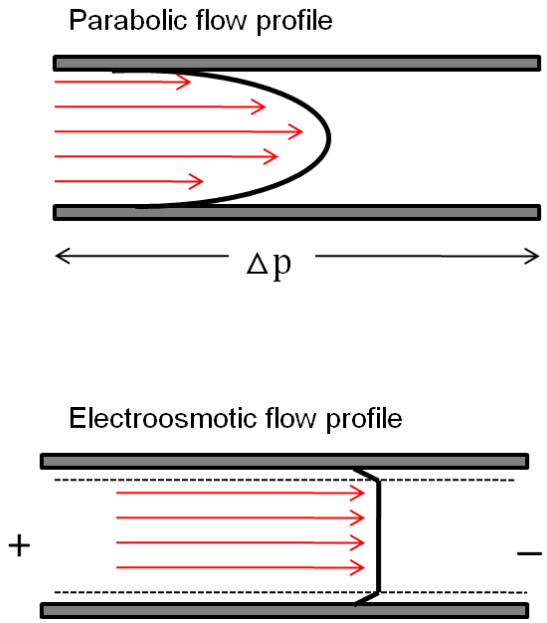

Figure 1.2. Schematic diagrams depicting parabolic flow profile due to pressure-driven flow (above) and 'plug' flow profile due to electroosmotic fluid transportation. The sizes of the red arrows represent the magnitude of fluid velocity at different regions in the capillary.

1.3 Electrophoretic Separations

Initial work in electrophoretic separations began in the 1930s with Arne Tiselius who separated serum proteins using a U-shaped container with electrodes at the openings.[4] One of the greatest challenges Tiselius encountered while performing his experiments was joule heating that induced convective currents, thus compromising the separation efficiency due to band broadening. Later, in the 60s, anti-convective gels were developed, leading to the well-established polyacrylamide gel electrophoresis utilized in the separation and quantification of proteins.[5-9] The voltage applied to these gels was greatly limited by joule heating which was difficult to dissipate. This challenge was overcome by the development of capillary electrophoresis, which was first demonstrated by Jorgensen in 1981.[10-12] The increased surface

area to volume ratio of the capillary ensured that heat was quickly and efficiently dissipated and this permitted the use of voltages as high as 30,000 V. The result was very high separation efficiencies limited only by diffusion. A more detailed discussion on separation efficiency is presented in section 1.4.

Electrophoretic separations are based on the velocity of an analyte ion in an electric field. Two types of forces affect ions in an electric field; electric force (F_{el}) and frictional force (F_{fr}), and they are calculated as follows;

$$\boldsymbol{F_{el} = qE = q\frac{V}{L}} \qquad \textbf{(1.8)}$$

$$\boldsymbol{F_{fr} = -6\pi\eta r v} \qquad \textbf{(1.9)}$$

Where q is the charge of the ion, E is the electric field, V is the voltage applied, L is the length of capillary, η is the fluid viscocity, r is the effective radius of the ion and v_{ep} the electrophoretic velocity. The frictional force has a negative sign because it acts in the opposite direction to the electrophoretic force. At a steady electrophoretic state, the two forces balance out and they can be equated.

$$\boldsymbol{qE = 6\pi\eta r v_{ep}} \qquad \textbf{(1.10)}$$

The electrophoretic velocity can then be expressed as follows;

$$\boldsymbol{v_{ep} = \frac{qE}{6\pi\eta r} = \mu_{ep} E} \qquad \textbf{(1.11)}$$

It is noted in the expression above that the electrophoretic mobility μ_{ep} is directly proportional to the charge density and inversely proportional to its effective hydrodynamic radius. Therefore a smaller molecule with higher charge density will have a higher mobility than a larger molecule with a lower charge density. The overall migration velocity of an analyte is the sum of the electrophoretic velocity and the electroosmotic velocity, discussed earlier (Equation 1.1), i.e.

$$v = \mu_{ep}E + \mu_{eo}E \qquad (1.12)$$

In most cases, $v_{eo} > v_{ep}$ and as a result, the net migration of the analytes is towards the cathode in the case of a fused silica capillary. Capillary electrophoresis is capable of very high separation efficiencies thanks to the plug flow profile generated by electroosmosis.

1.4 Separation Parameters

The ultimate goal in any chromatographic separation is to maximize the differential transport and minimize zone spreading/band broadening of the separated species. The 'goodness' of a separation is determined by the following separation efficiency parameters; plate height, plate number, resolution and peak capacity. All these parameters are influenced by band broadening. The band broadening process arises from stochastic events that can be statistically described. The molecules in a band undergo successive displacement in different directions resulting in an initially narrow band spreading outward, to produce a Gaussian concentration profile.[3] The standard deviation, σ is equal to the distance from the center of the Gaussian profile to the point of inflection and the base width is approximately 4σ (Figure 1.3). The variance, σ^2 is simply the standard deviation squared. Because diffusion is the result of the random movement of molecules, the spreading of a narrow band of molecules will evolve into a Gaussian shaped concentration band. The relationship between the width of the band and the time over which diffusion is occurs is given by the Einstein-Smoluchowski equation below;

$$\sigma^2 = 2Dt \qquad (1.13)$$

where D is the diffusion coefficient and t is time.

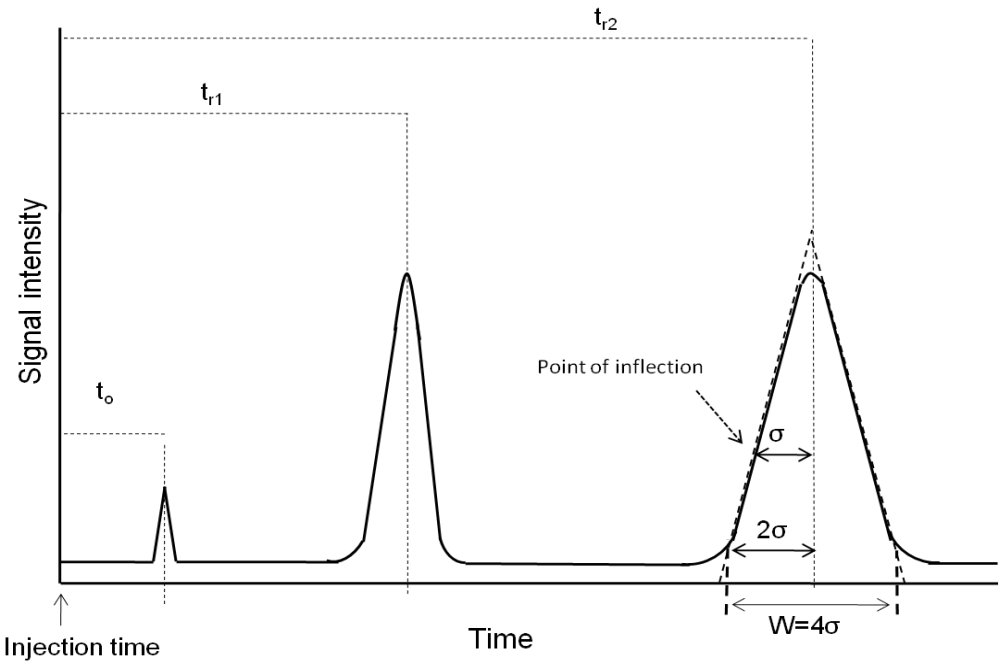

Figure 1.3. A typical electrochromatogram with important parameters indicated. t_o is the retention time of an unretained component while t_{r1} and t_{r2} are the retention times of the least retained and the most retained components respectively. The width of the base of the peak (W) is equivalent to four times the standard deviation of the Gaussian peak.

1.4.1 Plate Height and Plate Number

Plate height (*H*) and plate number (*N*) are commonly used to describe and quantify the efficiency of a chromatographic separation. These are hypothetical terms and have their origin in distillation columns that contained plates to enhance separation efficiency. The theoretical plates are imaginary regions where equillibrium is achieved after analytes move from one phase to another (e.g. mobile phase to stationalry phase). The more these plates are, the better the separation efficiency. Plate height is the distance between two adjacent theoretical plates and for the same length of column, a smaller height means a more efficient separation. The two terms are related by the equation (1.14) below;

$$\boldsymbol{H = \frac{L}{N}} \qquad \textbf{(1.14)}$$

where *L* is the column length between the injection point and the detection window.

The term *t* in equation (1.13) can be written in terms of *L* and peak velocity *u*. Substituting *t* in equation (1.13) with *L/u* and diving both sides of the equation with *L*, we get an expression for plate height as shown below;

$$\boldsymbol{H = \frac{\sigma^2}{L} = \frac{2D}{u}} \qquad \textbf{(1.15)}$$

The variance, σ^2, can be deduced from the base length of an analyte peak as shown in Figure 1.3. Equation (1.14) can then be rearranged to give the expression for *N*;

$$\boldsymbol{N = \frac{L}{H} = \frac{L^2}{\sigma^2}} \qquad \textbf{(1.16)}$$

Due the plug flow profile in electrophoresis-based separations, the value of *N* is orders of magnitude higher than other column chromatographic techniques.

In capillary electrophoresis, diffusion is the major source of band broadening, but there are other contributions which are summarized in equation 1.17 below.[2]

$$\boldsymbol{\sigma^2_{total} = \sigma^2_{diff} + \sigma^2_{inj} + \sigma^2_{det} + \sigma^2_{joule} + \sigma^2_{geo} + \sigma^2_{MT} + \sigma^2_{ads} + \sigma^2_{edisp} + \sigma^2_{flow}} \qquad \textbf{(1.17)}$$

The subscripts, beginning from the left are diffusion, injection plug length, detection window length, joule heating, geometry, mass transfer effects, adsorption, electrodispersion and laminar flow.

A sample cannot be added onto the capillary or on any chromatographic column as an infinitely thin band and the contribution to band width due to the sample injection plug is calculated as follows;

$$\boldsymbol{\sigma^2_{inj} = \frac{l^2_{inj}}{12}} \qquad \textbf{(1.18)}$$

where l_{inj} is the injection plug length. The contribution of σ_{inj} is trivial except in situations where very fast separations are performed such as on microfluidic devices.[2,13]

In detection systems that utilize lasers (LIF or UV), the length of the detection window is determined by the laser spot diameter or the size of the spatial filter aperture, depending on which of the two is larger. A larger filter aperture would mean that the whole laser beam spot

would define the detection window and since its intensity has a Gaussian distribution, then the variance contribution would be defined by equation (1.15) below;

$$\sigma_{det}^2 = \frac{l_{det}^2}{16} \qquad \textbf{(1.19)}$$

On the other hand, if the laser beam is larger than the aperture, then the dispersion is described by equation (1.17).[2]

Joule heating in capillaries and microfluidic devices arises from electrical energy being converted to heat energy when friction occurs from drag by caused current-conducting ion species. If the heat is poorly dissipated, a temperature gradient and in turn a viscosity gradient occurs in the column. This affects the electroosmotic mobility of ions during an electrophoretic separation (see equation 1.11) and therefore reduces the separation efficiency. Microfluidic devices made out of glass have better heat dissipation due to the large surface area to volume ratio of the channels compared to fused silica capillaries. Higher field strengths can be used on these devices with little contribution by joule heating to band broadening.[2] The devices used in this dissertation are a glass-poly(dimethyl) siloxane hybrid. The heat dissipation efficiency of PDMS is lower than that of glass but still sufficient for generating high efficiency separations. Channel designs on microfluidic devices are varied and it is common to include sharp bends and curves. When analytes negotiate these bends, they experience different velocities, or have to cover more distance depending on their loci at the curve. Constriction of the curved regions significantly reduces the dispersion due to the curved geometry.[2,14]

Causes of parabolic flow profile in microfluidic devices include joule heating and net pressure differences along channels. Unintentional pressure drops can occur when fluids in reservoirs are at different heights, thereby resulting in hydrodynamic flow. Another cause of pressure drops in the channels is non-uniform electroosmotic flow. The dispersion caused by parabolic flow

profile in rectangular channels is a function of channel depth *d*, channel width *w*, pressure drop ΔP, viscosity η, channel length *L* and diffusion coefficient *D*, as shown in the equation below.[2]

$$\sigma_{flow}^2 = 4\frac{(\Delta P)^2 d^6}{105 D\eta^2 L^2}\left[\frac{1}{12} - \frac{16d}{\pi^5 w} tanh\left(\frac{\pi w}{2d}\right)\right]^2 t \qquad \textbf{(1.20)}$$

When operating microfluidic devices, σ_{flow} can be minimized by ensuring that the fluid in reservoirs are maintained at about the same levels although calculations indicate that differences as large as 1 mm have negligible effect on the overall dispersion of the analyte peaks.[2]

Mass transfer processes involve the partitioning of analytes in and out of the stationary phase. Mass transfer processes in both the mobile phase and the stationary phase result in dispersion and are generally considered separately. The expression below (1.20) is used to determine the contribution to dispersion (σ_{st}) from the stationary phase.

$$\sigma_{st}^2 = \frac{k}{(1+k)^2} uL \frac{2d_{st}^2}{3D_{st}} \qquad \textbf{(1.21)}$$

where *k* is the capacity factor, u is the mobile phase velocity, *L* is the channel length d_{st} is the stationary phase thickness and D_{st} diffusion coefficient of the analyte in the stationary phase film. Dispersion due to mobile phase mass transfer, σ_{mp} is is shown in equation (1.21).

$$\sigma_{mp}^2 = \frac{1+6k+11k^2}{96(1+k)^2} uL \frac{d_{mp}^2}{D_{mp}} \qquad \textbf{(1.22)}$$

Where d_{mp} is the channel depth, and D_{mp} is the diffusion coefficient of the analyte in the mobile phase. The other terms remain the same as described in equation (1.20).

Electrophoretic separations do not require stationary phase so there is no contribution to dispersion from mass transfer processes.

Electrodispersion of analytes occurs when the analyte buffer and the running buffer have significantly different conductivities. The analytes will have different mobilites in the two

buffers and usually this manifests as non-symmetrical triangular peaks with poor separation of analytes.[2]

1.4.2 Resolution

Resolution (R_s) is another reliable measure of separation quality and it describes how well two adjacent peaks are separated. *Rs* is a dimensionless number calculated using the distance between any two adjacent peaks and their respective standard deviations as shown in the expression below;

$$\boldsymbol{R_s = \frac{2(x_1 - x_2)}{(w_1 + w_2)}} \qquad \textbf{(1.23)}$$

where x_1 and x_2 are the respective separation distances of two adjacent peaks and the w_1 and w_2 are the corresponding base line widths. The equation above can further be rearranged to calculate *Rs* for peaks that have been separated electrophoretically to yield;[2,15]

$$\boldsymbol{R_s = \sqrt{\frac{L}{H}} = \frac{\sqrt{N}}{4}\,\frac{\Delta u}{\bar{u}}} \qquad \textbf{(1.24)}$$

Where Δu represents the difference in ion mobilities of two adjacent peaks and $\bar{u}$ is the mean ion mobility of the two analyte peaks. A value of Rs> 1.5 indicates adequately resolved peaks when performing a qualitative analysis but higher values are desirable with quantitative experiments.

1.4.3 Peak Capacity

Another criterion for gauging the separation quality is the peak capacity n_c. This is a measure of the maximum number of resolved peaks within a separation length *L*. n_c is a preferred parameter of separation compared to resolution especially when the sample mixture is complex.[3] Peak capacity is calculated as follows;

$$\boldsymbol{n_c = \frac{L}{w} = \frac{L}{4\sigma}} \qquad \textbf{(1.25)}$$

1.5 Affinity Chromatography

Affinity chromatography is a unique separation technique that exploits the extremely specific biological interactions to achieve purification and separation. Some of these interactions include antigen-antibody and enzyme-substrate interactions. This technique enables the separation of analytes from complex matrices in a single process. For this technique to work, the substance to be separated must be capable of reversibly binding to a ligand attached to an insoluble matrix. In a column set-up, only the specific compound binds to the ligand and everything else is washed off. The desired compound is then recovered by disrupting the non-covalent interactions between the ligand and the compound.

1.5.1 Immunoaffinity Chromatography

This is a subset of affinity chromatography whereby the binding affinity of an antigen to a parent antibody is utilized as a basis for separation. The antibody is immobilized on a rigid support in a column and a complex mixture is passed through the column. The reversible interaction can be interrupted to release the antigen, resulting in a highly purified product. The interruption is achieved by altering the pH, or using chaotropes such as sodium cyanate, potassium cyanate or urea.[16] What makes immunoaffinity chromatography (IAC), and indeed other affinity chromatography techniques special is the efficient purification and separation of one component from a very complex mixture, in a single process. It is for this reason that affinity chromatography finds wide application in the separation of biomolecules from complex mixtures like blood, serum and insect hemolymph.

The stationary phase in immunoaffinity is prepared by covalently binding the affinant, in this case, the antibody, onto an insoluble support. The latter includes monoliths, polystyrene beads, glass beads, membranes, sol-gel or magnetic beads.[17]

1.5.2 Structure of the Antibody

The structure as shown in figure 2.2 has a basic unit containing four chains- two light chains (23KDa) and two heavy chains (50-70KDa). The chains are linked by covalent disulfide bonds and other non-covalent forces. Both the heavy and light chains have regions of sequence homology called domains. The light chains have 2 domains each; constant (C_L) and variable (V_L). The heavy chain has 5 domains, one variable, (V_H) and 3 or 4 constant domains (CH_1 –CH_3 or CH_4). The N-terminal domains form the binding site region of the immunoglobins, and they vary with different Igs. The variability of this region determines the selectivity of the antigen the Ig binds. Antibodies may be monoclonal or polyclonal, depending on how they are produced.

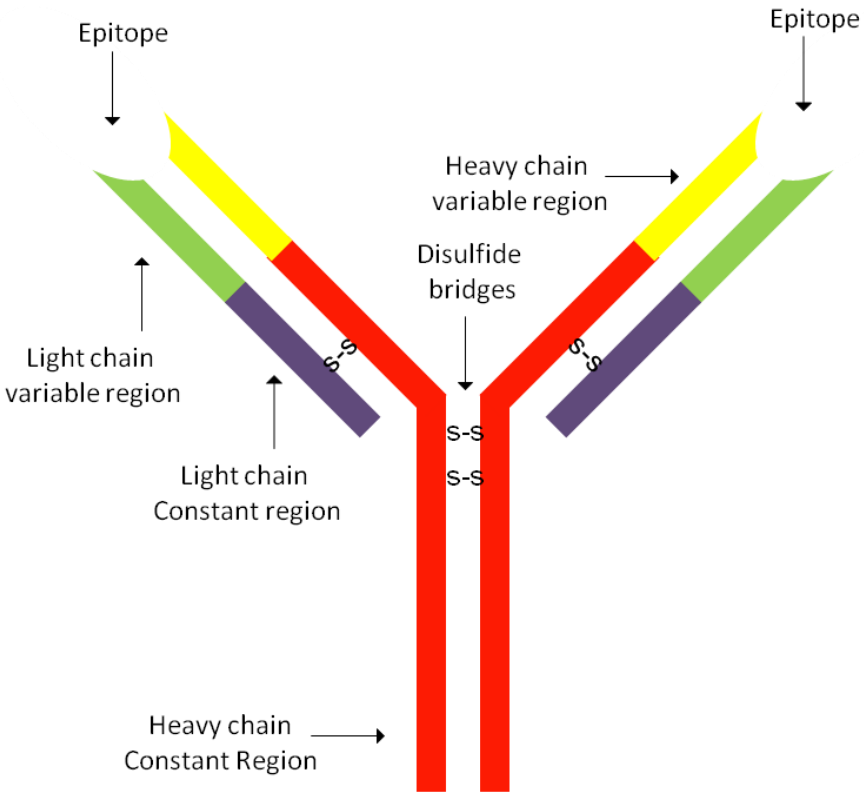

Figure 1.4. Basic structure of immunoglobins.

Polyclonal antibodies are prepared from immunized animals and consist of a complex mixture of antibodies produced from different B cell clones. These antibodies recognize different epitopes of the antigen. On the other hand, monoclonal antibodies are a homogenous preparation of antibodies produced *in vitro* from one type of B cell clones, and they consist of a single type of binding site called a paratope.

1.5.3 Antibody-antigen Interactions

Antibody-antigen interactions involve the hyper variable region of the antigen-binding site (paratope) and the antigenic determinant (epitope). The forces responsible for the binding process include hydrogen bonding, hydrophobic interactions, ionic interaction, Van-der Waals forces, and stearic repulsive forces. The interaction is expressed mathematically as follows;

$$\boldsymbol{Ab + Ag \leftrightharpoons AbAg} \qquad \textbf{(1.26)}$$

Where *Ab* is the free antibody, *Ag* is the free antigen and *AbAg* is the antigen-antibody complex. The law of mass action states that the rate of formation of the complex is proportional to the concentration of the reactants. The expression above can, therefore, be written as follows;

$$\boldsymbol{K_a[Ab][Ag] = K_d[AbAg]} \qquad \textbf{(1.27)}$$

Where K_a, *Kd*, [*Ab*], [*Ag*] and [*AbAg*] are the association constant, the dissociation constant, the free antibody concentration, the free antigen concentration and the antibody -antigen complex concentration respectively. The rate of formation of *AbAg* is given by;

$$\boldsymbol{\frac{d[AbAg]}{dt} = K_a[Ab][Ag] - K_d[AbAg]} \qquad \textbf{(1.28)}$$

At equilibrium, the rate becomes zero and the expression becomes

$$K_a[Ab][Ag] = K_d[AbAg] \qquad \textbf{(1.29)}$$

Rearrangement yields

$$\frac{K_a}{K_d} = K = \frac{[AbAg]}{[Ab][Ag]} \qquad (1.30)$$

where K is the equilibrium constant. For the antibody-antigen association to be stable, the K_a should be within the range 10^4-$10^8 M^{-1}$.[16]

1.6 Proteomics and Mass Spectrometry

Proteomics is a fairly recent field that involves the study of protein structure and functions and how these proteins are affected by biological processes.[18] Although the term 'proteomics' was coined in the late nineties, detailed studies of proteins had begun in the seventies with the advancement of electrophoresis-based separations that included 2D gel electrophoresis. Proteomics is now fundamental in identifying biomarkers, drug targets and studying biological mechanisms in cells, tissue and serum. Initially, the idea of studying whole cell proteome sounded over-ambitious, considering that the proteome samples are complex, have dynamic characteristics and have highly varied abundances. However, with advancing analytical technology, great progress has been achieved and in the past decade, there has been an exponential increase in publications on proteomics. In particular, mass spectrometry (MS) has become an indispensable technique for protein profiling. MS accurately separates mobile ion species based on their mass/charge (m/z) ratios. Therefore, samples must be ionized for MS to work. A common technique of ionizing samples is Electrospray ionization (ESI). In this ionization technique, the sample is passed through a stainless steel capillary needle held at high voltage, resulting in a fine spray of charged droplets. The solvent in the spray is rapidly evaporated in vacuum and as a result, the charge density increases and desorption of ions into the ambient gas occurs.[19] The ionized species are then swept into an electromagnetic field where their masses are detected based on their speed and trajectory. Available mass analyzers include quadrupole, time-of-flight (TOF) and Orbitrap.[20] ESI is a soft ionization technique and the

analyte is not fragmented during ionization. This is the reason why it is commonly preferred over other sample ionization methods.

There are two distinct approaches used in the identification of proteins and other large molecules; top down and bottom up approaches. In the top down approach, separation techniques such as 2D gel electrophoresis or liquid chromatography are utilized to isolate intact proteins from a sample. The purified protein is then identified by MS. This approach is preferred when analyzing the properties of the intact protein. Sample preparation for MS is less rigorous compared to bottom up approach. Bottom up approaches begin with digestion of a complex protein sample prior to MS analysis. The sample may be native or previously purified. Enzymatic digestion fragments the protein into short peptide chains at specific points on the primary structure. These fragments are then further separated, usually by reverse phase liquid chromatography, prior to ionization and MS analysis. This approach is also commonly referred to as 'shot gun' approach. To identify the protein, the mass data from the fragments are compared to those of known identities in protein databanks by using specialized search engines like Matrix Science (MASCOT). ESI-MS utilizing time-of-flight (TOF) or Orbitrap mass analyzers are capable of analyzing peptide chains with small mass differences.

1.7 Microfluidics

Microfluidics is a dynamic field of science that has gained great popularity since its development two decades ago. Microfluidics encompasses the design, fabrication of devices consisting of channels and features with at least one of the dimensions measuring < 1 mm. Microfluidic devices, also known as micro total analysis systems or lab-on-chip devices, have

been utilized in diverse research areas such as cell analysis,[21] molecular biology,[22] microelectromechanical systems (MEMS)[23] and fluid transport and manipulation.[24] The motivation to use microfluidic devices accrues from the benefits that accompany miniaturization such as faster analysis times, low reagent consumption, improved robustness, less generation of waste, ease of performing parallel experiments and amenability to automation.[25] Initially, glass etching was the primary method of fabricating microfluidic devices but soft lithography[26] is now more popular mainly because it is a faster and cheaper alternative. Soft lithography begins with making a mold on a substrate like silicon wafer, using photoresist. An elastomer such as poly (dimethylsiloxane) (PDMS) is then poured over the mold and baked at ~80^{o}C. The now hardened but pliable PDMS is then peeled off the mold and assembled to complete the microfluidic device fabrication. Several operations can be performed on microfluidic devices and these include mixing, valving and fluid compartmentalization but the most common operation is separation. Analyte separations on microfluidic devices is often electrophoresis- based, sometimes in combination with other techniques such as immunoaffinity chromatography. The channel designs on the devices are fashioned to suit specific operations. Most analyte separations utilize intersecting channels whereby sample analytes are introduced into the separation channel by either of two techniques; gating or pinching (Figure 1.5). The two sampling techniques are achieved by manipulation of electric fields in the channels. The voltages applied to the channels to elicit the desired electric fields are determined by Kirchhoff's law (1.25) and Ohm's law (1.26);

$$\sum_{k=1}^{n} \boldsymbol{I_k = 0} \qquad (\mathbf{1.25})$$

$$\boldsymbol{V = IR} \qquad (\mathbf{1.26})$$

Kirchhoff's law state that at an intersection, the sum of current of all incoming channels is equal and opposite to the sum current of the outgoing channels. By considering the fluid resistance and the field strength, it is then possible to calculate the voltage at the intersection.

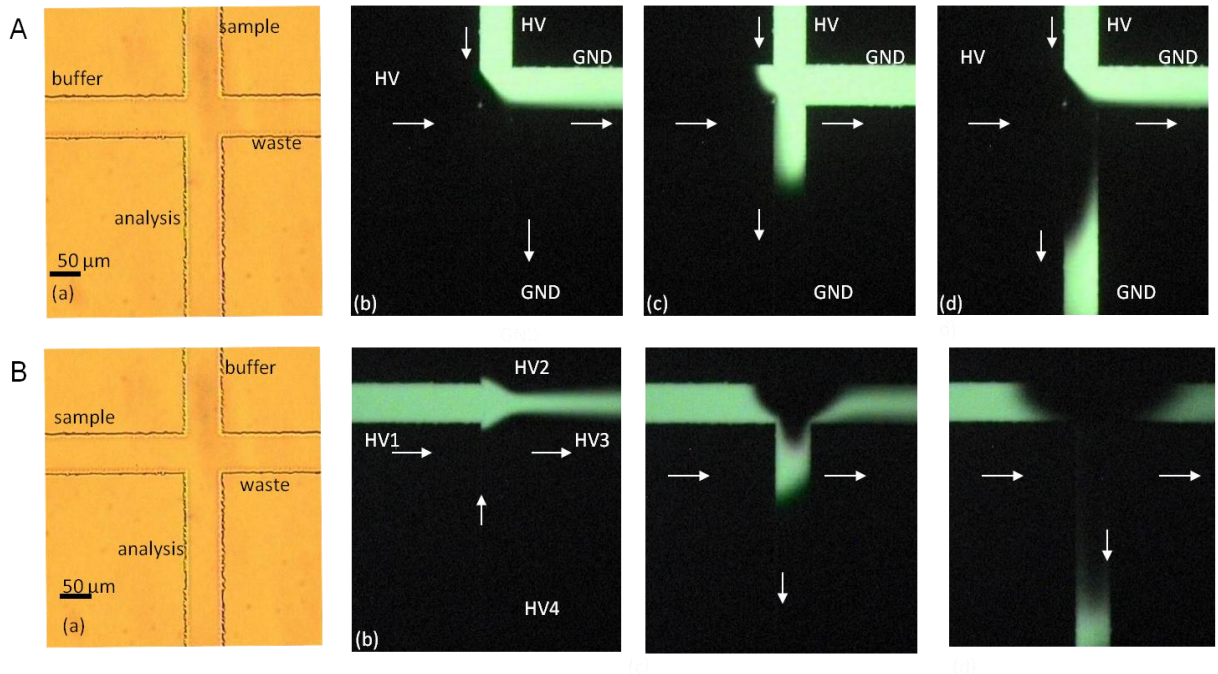

Figure 1.5. Sequential frame grabs from videos demonstrating the types of sample injection used on microfluidic devices; Gated injection (A) and pinched injection (B).

Other techniques of sample introduction are being explored. In our group, we have used PDMS's property as an electroactive polymer to perform non-biased sample injections into a separation channel on a microfluidic device.[27] The combination of hydrodynamic flow and electrophoresis is another unique method of sample introduction into a separation channel. In chapter 3, I will discuss experiments performed on a microfluidic device that involved hydrodynamic transportation of intact cells onto an intersection where they encountered a field strength that was sufficient to lyse and subsequently separate the lysate in a separation channel.

1.8 Conclusion

The fundamental basics of electrophoresis and immunoaffinity chromatography have been discussed. Miniaturization of these techniques on microfluidic devices offers a reliable platform to perform efficient analysis of small sample volumes such as single cells (volume ~ 10 pL) and hemolymph from mosquitoes (~70 nL). Other advantages of miniaturized separation techniques include low reagent consumption, less waste generation, and faster analysis times. In the subsequent chapters, research utilizing the two techniques will be presented. Chapter 2 will discuss immunoaffinity chromatography employed to isolate proteins involved in the immune system of *M. sexta* and *A. gambiae*. Proteins were identified from as little as 13 nL of hemolymph samples. In chapter 3, a novel microfluidic device that was used to study expression of nitric oxide in single mammalian cells will be discussed. Individual Jurkat cells were transported, lysed and lysate from the cells singly analyzed by electrophoresis. We designed a mixing device based on the property of PDMS as an electroactive polymer and the preliminary findings will be discussed in chapter 4.

Chapter 2 - Micro Column Separation of Proteins from Insect Hemolymph

World Health Organization statistics (2012) indicate that malaria affects more than 200 million people globally, resulting in 600,000 deaths annually. Many of the fatalities occur in sub-Saharan Africa where a child dies of malaria every minute. To date, a malaria vaccine has been elusive and effective treatment and management of malaria has been hampered by the ability of the parasite to develop resistance to medicine. For this reason significant attention is directed toward vector control as a preventative measure. A better understanding of the *Plasmodium*–*Anopheles* interaction is necessary to develop more effective interventions to curb malaria.[28,29] Current research is focused on the development of new insecticides with different modes of activity that are less prone to resistance by the vector. An example is a recent proposal to develop insecticides that target mosquitoes late in their reproductive cycle.[30] These so-called late-life acting (LLA) insecticides would minimize selective pressure for insecticide resistance. However, identification of potential LLA insecticide targets requires lengthy bioassays and this limits the number of potential targets that can be studied.

The mosquito, like all invertebrates, possesses an innate immune response system that comprises of cellular and humoral components. An important humoral immune strategy is the activation of proteolytic cascades that convert pro-phenoloxidase (PPO) into the active form, phenoloxidase (PO), which in turn catalyzes reactions that produce eumelanin. Eumelanin is a dark heteropolymer that is deposited on the surface of the invading microbes resulting in encapsulization and eventual death of the microbes.[31] The PPO pathway is tightly regulated by serine protease inhibitors (serpins). These serpins act by forming covalent complexes with the

proteases, thereby distorting the protease structures and rendering them inactive. Of particular interest is serpin 2 (SRPN2) from *Anopheles gambiae* mosquito that has shown potential as a LLA insecticide target. [32,33] The only known function of SRPN2 is inhibition of melanization and its depletion shortens the life span of *Anopheles gambiae*.[32-34] One protease that SRPN2 is known to inhibit is the clip serine protease CLIPB9, which activates proPO to PO.[32] The other serine protease targets that mosquito SRPN2 interacts with are not well known. Studies on mosquito hemolymph are restricted because of the low nanoliter volumes found in the insect. Standard analytical techniques are not sensitive enough to study these small volumes.[35] Furthermore, the low concentrations of serpins and proteases in the hemolymph would necessitate the use of hundreds of mosquitoes to attain detectable amounts of the desired protein.

The aim of the experiments discussed in this chapter was to develop a microscale immunoaffinity chromatography technique to isolate SRPN2-protease complexes from female *Anopheles gambiae* mosquitoes followed by identification of the proteases by mass spectrometry. Immunoaffinity is a powerful separation technique that takes advantage of the highly specific biological interactions between antibodies and their complementary antigens to efficiently separate isolate and concentrate individual proteins from complex matrices like hemolymph or serum. Since the activity of the serpins involves the formation covalently bound irreversible complexes, it was possible to isolate the complexed serpins because the serpin antibody bound the same paratope on both the un-complexed SRPN2 and SRPN2-protease complexes. Following immunoaffinity chromatography, the isolated proteins were analyzed with Western blotting and silver staining and ESI-MS. The significant peptide fragment ions from ESI-MS analysis were checked against protein databases using MASCOT software (Matrix

Science) to identify the proteases. To optimize the immunoaffinity experiments, hemolymph from the model insect, *Manduca sexta*, was used.

2.1.1 Innate Immune Response in Insects

Vertebrates possess both innate and adaptive immunity that they deploy in the event of a microbial invasion. On the other hand, invertebrates, have only the innate immune response that begins with recognition of non-self, which in turn triggers responses that may be cellular or humoral.[36] The cellular immune strategies include cell phagocytosis, melanotic encapsulization and physical barriers like the midgut wall. Humoral responses involve activation of enzymes that initiate proteolytic cascades including the proPO pathway whose end result is the conversion of proPO to PO which in turn catalyzes the production of eumelanin used to encapsulate the pathogens (PPO pathway). Other humoral responses include the production of reactive nitrogen and oxygen species that are toxic to the invading microbes, and production of antimicrobial peptides that act against bacteria, fungi and viruses.[36] Figure 2.1 is a simple illustration of the major components of the insect innate immune system.

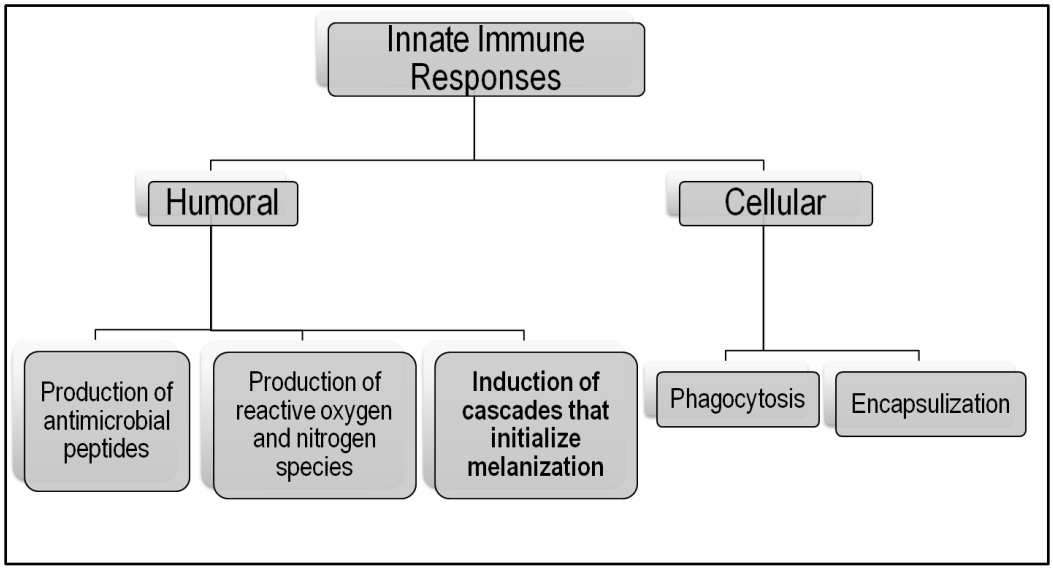

Figure 2.1. Components of the innate immune response system in invertebrates.

Proteolytic cascades, including the PPO pathway, are triggered when biomolecules originating from invading microbes get bound to pattern recognition receptors (PRR) . These biomolecules include β-1,3-glucans, lipopolysaccharides and peptidoglycans.[37,38] The cascade culminates in the activation of clip serine proteases that convert PPO to PO. *Anopheles gambiae* CLIPB9 is an example of these proteases.[32] The PPO pathway is tightly regulated by serpins to prevent self-destruction from the toxic reactive species expressed during eumelanin production.

Figure 2.2 is a diagrammatic representation of the PPO cascade.

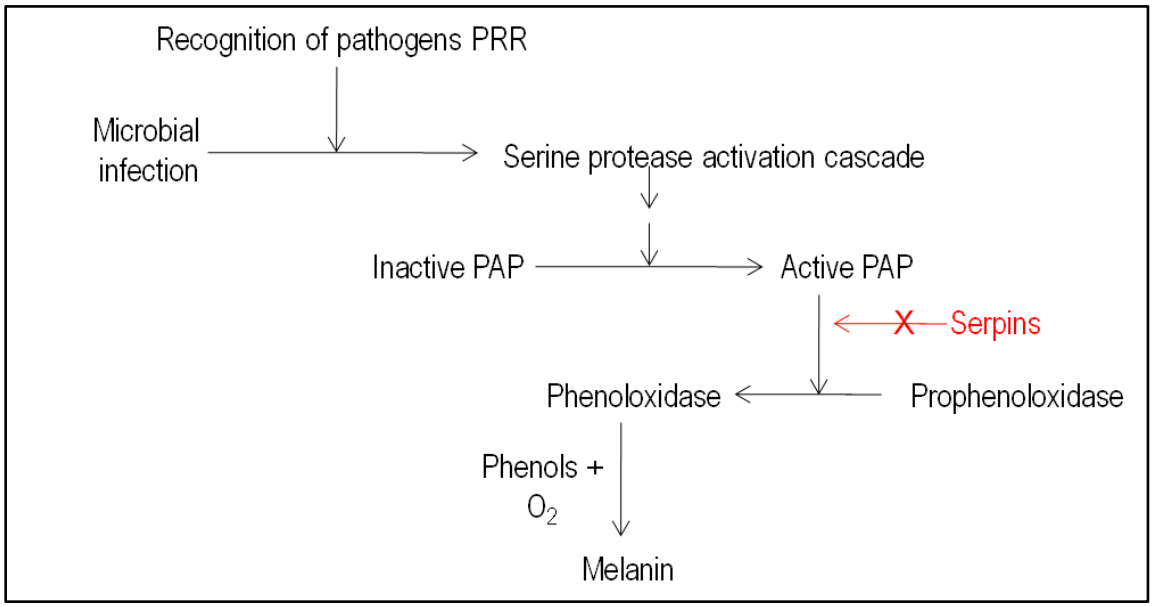

Figure 2.2. Illustration of prophenol oxidase cascade.
Pathogen recognition activates a cascade which ultimately activates the conversion of prophenol oxidase to phenol oxidase (PO). PO catalyzes reactions that produce precursors for melanin production. Abbreviations: PRR, pattern recognition receptors; PAP, proPO activating proteinase.[31]

Serpins are 45-50 kDa proteins, with amino acid residues ranging from 350 to 470 residues and contain a reaction center loop (RCL) near the carboxyl terminal.[39] The 3D structure is composed of 7-9 α-helixes and 3 β-sheets. Figure 2.3 shows the structure of native SRPN2 from

A. gambiae.[34,40] The selectivity of the serpin is dependent on the amino acid sequence in the RCL. Most serpins act as irreversible inhibitors of serine proteases by formation of stable covalent complexes with the proteases, following the cleavage of a scissile bond in the RCL.[41,42]

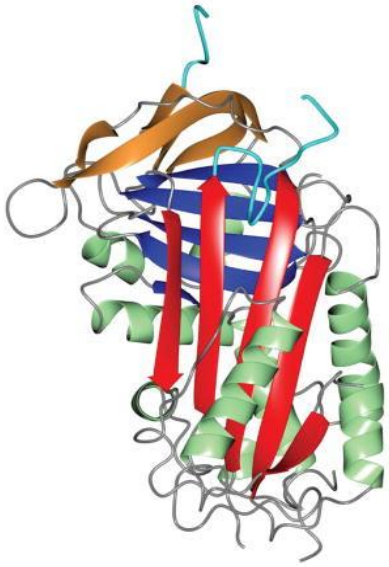

Figure 2.3. Structure of SRPN2 from *A. gambiae* (PDB ID: 3PZF).[40]
The α-helices are shown in green the reaction center loop (RCL) is shown by the cyan strand and the β-sheets A-, B- and C- are represented by red, blue and tan, respectively.

2.1.2 Mechanism of Serpin Inhibition

The inhibition mechanism of serpins involves the formation of stable covalent complexes with serine proteases. Initially, the proteinase forms a non-covalent Michaelis-like complex, via interactions with the RCL residues P1 and P1' in the region near the scissile bond. Following a nucleophilic attack by serine on the active site, a covalent ester linkage between Ser-195 of the proteinase and the P1 residue of the serpin is formed, followed by cleavage of the peptide bond. It is at this point that the RCL starts to insert into the β-sheet A and drags the covalently bound proteinase with it, resulting in a massive conformational change.[43] As a

consequence, the proteinase is distorted and therefore inactivated. Figure 2.4 is an example of a serpin-protease covalent complex formed when rat trypsin is inhibited by serpin1K.[44]

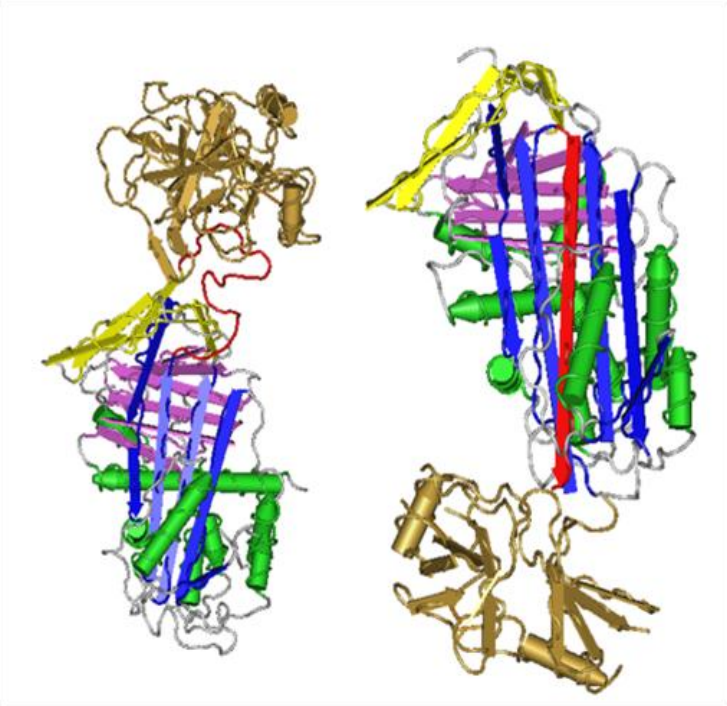

Figure 2.4. Left: Structure of non-covalent complex of insect Serpin 1K and mutated inactive trypsin (PDB ID: 1K90).

The RCL is shown in red. Right: Irreversible (covalent) complex with the RCL inserted into β-sheet A, shown in red, and the proteinase is translocated, resulting in distortion (PDB ID: 1EZX, NCBI database).[44]

2.2 Experimental Procedures

2.2.1 Hemolymph Collection, Preparation and Storage

M. sexta hemolymph. Hemolymph was collected from day 3 3rd instar *M. sexta* larvae injected with 100 µg of *M. luteus* bacteria 24 hrs prior to hemolymph collection. The larvae were chilled on ice for 20 min after which one of the prolegs was clipped to start the bleeding. The hemolymph was collected into centrifuge tubes containing appropriate stock volumes of

diethyldithiocarbamic acid (DETC) and polythiourea (PTU) to obtain final concentrations of 10mM and 0.1mM respectively. DETC and PTU prevent melanization of hemolymph. The expressed hemolymph was then centrifuged at 8000 rcf for 15 min at 4^0C to remove hemocytes. 100 or 50 µL aliquots were prepared and stored at -80^0C until needed.

A. gambiae hemolymph. Day 2 mosquitoes were injected with M. luteus bacteria solution whose optical density was 0.58 prior to hemolymph collection 24 h later. To collect hemolymph, the mosquitoes were knocked down with carbon dioxide and arranged on an ice plate on their backs in groups of 10 or 15. The proboscides were then clipped and the thorax squeezed. The clean drop of hemolymph that formed at the tip of the clipped proboscis was collected in a drop of PBS buffer containing 100× diluted protease inhibitor cocktail (Roche) and 1% PTU using a 10 µL pipette. The aliquots were stored at -80^0C until when needed.

2.2.2 Purification of Serpin Antibody from Rabbit Antisera

Antisera against *M. sexta* SERPIN-1 (KSU-178)[45] and *A. gambiae* SRPN2 (DIF-5, DIM-6 [32] and KSU-239) were generously provided by Dr. M. Kanost (Biochemistry Dept., Kansas State University) and Dr. K. Michel (Division of Biology, Kansas State University), respectively. Aminolink® Plus Immobilization Kit (Pierce, Rockford IL) was used to purify the serpin antibody from the antisera. The kit consisted of argarose bead slurry containing activated aldehyde groups on the bead surface. The aldehyde groups form spontaneous Schiff bases with amine groups on the ligand to be immobilized, and are stabilized by sodium cyanoborohydride, which is a mild reducing agent. The purification procedure consisted of three main steps namely, 1) ligand immobilization, 2) antibody purification 3) elution of purified protein.

2.2.2.1 Ligand Immobilization

E.coli expressed recombinant *A. gambiae* SRPN2 or *M. sexta* SERPIN-1, provided by Drs. Michel (Division of Biology, Kansas State University) and Kanost (Biochemistry Department, Kansas State University), respectively, were used as the ligand in our experiments. The proteins, originally in tris buffer (20mM Tris, 50 mM NaCl), were dialyzed into coupling buffer (Phosphate buffered saline, pH 7.2). The affinity column was equilibrated to room temperature and then rinsed with 5 mL of the coupling buffer. Following complete drainage, the bottom cap of the column was replaced and 1 ml of either *M. sexta* recombinant SERPIN-1 or *A. gambiae* recombinant SRPN2 protein solution applied to the top of the column. The top cap was replaced and the reaction slurry incubated with end-to-end rocking for 4 hrs. The flow through saved to analyze the coupling efficiency. The column was then transferred to a fume hood where 2 mL of coupling buffer and 40 µL of sodium cyanoborohydride were added. The bottom and top caps of the column were replaced and the columned rocked for at least 4 hrs. The column was drained and then rinsed and incubated with quenching buffer (1M Tris-HCl, 0.05% NaN_3, pH 7.4) for 30 min. Any uncoupled protein was removed by flowing at least 15 mL of wash buffer (IM NaCl, 0.05% NaN_3) followed by storage in coupling buffer containing 0.05% NaN_3.

2.2.2.2 Antibody Purification

A porous disc was placed at the top of the column to within 1 mm of the gel. The column was then rinsed with at least 5 mL of coupling buffer prior to applying 2 mL of antisera solution. The column was then allowed to drain until the sample front was very close to the bottom or exactly 2 mL of flow through had been drained. The bottom and top caps were sequentially replaced and the column rocked for I hr at room temperature. During this period, the immobilized serpin on the beads bound the corresponding antibody from the antisera. All other proteins not captured by the serpins were washed off the column using 12 mL of PBS, pH 7.4.

The flow through was saved to analyze purification efficiency. In the situation where more than 2 mL of antisera was purified, this procedure was repeated until all the antisera had been incubated with the column.

2.2.2.3 Elution of Bound Antibody

Glycine buffer (100mM glycine-HCl, pH 2.5) was used to elute the bound antibody off the affinity column. 8 mL of glycine was applied at the top of the column and 1 mL fractions were collected into 1.5 mL centrifuge tubes each containing 100 µL 1M Tris, pH 7.5). BioTek's PowerWave HT microplate spectrophotometer (Winooski, VT) was utilized to quantitatively determine the total protein concentration in the elution fractions at 595 nm, by comparing intensities with those of known concentrations of bovine serum albumin (Pierce, Rockford, IL). Fractions with the highest concentrations were pooled and exchanged into 10mM phosphate buffer, pH 7.4. The antibody solutions were gently mixed with glycerol in a 1:1 ratio (v/v) and stored at -21^{o}C.

2.2.3 Experimental Design for Immunoaffinity Experiments

Immunoaffinity experiments with the hemolymph samples were performed in two formats; online and/or batch formats. Both formats utilized protein A coated magnetic beads, 2.8µm in diameter, purchased from Invitrogen (Carlsbad, CA). The beads consisted of polymer-coated iron oxide spheres, with protein A covalently linked to the surface. In the online format, the magnetic beads were packed into a capillary column and held in place by strong magnets. Buffers and sample solutions were then flowed over the beads in a continuous fashion. This format was used with hemolymph samples from *M. sexta* and the design and operation are discussed in the appendix section of this dissertation. On the other hand, the batch experiments

consisted of placing beads in a centrifuge tube where the buffers and sample solutions were applied in discrete volumes.

In the batch format, 40 µL of bead slurry was aliquoted into a 0.5 mL centrifuge tube (Eppendorf AG, Hamburg, Germany). A neodymium iron boride rare earth metal magnet (K&J Magnetics, Jamison, PA), 1.85 cm by 1.25 cm by 2.5 mm, was placed on the side of the centrifuge tube to decant the beads. The bead free decant was removed using a transfer pipette and discarded. Next, the magnet was removed and the beads re-suspended in 200 µL of binding buffer by gently mixing with a transfer pipette before placing the tube on a magnet and removing the supernatant. This wash step was repeated 2 more times. Appropriate purified antibody solution was made to 100 µL with binding buffer and added to the beads. 5 µL of this solution was saved for binding efficiency analysis. The mixture was gently mixed using a vortexer (Fisher Scientific, Pittsburg, PA) for 20-30 min after which the supernatant was removed and saved. The beads were then rinsed with binding buffer thrice then with pre-crosslinking buffer (20mM triethanolamine, pH 8.2). Next, the beads were incubated with 500 µL of 20mM DMP in pre-crosslinking buffer for 30 min at room temperature with gentle mixing. The crosslinking buffer was removed and replaced with 500 µL of quenching buffer and shaken for 15 min. The beads were finally rinsed with binding buffer and transferred to a new centrifuge tube. To remove un-crosslinked antibody, the binding buffer was removed and replaced with elution buffer (100mM glycine, pH 2.5). The beads were re-suspended in the elution buffer and mixed gently for 2 min. The elution buffer was removed and the beads were rinsed with binding buffer thrice. The magnetic beads were now ready to isolate proteins from hemolymph samples or recombinant protein solution. The samples to be analyzed had their volumes made up to at least 100 µL with binding buffer. The diluted hemolymph or recombinant protein solution was then

added to the antibody-coated beads and incubated at room temperature for at least 1 hr with gentle shaking. A few microliters of the sample solution were saved for later analysis of isolation efficiency. Following incubation, the unbound samplesolution was removed and saved. The beads were then washed at least three times with 100 µL each of binding buffer. All saved samples were stored at 4^{o}C prior to performing SDS-PAGE.

2.2.4 Sodium Dodecyl Sulfate-Polyacrylamide Gel Electrophoresis (SDS-PAGE)

NuPAGE, 4-12% Bis-Tris gels (Invitrogen, Carlsbard, CA) were used in all SDS-PAGE experiments. Samples were prepared for SDS-PAGE by adding 2× SDS buffer (20% glycerol (v/v), 4% SDS (w/v), 0.2 mg/ml bromothymol blue, 10% β-mercaptoethanol (v/v)), in equal volume to each sample. The samples were then briefly mixed and incubated at 95^{o}C for 5 min, followed by centrifugation for 1 min at 14000 rpm. 3-(N-morpholino)propanesulfonic acid (MOPS) buffer (Invitrogen, Carlsbard, CA) was diluted 20-fold and placed in an XCell SureLock^{TM} electrophoresis cell (Invitrogen; Novex Mini-Cell). The reduced samples were then loaded onto the gel lanes and 200V was applied to the gel for 45 min. The separated proteins were then detected by Western immunoblotting or silver staining.

2.2.5 Western Immunoblotting

Following SDS-PAGE, the proteins on the gel were transferred onto a 0.45 µm nitrocellulose membrane (GE Osmonics Labstore, Minnetonka, MN). A Trans-Blot SD Semi-Dry transfer cell (Bio-Rad, Hercules, CA) was employed for this purpose. The gel was removed from the cassette and placed in a tray containing the western transfer buffer (48mM TrispH 9.2, 39mM glycine, 1.3 mM SDS, 20% methanol (v/v)). The membrane and two pieces of thick blot paper were also soaked in this buffer. Next, the gel was placed on the wet nitrocellulose membrane and then sandwiched between the blot papers and placed on the semi-dry transfer cell.

The proteins on the gel were transferred by applying 10V for 1 hr. The protein-laden membrane was then incubated, with shaking, in 10 mL of 15% milk solution prepared in Tween-20-Tris buffered saline, T-TBS (25mM Tris pH 7.4, 137mM NaCl, 2.7mM KCl, 0.05% Tween-20), for 1 hr. This step served to block any remaining empty sites on the nitrocellulose membrane. The blocking milk solution was discarded and replaced with 10 mL of fresh milk solution. 10 uL of purified *M. sexta* SERPIN-1 or *A. gambiae* SRPN2 antibody (antibody to serpins on the membrane) solution was added to the milk and the membrane incubated for another 1 hr after which the membrane was washed thrice with T-TBS. Next, the membrane was incubated with 10 mL of milk containing 3 µL of secondary antibody (goat anti-rabbit IgG (H+L) HRP phosphatase conjugate, Bio-Rad) for 1 hr followed by three 2 min washes with Tris buffered saline (25mM Tris pH 7.4, 137mM NaCl, 2.7mM KCl). Finally, the membrane was developed using an alkaline phosphatase Conjugate Substrate Kit (Bio-Rad) for at least 15 min. The membrane was finally rinsed with distilled water and air dried.

2.2.6 Silver Staining

A SilverXpress® Silver Staining Kit (Invitrogen, Carlsbard CA) was also used to visualize proteins on SDS-PAGE gels. The gel was removed from its cassette and placed in a tray containing the fixing solution which consisted of 45% ultra pure water, 45% methanol and 10% acetic acid, and gently shaken for 10 min. This solution was decanted and replaced with a sensitizing solution comprising of 105 mL ultra pure water, 100 mL methanol and 5 mL sensitizer (contains glutaraldehyde), for a total of 20 min. Next the gel was rinsed with ultra pure water and incubated with a staining solution for 15 min. The staining solution consisted of 5% Stainer A (contains silver nitrate), 5% Stainer B (contains ammonium hydroxide and sodium hydroxide) and 90% ultra pure water. After two rinses with ultra pure water, the gel was next

incubated with Developing Solution (95 mL ultrapure water and 5 mL Developer (contains formaldehyde and citric acid)) for 3-15 min. A Stopping solution (contains citric acid) was added to directly to the gel when the appropriate band intensity was reached. Finally, the gel was rinsed thrice with ultra pure water. The now stained gel was placed in a gel drying solution [20% (v/v) ethanol, 5% (v/v) glycerol] for 5 min then dried between 2 cellophane membranes (Fisher).

2.3 Results

The goal of this study was to isolate SRPN2-protease complexes from mosquito hemolymph using immunoaffinity chromatography. Immunoaffinity chromatography is a powerful separation technique that is capable of isolating specific species from very complex matrices such as hemolymph due to the highly unique interactions between the antibody and the antigen. The SRPN2-protease complex and the uncomplexed SRPN2 are separated simultaneously, since the antibody on the beads binds to the same paratope in the complex as well as the un-complexed serpin. The isolated proteins were subjected to SDS-PAGE, Western blotting, silver staining and ESI-MS to identify the proteases.

For the preliminary experiments, recombinant SERPIN-1 and hemolymph from *M. sexta* larva were used to optimize the immunoaffinity chromatography experiment. *M. sexta* is well studied and is often used as a model insect. Furthermore, the larva is large and provides relatively large volumes of hemolymph compared to the mosquito. Interestingly, serpins from *A.gambiae* have been shown to inhibit PPO in *M. sexta*.[34]

At the scale the immunoaffinity experiments were performed, it was important to have the immunoaffinity chromatography experimental procedure to operate at its maximum binding efficiency. One strategy to achieve this was by utilizing purified antibody rather than antisera.

This way, we ensured that all the binding sites on the magnetic beads were occupied by the antibody of interest and all other non-serpin binding antibodies were excluded. The use of polyclonal antibodies rather than monoclonal ones was advantageous as they recognized more binding sites on the antigen. Another strategy we employed was to crosslink the antibody to the beads. This step reduced the large background from antibody that would otherwise co-elute with the target protein.

The flow in the capillary is parabolic and as such, it was difficult to collect the elution fraction in one fraction. As a consequence, the eluted sample fractions were diluted. An alternative would be to perform the immunoaffinity isolation in a batch format. This allows all of the eluted protein to be discretely collected in one small fraction. For the batch experiments reported below, 120 µL of protein A magnetic beads were aliquoted into a centrifuge tube. The buffer was replaced by 180 µL of SERPIN-1 antibody (35 ng/ µL) and incubated with gentle shaking for at least 20 min. The bound antibody was crosslinked as detailed in the experimental procedure in section 2.2.3.2. The now antibody-coated beads were divided into 3 equal portions and the buffer they were in was removed and replaced with PBS-diluted solutions containing 1.0, 0.4 and 0.096 µL of *M. sexta* hemolymph respectively, followed by incubation at room temperature for 1 hr with gentle shaking. Bound proteins were eluted into 20 µL of 50 mM glycine-HCl, pH 2.5. The eluents were neutralized with 1M sodium phosphate and divided into two. One half was saved for ESI-MS analysis while the other half was used for SDS-PAGE and silver staining.

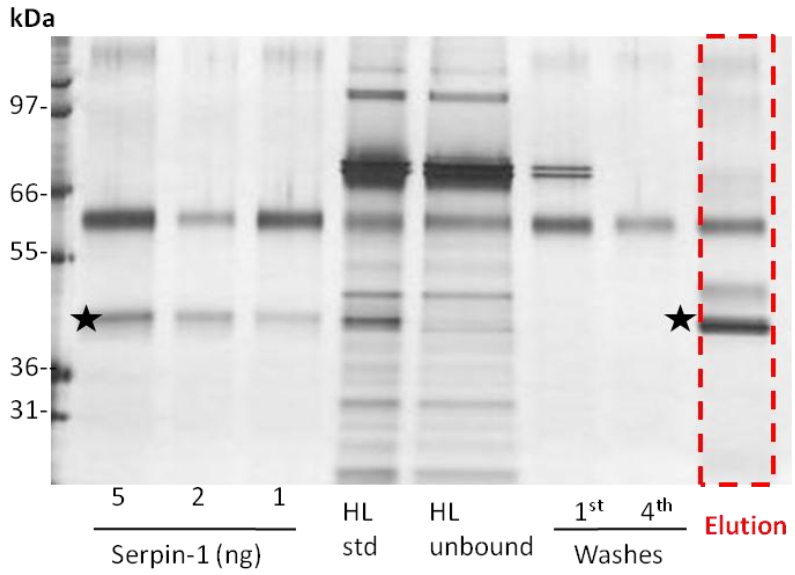

Figure 2.5. Serpin-1 Antibody-coated beads can isolate native serpin-1 from 96 nL of *M. sexta* hemolymph. 60 µL of PBS containing 96 nL of M.sexta hemolymph was incubated with Serpin-1 antibody-coated beads for 1 h at room temperature with gentle shaking. The supernatant was removed and the beads washed thrice with PBS. The bound proteins were eluted into 20 µL of elution buffer (50mM glycine-HCl, pH 2.5). Native Serpin-1, shown by asterisk in the silver stain gel above, was depleted from the hemolymph as seen from the fainter Serpin-1 band in the unbound hemolymph compared to the hemolymph standard.

ESI-MS analysis was performed at the Biotechnology core facility (KSU) by Dr. H. Yasuaki. The samples were digested with trypsin prior to analysis. The effective sample volume analyzed by MS was ~25% of the original sample. In all the samples, SERPIN 1 was detected. Unfortunately, no SERPIN-1-protease complexes, whose band was expected at ~ 62 kDa, were detected. Despite this, it was impressive to observe that the column was able to capture SERPIN-1 as little as 96 nL of hemolymph. This volume is within the range of single mosquitoes. Table 2.1 is a summary of the ESI-MS results of the samples analyzed at KSU biothechnology core facility.

Table 2.1. ESI-MS analysis of elution fractions from IAC experiments with 1.0, 0.4 and 0.096 µL of *M. sexta* hemolymph. Summary of MASCOT search results from NCBI database.

Equivalent emolymph sample (Elution volume used for ESI-MS)	Score*	Mass	Num. of matches	Num. of sequences	emPAI**	% Sequence coverage	Description
1.0 µL (136 nL)	450	44352	23	17	2.15	41	Serpin-1 *M.sexta*
0.4 µL (55 nL)	368	43532	16	13	1.41	35	Serpin-1 *M.sexta*
0.096 µL (13 nL)	90	43483	2	2	0.16	13	Serpin-1 *M.sexta*

*** score>54 indicates protein identity/extensive homology**

**** exponentially modified protein abundance index**

To increase the concentration of SERPIN-1-protease complex, *M. sexta* hemolymph was treated with a 1 mg/ mL zymosan A solution (Sigma). Zymosan A is a glucan found on the surface of yeast cells that causes an immune reaction. Its addition to hemolymph served to increase the formation of SERPIN-1-protease complex. 1 uL of the solution was added to 9 µL of freshly thawed hemolymph followed by incubation at room temperature for at least 10 min. There was a marked increase in the intensity of the serpin protease complex band at ~ 64KDa as shown in Figure 2.6.

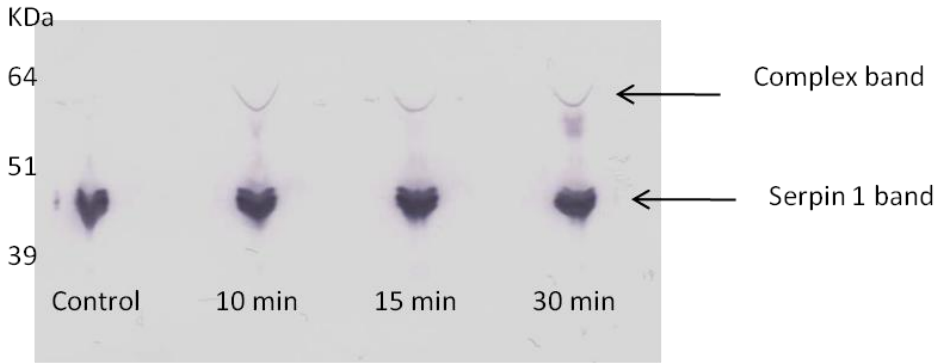

Figure 2.6. Effect of zymosan A on the concentration of serpin-protease complex in *M. sexta* hemolymph following different incubation times.

The Western blot was performed with rabbit SERPIN-1 antisera, KSU 178.[45] Within 10 min, the concentration of the complex was visibly increased (u-shaped band at ~ 64 kDa) compared to the untreated hemolymph (extreme left lane). The concentration of the complex did not change much with longer incubation times (2 right lanes).

The immunoaffinity experiments with 0.096, 0.40 and 1.0 µL of the zymosan A-treated M. sexta hemolymph were performed. The elution fractions were divided into two for use in SDS-PAGE and ESI-MS analysis. Unfortunately, no serpin-protease complex was observed on the western blot membrane or detected in the ESI-MS samples. We speculated that the concentration ratio of serpin-protease complex to free serpin was too low and was therefore difficult to detect with mass spectrometry. Furthermore, the efficiency of the antibody in retarding the serpin-protease complex from the hemolymph was questionable, especially at this small scale. Western immunoblots of *A. gambiae* hemolymph indicated a higher ratio of the complexed to uncomplexedSRPN2 especially after challenging the mosquitoes with *Micrococus luteus*. As a result, we decided to begin experiments with *A. gambiae* samples.

2.4 Immunoaffinity Experiments with *A. gambiae* SRPN2

SRPN2 antibody was purified from 6 mL of rabbit antisera (DIF-5 4)[33] as detailed in the experimental section. The total protein concentration was determined to be 0.23µg/µL.
50 µL of this solution was incubated with Dynabeads® Protein A magnetic beads, without crosslinking. The Ab-coated beads were then incubated with a solution containing 300 ng of SRPN2 recombinant protein. Bound protein was eluted into 2 susequent 20 µL of 0.1M glycine. The western blot membrane is shown in Figure 2.7.

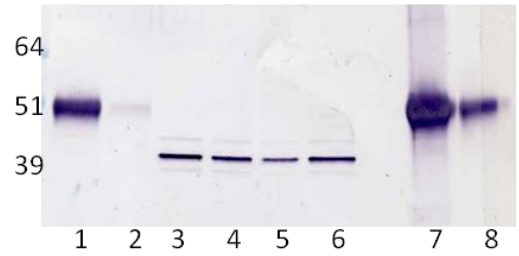

Lane	Identity
1	Ab solution
2	Ab unbound
3	45 ng SRPN2
4	34 ng SRPN2
5	25 ng SRPN2
6	SRPN2 unbound
7	Elution 1
8	Elution 2

Figure 2.7. Recombinant SRPN2 binds poorly to SRPN2 antibody (DIF-5).
The Western blot was prepared with the same antibody. The antibody was bound efficiently by the protein A magnetic beads (compare lane 1 and lane 2). The antibody-coated beads were incubated with a solution of recombinant SRPN2 containing 300 ng of protein. The binding of the recombinant protein to the antibody was very poor as evidenced by the intense band on lane 6 from the unbound protein solution. There was no visible SRPN2 band in the elution fraction.

The efficiency of antibody binding to beads was very high (very faint band in lane 2 compared to lane 1 in Figure 2.7). Unfortunately little or none of the recombinant protein bound to the antibody (no visible SRPN2 bands in lanes 7 an 8, Figure 2.7). Another experiment with hemolymph from 15 mosquitoes showed similar results. It was evident from these results that SRPN2, whether native (from hemolymph) or recombinant, was not binding to the antibody. Similar results were observed with recombinant protein dialyzed into phosphate buffer.
At this point, we decided to work with SRPN2 antisera from a different rabbit. Antibody from antisera DIM-6 3^{33}, was purified and the fractions with most protein combined and dialyzed into 10mM phosphate buffer pH 7.4. Glycerol was added dialyzed antibody solution in a 1:1 ratio and the mixture stored at -21^{o}C until needed. The protein concentration of this mixture was 60 ng/µL. The storage buffer from 80 µL of the magnetic bead suspension was removed and

replaced with a solution containing 14.4 µg of SRPN2 antibody and incubated at room temperature with gentle shaking for 30 min. The beads were then divided into two halves. One half had the antibody crosslinked to protein A on the beads while the other half remained uncrosslinked. Both batches of beads were then incubated with 300 ng each of recombinant SRPN2 protein solution and the bound proteins eluted into 30 µL of 0.1M glycine pH 2.5. The collected fractions were subsequently analyzed with SDS-PAGE and Western blotting. A scan of the western immunoblot membrane is shown in Figure 2.8.

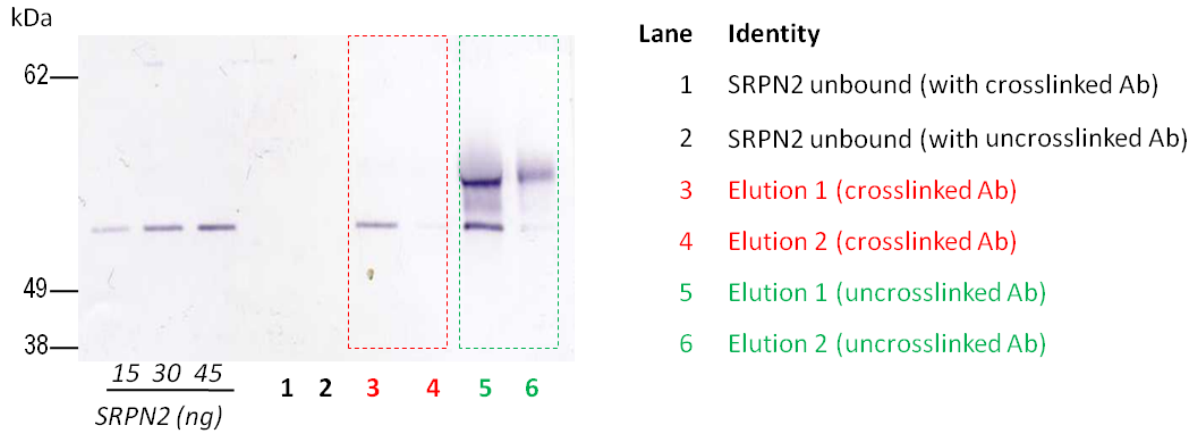

Figure 2.8. purified antibody from rabbit DIM-6 antisera binds recombinant SRPN2.
Western blot prepared with purified antibody from DIF-5 antisera. 80 µL of protein A magnetic beads were incubated with 14.4 µg of purified antibody from DIM-6 antisera. The beads were divided into two and in one half the antibodies were crosslinked to protein A. Both batches of beads were incubated with 300 ng of recombinant SRPN2 each and bound proteins eluted in 15 µL glycine elution buffer twice. Lanes 1 and 2 are from the unbound protein solutions from the crosslinked-antibody beads and the uncrosslinked antibody beads respectively. lanes 3 and 4 (in red box are elution fractions from the crosslinked-antibody beads while lanes 5 and 6 are elution fractions from the uncrosslinked-antibody beads.

An improvement in the antibody binding efficiency to recombinant SRPN2 was observed with the DIM-6 purified antibody compared to the DIF-5 antibody (Figure 2.7). The recombinant protein was also efficiently depleted from the solution following incubation with the Ab-coated

beads. (lanes 1 and 2, Figure 2.8). In the experiment with crosslinked antibodies, about 10-20% of the recombinant protein was recovered in the elution fractions (lanes 5 and 6). There was slightly more in the experiment with un-crosslinked antibodies, though it seemed that not all the bound protein was eluted, judging from the amount of antibody that co-eluted. With the observations from this experiment, it was determined that the previous SRPN2 antibody (DIF-5) poorly bound SRPN2. Encouraged by these results we performed an experiment with hemolymph from 50 *M. luteus*-challenged female mosquitoes. The bound protein was eluted in 50 µL of 0.1M glycine buffer. The membrane in **Figure 2.9** summarizes the results we obtained;

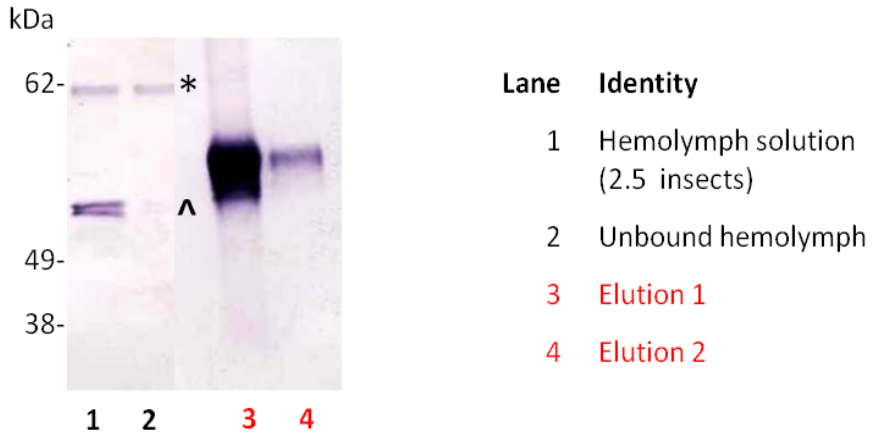

Figure 2.9. Purified antibody from DIM-6 binds native SRPN2 but does not bind SRPN2-protease complex. Western blot was prepared using purified antibody from rabbit antisera DIF-5. Hemolymph from 50 bacteria-challenged female A. gambiae mosquitoes was added to antibody-coated magnetic beads. Lane 1 shows protein from hemolymph equivalent to 2 insects. Lane 2 is unbound protein from hemolymph equivalent to 2 insects following incubation with the antibody-coated magnetic beads. * indicates the SRPN2-protease complex, ^ indicates un-complexed SRPN2. Bound proteins were eluted into 50 µL of elution buffer (glycine-HCl, pH 2.5) twice. 10 µL of the elution fraction used in the Western blot (lanes 3 and 4).

The elution fractions ran on the gel were 20% of the total elution fraction. The proteins were not crosslinked to protein A and this explains the intense band on lanes 3 and 4 due to the

antibody that co-eluted with the bound SRPN2. The un-complexed SRPN2 in the hemolymph solution was depleted from the solution (compare lanes 1 and 2 lower protein bands). Interestingly, the band intensities of SRPN2-protease complex (bands on lanes 1and 2, upper bands) remained largely the same.

A possible explanation for the generally poor binding efficiency of the antibodies is the fact that the antisera was prepared by immunizing rabbits with denatured recombinant SRPN2. As such, we speculated that the binding to native SRPN2 from hemolymph or non-denatured recombinant SRPN2 would not bind as strongly to the antibody. The next set of experiments was aimed at determining if the antigen-antibody binding efficiency would improve if the sample was denatured. Different denaturants were used. We began with the denaturant used to prepare samples for SDS-PAGE. 10 mL of the denaturant was prepared by mixing 1.26 mL Tris (pH 6.8), 2.0 mL glycerol, 6.7 mL ultrapure water, 0.4 g SDS and 0.2 mL β-mercaptoethanol. 0.2 mL of this solution was added to 200 µL of a 0.2 µg/µL solution of SRPN2. The resulting mixture was then heated at 95^{o}C for 5 min, left to cool to room temperature then dialyzed into 10mM phosphate buffer, pH 7.4.

An immunoaffinity experiment was then performed to determine if there would be any improvement in binding efficiency of denatured recombinant protein to the SRPN2 antibody compared to the 'native' recombinant protein. In this experiment, the antibody was crosslinked to protein A on the beads. The Western blot in Figure 2.10 illustrates the results;

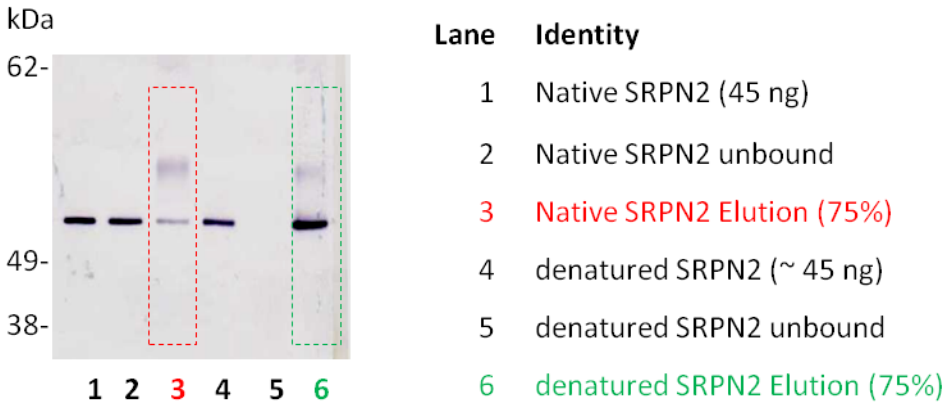

Figure 2.10. Denatured recombinant SRPN2 binds to SRPN2 antibody-coated beads better than the non denatured recombinant SRPN2.

Western blot was prepared with antibody purified from DIF-5 antisera. 2 batches of SRPN2 antibody-coated magnetic beads were incubated with 300 ng of non-denatured recombinant SRPN2 and 300 ng denatured recombinant SRPN2 respectively. Lane 1 was loaded with 45 ng of the non-denatured recombinant SRPN2. Lane 2 is the equivalent volume after incubation with the antibody-coated beads. The lane within the red box was ¾ of the elution fraction from the experiment with the non-denatured SRPN2. Lanes 4-5 are the corresponding lanes to lanes 1-3 with experiments using denatured recombinant SRPN2.

As expected, the denatured recombinant SRPN2 interacted more strongly with the antibody on the beads compared to the non-denatured sample (see Figure 2.10, lane 1 and 2 compared to 4 and 5 respectively). Further, the amount of protein in the elution fraction of the denatured sample was much more compared to the 'native' elution sample (red and green boxes respectively, Figure 2.10).

Unfortunately, similar experiments with hemolymph were not successful and no bands were visible in the elution fractions. The SDS in the denaturing solution was difficult to removve by dialysis and this compromised the quality of the sample. Urea was used instead of the SDS-based denaturant and this worked quite well with the recombinant proteins. (see appendix 2).

The experiments with denatured samples of the recombinant proteins indicated an improvement in binding capacity. In the next set of experiments, we compared the performance of the antibody-coated magnetic beads with urea denatured and non-denatured hemolymph. The antibody used in these experiments was freshly purified and dialyzed into 10mM sodium phosphate buffer. 120 µL of bead suspension was incubated with 21.6 µg of antibody in 180 µL of solution then crosslinked as detailed in the experimental section. The antibody-coated beads were divided into 3 equal portions. Meanwhile, hemolymph from 191 insects was made up to 300 µL with 10 mM sodium phosphate buffer and divided into 3 equal portions. 400 µL of 8M urea was added to one portion. 400 µL of 8M urea containing 2% β-mercaptoethanol was added to another portion while the third portion was refrozen at -80^{o}C until needed. The denatured samples were left at room temperature for 1 hr followed by dialysis into 10mM sodium phosphate buffer at 4^{o}C. The three prepared hemolymph samples were then added to the previously prepared magnetic beads and incubated with gentle shaking at room temperature for 1 hr. 20 µL from each of the hemolymph samples was saved for analysis of binding efficiency. The bound proteins were eluted in 30 µL of 100mM glycine-HCl and neutralized with 2 µL 1M sodium phosphate. SDS-PAGE followed by Western immunoblotting was performed on the collected fractions. The denatured hemolymph samples yielded very little protein in the elution fractions, evidenced by very faint bands of the un-complexed SRPN2 and even fainter band of SRPN2-protease complex. Interestingly, in experiments with non-denatured hemolymph, the SRPN2-protease complex band was observed in the elution fraction lane. Further, it was evident that the complex was depleted from the hemolymph solution. Additionally, both the SRPN2 and SRPN2-protease complex bands were more intense compared to those from the denatured samples (Figure 2.11).

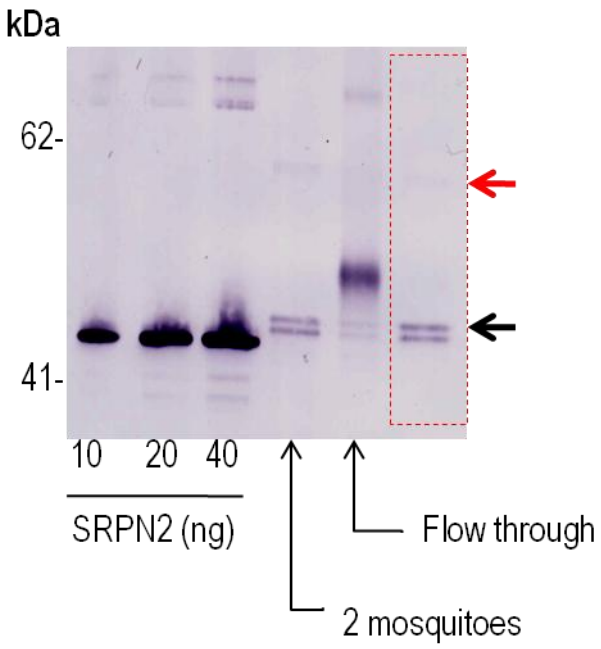

Figure 2.11. Analysis of fractions from immunoaffinity experiments with non-denatured hemolymph. Following incubation of SRPN2 antibody coated beads with hemolymph solution from 60 female anopheles mosquitoes, the proteins retained by the antibodies were eluted in 30 µL of elution buffer, half of which was used for the Western blot in the lane contained in the red box. The red arrow indicates the location of the SRPN2-protease complex while the black arrow shows the SRPN2 band. The Western blot was prepared with purified antibody from rabbit antisera DIF-5.

The faint band at ~62KDa, shown with the upper arrow in Figure 2.11, is most likely SRPN2-protease complex. The intensity of the free serpin band, shown with the lower arrow on the right in Figure 2.11, is very similar to that of the hemolymph from 2 insects. This indicated that the efficiency of the beads in isolating serpins was only ~7%. This percentage was determined from comparing the band intensities of the SRPN2 band and calculating the amount of SRPN2 in terms of insects i.e ((2/30)x100). When the experiment with non-denatured hemolymph from the same batch of insects was repeated with antibody that had been previously stored at -21^{o}C, no detectable bands were observed in the elution fractions. Further, the free SRPN2 and SRPN2-protease complex bands in the hemolymph solution standard and the unbound protein solution

had very similar intensities. These experiments indicated that very little protein was bound by the antibody on the beads.

2.4.1 Immunoaffinity Experiments with KSU 239 Antibody

The SRPN2 antibody used in all the previous experiments were made by immunizing rabbits with denatured recombinant SRPN2 protein solution. We speculated that the poor binding efficiency observed was because the antibody was not strongly binding the native proteins, whether recombinant serpin or from hemolymph. We predicted that antibodies made against native recombinant protein would yield better performing antibodies. This would be an easier route compared to denaturing the samples prior to immunoaffinity precipitation.

Antisera (KSU 239 1/31/13) was obtained from rabbits immunized with solution of recombinant SPRN2 that was not denatured. Recombinant SRPN2 (10 mg) was immobilized on the Aminolink® column. The column was then used to purify SRPN2 antibodies from 4 mL of antisera. The total protein concentration of the fractions with most protein were determined to be, 1.56 mg/mL (total volume = 3 mL) and 0.35 mg/mL (total volume = 2 mL).

Hemolymph from 105 mosquitoes was diluted to 210 µL and 200 µL of this solution applied to the antibody-coated beads. The bound antibodies were eluted into the glycine buffer and neutralized. The elution fraction was divided into two equal halves. One half of the fraction was presented to Dr. Yasuaki (Biotechnology core facility, Kansas State University) for ESI-MS experiments while the other half was used for SDS-PAGE and Western immunoblotting.

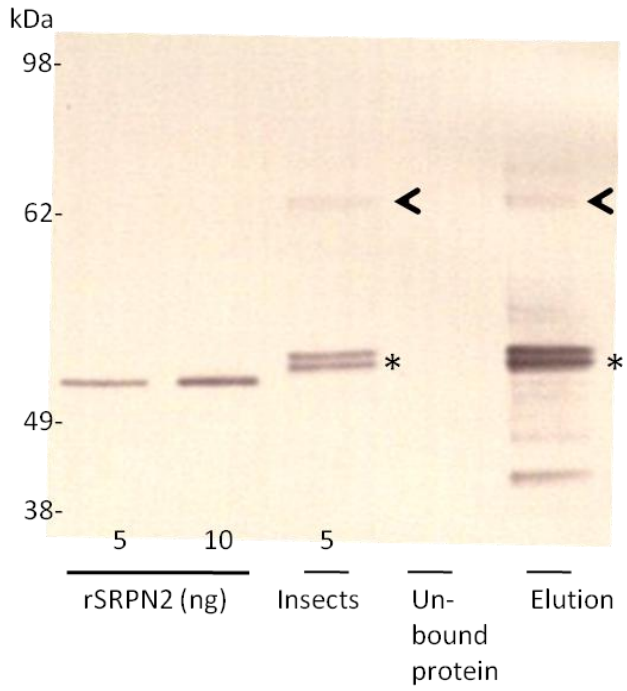

Figure 2.12. Better binding efficiency of SRPN2 and SRPN2-protease complexes is achieved with the use of antibodies against non-denatured SRPN2.

The Western blot was prepared with purified antibody from rabbit antisera DIF-5. Hemolymph from 100 female anopheles mosquitoes was incubated with SRPN2 antibody-coated magnetic beads and the bound protein eluted into 30 µL of glycine buffer. Half of the elution fraction was used for this Western blot (extreme right lane). The arrows show the location of the SRPN2-protease complex band. The asterisks show the uncomplexed SRPN2 band.

As predicted, there was great improvement in binding efficiency of the antibodies. The antisera prepared against non-denatured recombinant SRPN2 had better recognition of the native SRPN2 and the SRPN2-protease complexes from mosquito hemolymph. The whole immunoprecipitation experiment was repeated with hemolymph from another 105 mosquitoes from the same population, and the fractions collected were used to perform SDS-PAGE on 2 gels. Silver staining was performed on one gel while Western immunoblotting was performed on the other gel (Figure 2.13). The aim of this step was to determine whether there was non-specific binding of proteins on the beads and to check the reproducibility of the results earlier obtained.

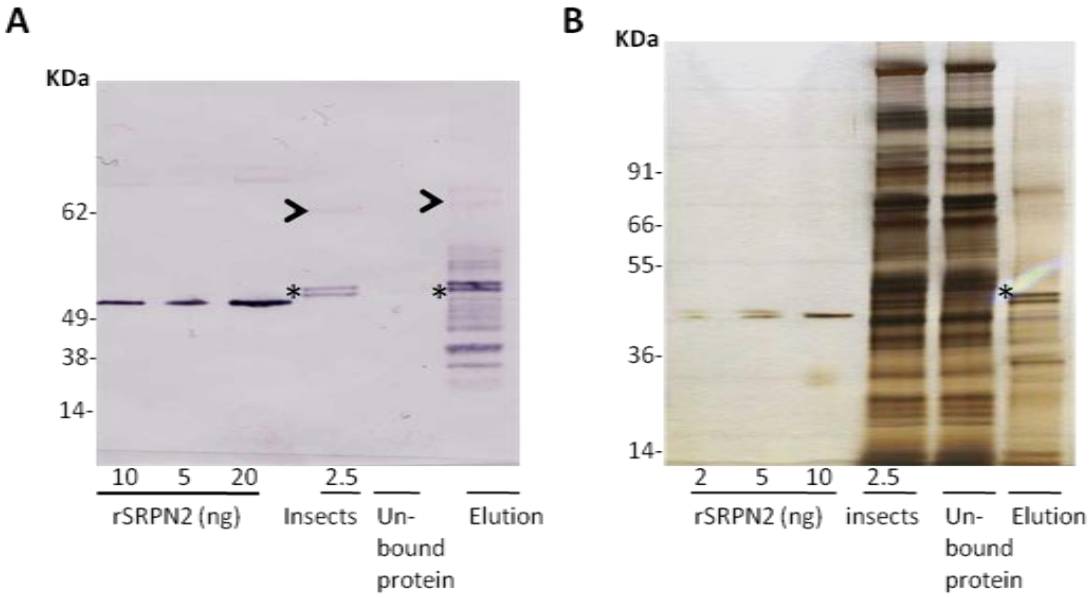

Figure 2.13. SRPN2 antibody binds both non-complexed SRPN2 and SRPN2-protease complex.
A, B, Western blot and Silver stain analysis of elution fraction from immunoaffinity precipitation of SRPN2 and SRPN2-protease complexes from hemolymph equivalent to 100 mosquitoes. The Western blot analysis was performed using purified rabbit anti-SRPN2 (DIF-5 4). *Asterisks,* non-complexed SRPN2; *Arrow heads,* SRPN2-protease complex.

The mass spectrometry analysis was performed by Dr. Yasuaki (The Biotechnology core facility, Kansas State University). The elution fraction was subjected to trypsin digestion followed by an enrichment step on a C18 liquid chromatography column prior to ESI-MS. MASCOT (Matrix Science) search engine was then used to analyze the data generated from the mass spectrometer in order to identify the proteins. The peptides were compared with those from the NCBI database. Table 2.2 shows the identity of the proteins that got the most hits. A score > 54 indicates protein identity or extensive homology. This was the case in all but one of the proteins in the table. Apart from SRPN2, the proteases, CLIPA6, CLIPA7, serine protease 14D (CLIPB4), CLIPB14 and CLIPB15 were also identified.

Table 2.2. Summary of ESI-MS MASCOT search results from NCBI database.

Accession	Score *	Mass	Num. of matches	Num. of sequences	emPAI **	% sequence coverage	Description	Peptide sequences
gi|116041593	425	46528	12	7	0.98	35	serpin 2 [Anopheles gambiae]	K.ILLTLIYEASDTSFGNAVSNTK.R R.ELSSVIQNDNIDHTR.S K.VSYSNPTQTAATINNWVSEHTNGR.L R.EIVTPDSLEGAVITLVNVIYFK.G K.GLWTYPFPEVANNVKPFYGTR.G K.FDFSEQLNEPLQQVGIR.E K.AGITINELGSEAYAATEIQLVNK.F
gi|159145445	145	23429	5	4	0.49	50	serine protease inhibitor 2 [Anopheles gambiae]	R.ELSTVIQNDNIEHTR.S K.VSYSNPTQTAATINNWVSEHTNGR.L R.EIVTPDSLEGAVITLVNVIYFK.G K.GLWTYPFPEVANNVKPFYGTR.G
gi|58394427	76	81892	2	2	0.08	2	CLIPA7	R.FNPDNECEDYLLK.C R.LGEWDTQTK.N
gi|187441820	72	19426	1	1	0.17	8	CLIPB15	K.FSNSPTCGAQQLADR.I
gi|347972684	58	46609	3	3	0.15	7	CLIPA6	K.GGPCGGEAVCIQK.Y K.TEEVLGQLR.E K.AGTYQVILK.K
gi|2253393	79	40252	3	3		10	Serine protease14D	K.IDEFPWTALIEYEKPNGR.F K.IIVHPGYNLQDK.S R.EINYSSTIR.A
gi|118793181	45	30928	1	1	0.11	3	CLIPB14	K.APPTSVPDAR.R

*** score>54 indicates protein identity/extensive homology**

**** exponentially modified protein abundance index[46]**

2.5 Discussion

Immunoaffinity chromatography is a powerful separation technique capable of isolation, purification and pre-concentration of specific target analytes from complex matrices. This property makes it an ideal choice for the separation of proteins from mosquito hemolymph. An important advantage of immunoaffinity chromatography is that miniaturization does not affect its efficiency and is only limited by the detection limit of the target protein. In the experiments discussed in this chapter, protein A-coated magnetic beads were employed for the immunoaffinity precipitation of SRPN2-protease complexes from hemolymph of female

Anopheles mosquitoes. The use of magnetic beads was beneficial on several fronts compared to beads prepared from non-magnetic materials; first, it was not necessary to confine them in a column and their use in a batch format simplified the experimental procedure. Secondly, in batch format, samples and buffers were added in discrete volumes and buffer carry over was minimal. This provided for collection of eluted samples in the smallest volume possible and therefore in the highest concentration possible. This is was significant in the experiments discussed in this chapter because a smaller hemolymph sample was sufficient for the analysis of the target proteins. It was important at this small scale to maximize the binding efficiency of the antibody-coated magnetic beads. One strategy to achieve this was to use purified SRPN2 antibody instead of antisera. This way, the protein A sites on the magnetic beads would be occupied by SRPN2 antibody only. This translated to more binding sites for SRPN2 and its protease complexes from hemolymph. The antibody was crosslinked to protein A on the beads using dimethyl pimelimidate (DMP). DMP contains two imido esters on each end of its structure and each reacts with primary amines in basic conditions[47] to covalently link the Fc region of the antibody to protein A on the beads. During the elution step, only the bound protein got pulled down, leaving the antibody still attached to the beads. The signal to noise ratio was greatly improved considering the fact that the antibody concentration was orders of magnitude higher than the proteins of interest.

The only known function of SRPN2 in the *Anopheles* mosquito is to inhibit the PPO pathway that causes melanization, by forming covalent complexes with CLIP proteases in the PPO pathway. SRPN2 has been proposed as a potential target for late life acting (LLA) insecticides that target older mosquitoes with less propensity of developing insecticide resistance.[32] SRPN2 depletion through gene silencing resulted in increased formation of

melanotic tumors and consequently reduced the longevity of the *A. gambiae* female mosquito.[32] SRPN2 inhibits CLIPB9 that cleaves proPO to the active form PO. Other molecular targets of SRPN2 have not been extensively studied because of the small size of the mosquito that limits sample size.

To the best of our knowledge, this is the first time that immunoaffinity chromatography has been employed to purify and enrich SRPN2-protease complexes from native hemolymph.

ESI-MS analysis on the elution fractions determined the presence of Clip domain proteases, CLIPA6, CLIPA7, CLIPB14, CLIPB15 and serine protease 14D. It is established that SRPN2 regulates the PO pathway at its final stages by irreversibly binding to CLIPB9.[34] However, SRPN2 interacts with other proteases but there is still a lot that is unknown on the identities and mechanisms of these proteases. CLIPB4, -14 and -15 are important in promoting melanization in *A. gambiae*.[48-51] CLIPA7 expression increases upon infestation of mosquito by the plasmodium parasite.[50] The ESI-MS results strongly suggests that these proteases interact with SRPN2. Other experiments are needed to verify these results. Work is on-going to prepare antibodies to some of the proteases to establish, by Western blotting whether the complex comprises of the particular proteases.

2.6 Conclusion

Melanization is one of the potent immune response mechanism employed by invertebrates to fight microbial infestation. The PPO pathway that is responsible for the reactions that produce eumelanin are tightly regulated by clip domain serine proteases (CLIPS) and serpins. Of particular interest is *A. gambiae* SRPN2 that negatively regulates the PPO cascade by forming irreversible complexes with proPO activating CLIPS. SRPN2 is a potential target in the

development of novel insecticides would be less prone to parasite resistance. The targets of SRPN2 are poorly understood because the small size of the mosquito results in minute sample volumes that are difficult to collect and more challenging to analyze. An immunoaffinity chromatography system was developed to comfortably handle the small volume hemolymph samples. SRPN2 antibody-coated magnetic beads were employed, in batch format, to isolate SRPN2-protease complexes from hemolymph of bacteria-challenged female *A. gambiae* mosquitoes. The isolated proteins were then analyzed by SDS-PAGE and ESI-MS. On the Western blot, a high MW band was visible at ~ 62 kDa, in the lane loaded with the elution fraction. The same band appeared in the hemolymph solution lane but was absent in the lane loaded with the supernatant solution following incubation with SRPN2 antibody -coated beads. ESI-MS analysis of the elution fraction identified the following proteases; CLIPB15, CLIPB14, serine protease 14D, CLIPA6 and CLIPA7. These proteases have been determined to participate in the PPO pathway, although their specific roles and mechanisms are still not well established.

Chapter 3 - Integrated Microfluidic Device for Monitoring Nitric Oxide Production in Single Cells

The majority of this chapter has been submitted for publication as: Eve C. Metto; Amita Sharma; Karsten Evans; Patrick Barney; Anne H. Culbertson; Dulan B. Gunasekara; Giuseppe Caruso, Matthew K. Hulvey, Jose Alberto Fracassi da Silva, Susan M. Lunte; Christopher T. Culbertson *Analytical Chemistry*, **2013**

3.1 Introduction

Nitric oxide is an important signaling molecule that is involved in a number of physiological processes including, blood pressure regulation,[52] neurotransmission and the immune response.[53-55] The reaction of nitric oxide with superoxide in cells can result in the production of peroxynitrite and other reactive nitrogen species that have been linked to a number of diseases including cancer,[56,57] diabetes[58] and neurodegenerative diseases such as Alzheimer's, Parkinson's and stroke.[59-63]NO has also been shown to promote apoptosis in cancer cells.[64] Nitric oxide is generated by nitric oxide synthase (NOS) *in vivo*. There are three forms of nitric oxide synthase. Two of these, endothelial nitric oxide synthase (eNOS) and neuronal nitric oxide synthase (nNOS) are constitutively expressed enzymes and calcium dependent. These forms of NOS produce a constant level of NO over time. However, a third form of NOS, inducible nitric oxide synthase (iNOS) is up-regulated during inflammation or infection. This form of NOS is found in a variety of cell types including macrophages, endothelial cells, neurons, microglia and lymphocytes.

Many studies of NO production have been performed at the bulk cell level.[65,66] However, there is evidence that the production of NO is not uniform among a population of cells and is

dependent on the level of iNOS expression in those cells. While NO differences can be qualitatively determined in individual cells using fluorescence imaging, more quantitative methods need to be developed[67] so that the effect of cell type, cell cycle stage and stimulant type on the production and release of nitric oxide can be studied.[68-71] The half-life of NO in the cell is very short. It is known to react with superoxide to produce peroxynitrite and also to be oxidized to generate N_2O_3 *in vivo*. These molecules can nitrate proteins which has been proposed as a signal for programmed cell death.[72,73] There have been only a few reports measuring nitric oxide production in single cells. In particular, Sweedler's group has measured nitric oxide in single neurons isolated from Aplysia by capillary electrophoresis[74-80] Amatore's group has also measured the release of NO from single macrophages using chronoamperometry at platinized carbon microelectrodes.[81] Intracellular concentrations of NO have also been determined using capillary electrophoresis with fluorescence detection. [67,78,80]

The analysis of single cells by conventional capillary electrophoresis, however, is a slow and tedious process. Since single cell analysis by CE is difficult to automate, the throughput is usually on the order of less than a dozen cells per day. [82,83] A major challenge when using capillaries for single cell analysis is getting rid of cell debris that often adheres to the capillary wall, causing signal distortion and at times blockage of the lumen.[73] Because of this the capillary has to be either replaced or cleaned between runs.

A promising approach to improve throughput and automate single cell analysis is the use of microfluidic devices. These devices have several advantages over capillary-based single cell analysis techniques including 1) faster analysis times and thus higher throughput, 2) smaller sample volume requirements that allow for improved detection limits, 3) amenability to automation, 4) ability to integrate several analytical procedures such as cell transport, cell lysis

and sample injection onto a single platform and, 5) better and more precise fluid control. [69,83-86] Single cell analysis on microfluidic devices has become very popular and several excellent reviews are written on the topic annually.[69,82,83,87-92] A wide variety of approaches are used including single cell cytometry,[93] microwell array and microhurdle trapping and imaging or trapping with subsequent lysis and lysate analysis[82] among others. Electrochemical detection of species released from cells is also popular.[65,94-96]

This chapter is focused on further expanding the capabilities of electrokinetic and hydrodynamic flow-based single-cell trapping and analysis devices. Transporting cells individually to an analysis system where they can be quickly lysed, the lysate injected into a channel, and the analytes separated and detected, provides the ability to analyze and quantitate a much larger number of analytes than is available with many of the other approaches mentioned above. Most reported single cell analysis experiments of this type on microfluidic devices, however, have been proof of principle studies on a small number of cells using test analytes,[69] although in a few cases native intracellular molecules[97-100] have also been measured. Only a couple of devices have been reported that have detected either test analytes[87] or native molecules[101] in more than 100 cells. To the best of our knowledge this is the first example of a microfluidic device being used to serially measure and quantitate the change in an intracellular molecule, i.e. NO, in response to an external stimulation in 100's of individual cells. A reason for this lack of papers using these devices for high throughput analysis may be due to the challenge of reproducibly controlling cell transport, lysis, and injection on chip and performing these steps quickly. In this chapter, we report an improved microfluidic device designed for single cell analysis. The PDMS/glass hybrid chip was modeled on an earlier etched glass design used in our lab and by others.[69,87,102] The geometry and of the lysis and injection intersection has been modified to significantly

improve the reproducibility of the lysate injection process. The new design exposes the cell to the electric field longer to ensure complete lysis and aligns the analyte plug with the electric field to improve the injection. The additional exposure time also allows the use of lower DC field rather than an AC electric field. In addition, unlike the previous all-glass devices, PDMS-based chips are easy to fabricate and they do not require elaborate preparation steps before the experiments. The PDMS/glass chip was used to measure NO production using a diaminofluorescein-based probe in over 200 hundred cells within 20 minutes. The labeled cells were transported to an intersection where they encountered high DC voltage that generated cell lysis followed by electrophoretic injection and separation of lysate, prior to laser induced fluorescence (LIF) detection. The results compare nicely to recently published bulk cell studies performed for the analysis of NO. [74]

3.2 Materials and Methods

3.2.1 Reagents and Materials

Sodium borate, bovine serum albumin (BSA), Tween-20 and acetonitrile were all obtained from Fisher Scientific (Pittsburgh, PA). Sodium dodecyl sulfate and anhydrous dimethyl sulfoxide (DMSO) were supplied by Sigma-Aldrich (St. Louis, MO). SU-8 2010 was purchased from MicroChem Corp. (Newton, MA). The SU-8 developer, 2-(1-methoxy) propyl acetate, was obtained from Acros (Morris Plains, NJ). Silicon wafers, 4 inches in diameter, were purchased from Silicon Inc. (Boise, ID). Sylgard 184 PDMS prepolymer and curing agent was purchased from Dow Corning (Corning Inc., Corning, NY). Ultrapure water was generated from a Barnstead E-pure system (Dubuque, IA).

3.2.2 Microchip Fabrication

The microfluidic device (Figure 3.1B) was fabricated using established soft lithography procedures.[26] Briefly, SU-8 2010 negative photoresist was spun to a thickness of ~20 µm on a 100 mm silicon wafer using a spin coater (Laurell Technologies Corp., North Wales, PA). The coated mask was then placed on a 65^0C hot plate for a 2 min soft bake followed by a 4 min hard bake on a 95^0C hot plate. A mask containing the microfluidic channel pattern, created using AutoCAD LT 2006 (Autodesk, San Rafael, CA), was placed on the wafer that was then exposed to ultra violet light using a UV exposure system (ThermoOriel, Stratford, CT). The unpolymerized photoresist was washed off using SU-8 developer, rinsed with isopropyl alcohol and blow dried with nitrogen. A 10:1 w/w mixture of PDMS prepolymer and curing agent was then poured over the mold and cured for at least 50 min at 80^oC. Access holes to the channels were drilled on a 75 × 50 mm glass slide (Corning Inc., Corning, NY) using a 2 mm diamond tipped drill bit (Rio Grande, Albuquerque, NM) and fitted with glass reservoirs using epoxy resin (Epoxy Technology, Billerica, MA). A nanoport assembly placed on reservoir 5 (Figure 3.1), a micro-splitter valve, threaded adapters and PEEK tubing, all from Upchurch Scientific (Oak Harbor, WA) were used to connect the microfluidic device and the syringe pump.

The cured PDMS was peeled off the mold and placed over the glass slide with the ends of the channels aligned with the access holes on the glass slide. Another glass slide was placed on the top and the excess PDMS trimmed off. The channel dimensions were determined by measuring the height and width of the features on the silicon wafer mold using a profilometer (Ambios Technology, Santa Cruz, CA). The channels were 19 µm deep, corresponding to the height of the features on the mold. The narrow sections of the channels were 50 µm wide. The wide sections of the channel from reservoirs 1, 2, 3 and 4 were 160 µm while that from reservoir 5 was 500 µm (Figure 3.1B).

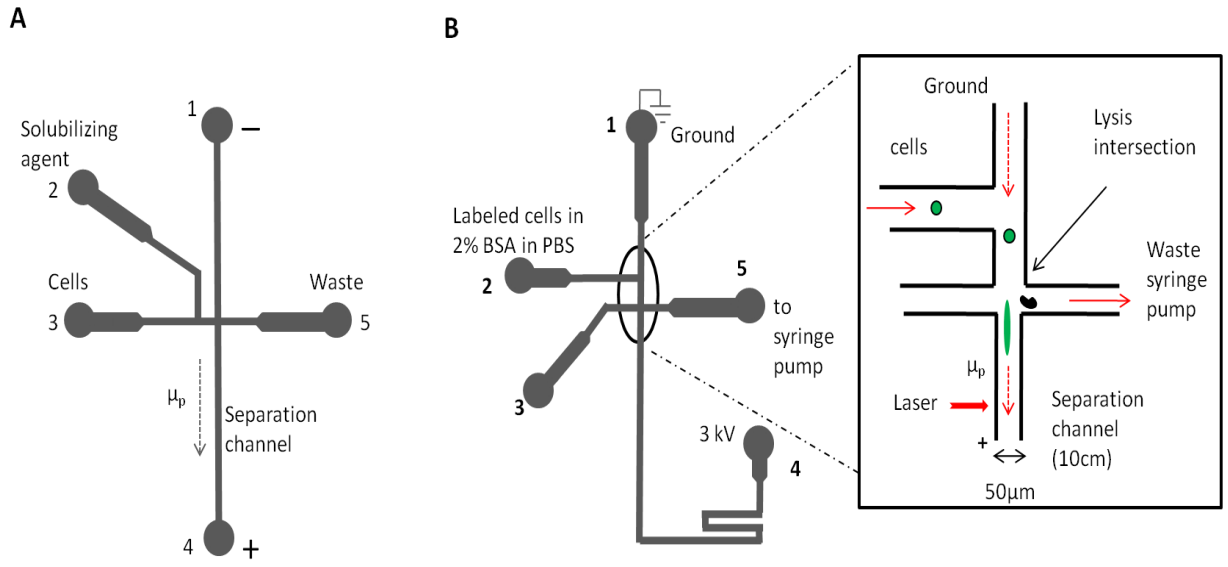

Figure 3.1. A Initial chip design. B Schematic of improved microfluidic chip used for single cell lysis experiments. Lysis intersection of the microchip shown in B. The solid arrows show the direction of bulk fluid flow while the broken arrows show the direction of the electrophoretic migration (μ_p).

3.2.3 Cell Culture

Jurkat cells from the Jurkat Clone E6-1 cell line (ATCC TIB-152 American Type Culture Collection, Rockville, MD) were cultured in RPMI 1640 medium containing 10% (v/v) fetal bovine serum, L-glutamine (2mM), penicillin (100 µg/ml) and streptomycin (100 µg/ml). The cells were maintained in a humidified environment at 37^0C and 5% CO_2 and cultured in 25 mL polystyrene culture flasks (Becton Dickinson Labware, Europe). Cells were passaged every 2-3 days to avoid overgrowth.

3.2.4 LPS Stimulation Protocol

NO production in cells was stimulated using purified lipopolysaccharide (LPS) from the *Escheria coli* line 0111:B4 (Sigma Aldrich, St, Louis, MO). 1.5 µL of 25 µg/mL LPS was

administered per ml of cell suspension of healthy Jurkat cells and allowed to incubate for 1-3 hours. An unstimulated (native) flask of Jurkat cells from the same population was incubated under the same conditions as a control for the stimulation experiment.

3.2.5 Sample Preparation

The cells were labeled with DAF-FM DA, which is fluorogenic and membrane permeable. Once inside the cell, DAF-FM DA is hydrolyzed by non specific cytosolic esterases to form 4-amino-5-methylamino-2',7'-difluorofluorescein (DAF-FM). The hydrolyzed dye further reacts with partially oxidized species of NO (N_2O_3) to form a triazole (DAF-FM T) which has a high fluorescence yield.[67] We co-labeled the cells with 6-CFDA, which is also fluorogenic and membrane permeable and is hydrolyzed by esterases to yield a charged fluorescent moiety that is membrane impermeable. We used 6-CFDA as an internal standard to correct for variances in fluorescence intensity when using different devices. Also, the fluorescence yield of 6-CFDA is not affected when cells are incubated with LPS. The dye solution was prepared by adding appropriate volumes of the stock solutions prepared in 99.9% DMSO to enough sterile PBS to make 2μM dye solution. To load the dyes, 1 mL of the cell suspension was centrifuged at 2000rpm for 1 min and the supernatant discarded. The cells were then re-suspended in the dye solution and incubated for 20 min at 37^0C on a heat block. Another centrifugation was performed at the same conditions to remove the dye solution and the labeled cells were re-suspended in RPMI media containing 2% BSA, prior to experiments.

3.2.6 Microchip Operation

The separation buffer consisted of 25mM sodium borate, 20% v/v acetonitrile, 2% w/v bovine serum albumin, 0.6% w/v Tween-20 and 2mM SDS. Initially, all the reservoirs were filled with the separation buffer by applying reverse pressure facilitated by a vacuum pump.

Reservoir 5 (Figure 3.1) was evacuated and replaced with a suspension of the fluorescently labeled cells. The waste reservoir was threaded to provide the connection, via PEEK tubing, to a 1000 µL glass syringe on a syringe pump (New Era Pump Systems Inc., Farmingdale, NY). Cell transport and fluid flow in the channel manifold was achieved by setting the syringe pump at withdrawal mode at a flow rate of 0.25 µL/min. Cell lysis and subsequent electrophoretic injection and separation were achieved by applying 3 kV using a high voltage supply (Spellman® High Voltage Electronics, Hauppauge, NY), across reservoirs 1 and 4 (Figure 3.1).

3.2.7 Detection

A multi-line Argon-ion laser (MellesGriot Laser Group, Carlsbad, CA) was used as the excitation source. The 488nm beam was selected using a dispersive prism and then reflected off a series of mirrors and directed into a Nikon eclipse TS100 microscope (Nikon Instruments Inc., Melville, NY) through the rear port and via a 20X objective (Plan Fluor, Nikon Japan) to the microscope stage. The beam was focused onto a small spot in the separation channel, 5 mm below the lysis intersection. The fluorescence emissions from the dyes were detected by a photomultiplier tube (Hamamatsu Instruments, Bridgewater, NJ) attached to the trinolucular port of the microscope. The signal was amplified using a low noise current preamplifier at 1µA/V with 100Hz low-pass filter (Stanford Research Systems, Sunnyvale, CA) and sampled at 100Hz using a PC1-6036E I/O card (National Instruments, Austin, TX). The program controlling the high voltage power supply and data acquisition was written in-house using LabVIEW (National Instruments, Austin, TX). Data analysis was performed using Igor Pro (WaveMetrics, Portland OR).

Video images of the experiment were collected using a digital color video camera (ExwaveHAD Sony Corporation, Japan) mounted on the side port of a Nikon TE-2000-U

inverted microscope (Melville, NY). Frame grabs retrieved in Image J (NIH) were used to calculate the flow rate of the analytes down the separation channel.

3.3 Results and Discussion

A modified microfluidic device was developed for the determination of nitric oxide production in single T-lymphocytes (Jurkat cells). The initial objective was to develop a more efficient microfluidic design for transporting and lysing cells that could be used to analyze several hundred cells in a short period of time. This device was then used to monitor NO production in native and stimulated Jurkat cells. Finally, the average results from single cell analysis were compared to previously published bulk cell results from our groups[74]

3.3.1 Microchip Design for Single Cell Lysis

A wide variety of microchip designs have been previously reported for single cell analysis. To the best of our knowledge, there have been only a couple of very recent reports[103,104] in which more than 30 cells have actually been quantitatively analyzed by such devices. One reason for the lack of such reports is due to the difficulty in setting up reproducible hydrodynamic flows on these chips for fast cell transport, efficient cell lysis and lysate injection. One of the goals of this project, therefore, was to develop a design that was easy to implement and that could be used routinely to analyze hundreds of cells in a short period of time. Our initial approach involved the use of our previously published design shown in Figure 3.1A.[69] In this design the cells were loaded into reservoir 3 and flowed through the intersection to waste (reservoir 5). However, we found that reproducible injection of the cell lysate was difficult to realize with this design due to difficulty in precisely controlling the volumetric flow rates in the channel manifold using an external syringe pump. The flow rates on these devices are in the low nL/min range, and the flows from all of the channels at the lysis intersection must be carefully

balanced in order to generate reproducible and complete injection of the lysate from the cell into the separation channel. Unpredictable changes in flow resistances over the course of a run due to partial obstructions in the various channels and small changes from device to device in terms of flow resistance make it difficult to reliably adjust the flow. In addition, there is a lag time in terms of when the flow rate is changed on the external pumping device and when the change is seen at the lysis intersection.

In order to improve the ruggedness and operation of the device, we altered the manner with which the cells were transported to the channel intersection section of the chip (region marked with black circle in Figure 3.1B). In the new design, cells are placed in reservoir 2 and are transported to the lysis area of the chip using the hydrodynamic flow generated by a syringe pump in withdrawal mode at reservoir 5 (Figure 3.1B). In this configuration, the cells make a 90˚ turn into the main channel where they encounter a DC electric field that is sufficient to lyse the cells. The lysate is then electrophoretically injected into the separation channel while the cell debris is hydrodynamically shunted to a waste channel.

Figure 3.2 shows consecutive image frames grabbed from a video demonstrating the lysis of individual Jurkat cells loaded with Oregon green using this device. The first image, Figure 3.2A, shows cells approaching the lysis channel. In the second image (Figure 3.2B), the cell has entered the lysis channel and is lysed by the electric field. In the next two frames (Figure 3.2C and Figure 3.2D), the fluorescent lysate is seen travelling into and down the separation channel electrophoretically towards the anode. The velocity of the lysate was 1.44 mm/s. It took less than 33 ms, the length of time between consecutive video frames, to completely lyse the cell. The cell debris was transported into the waste channel more efficiently with this design than previous designs (see Figure 3.2E). In addition to the cell transport redesign, the flow rates on this device

were more easily controlled by inserting an adjustable flow splitter into the line between the chip and syringe pump (Figure 3.1B).

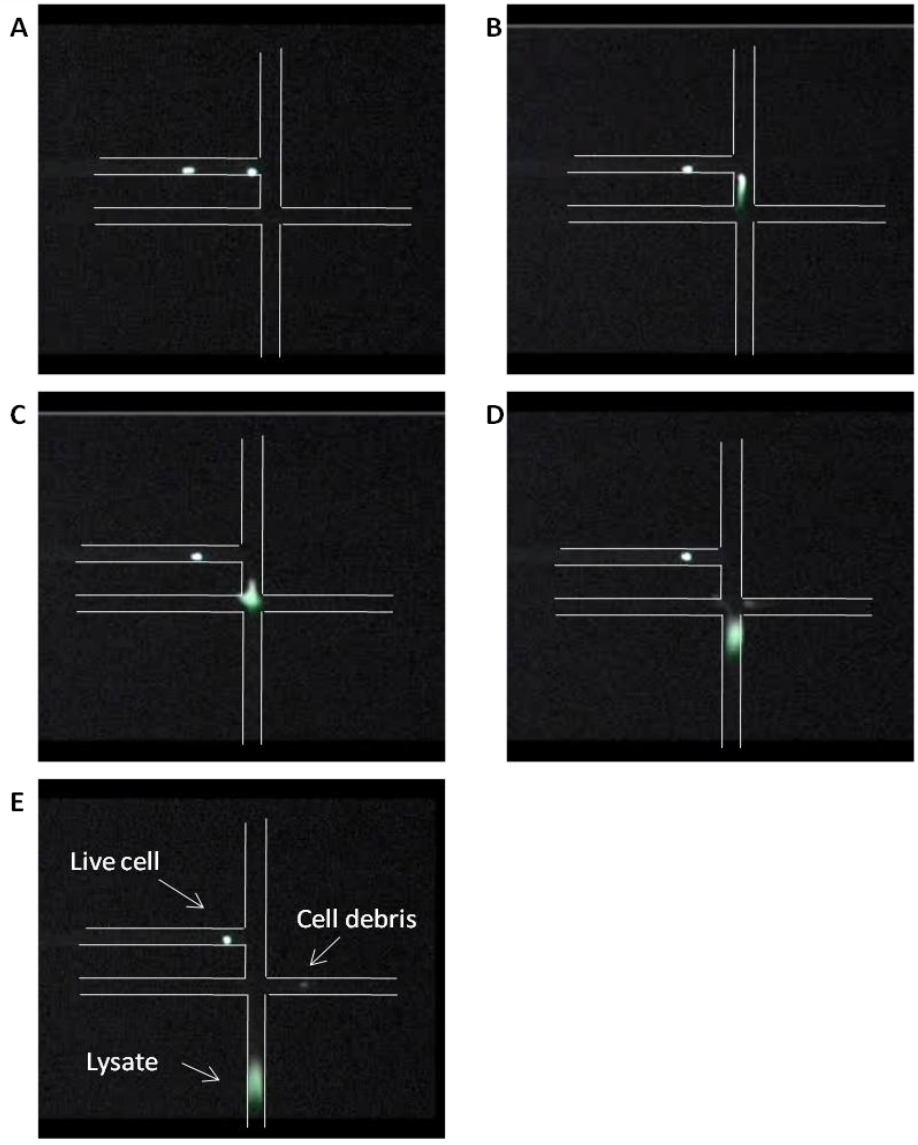

Figure 3.2 Still images obtained from a video of Jurkat cells lysing. The cells in A are hydrodynamically transported towards the lysis intersection. In frame B,the cell at the intersection encounter an electric field that causes them to lyse. In frames C-E, the cell lysate is electrophoretically transported down the separation channel while the cell debris gets shunted to the waste channel.

A major advantage with this new design is that a DC electric field could be used for cell lysis rather than the high voltage AC electric field previously reported,[69] This is important as the

high field AC requires a specialized and expensive generator. In addition, the DC electric field strength necessary for consistent cell lysis and lysate injection was less than half that of the previously reported required AC electric field strength.[69] The voltage applied between reservoir 1 and 4 (Figure 3.1B) generated a field strength of ~ 375V/cm in the cell lysing region of the chip. The significantly lower field strength requirements are due to the significantly longer residence time in the lysis field and the fact that the cell lysate does not need to change migration direction in order to get injected into the separation channel.

In order to reduce cell membrane adhesion in the chip, all of the channels were coated with 2% BSA. BSA also minimized the electroosmotic flow in the separation channel. Under these conditions, the electrophoretic mobilities of the two negatively charged reporting dyes used for the experiments described below were greater than the electroosmotic flow and, therefore, travelled towards the anode upon injection into the separation channel.

3.3.2 Lysate Separation Efficiency

In order to perform very high throughput analysis of single cells, it is crucial that the electrophoretic separation is fast and that the peaks exhibit high separation efficiencies. Unfortunately with this device design, we were not able to directly calculate the number of theoretical plates from the experimental set up because the cells entered the intersection randomly during any particular run. Instead, lysate migration velocities were calculated from videos of the lysate migration under the same separation conditions as that used to obtain the single point separations. The calculated migration velocity (1.44 mm/s for CFDA) from these videos was used to convert the temporal peak variances measured on the electropherograms to spatial variances so that the peak dispersion could be calculated and compared to predicted values. The predicted (or theoretical) peak dispersion values were calculated based upon the

published diffusion coefficient of fluorescein [105] together with the peak broadening expected from the parabolic flow generated in the separation channel from the syringe pump.

3.3.3 Fluid Resistance Calculation

The fluidic resistances in the channels of the cell lysis chip were calculated as reported in the microfluidic hydraulic resistance wikibook at

http://en.wikibooks.org/wiki/Microfluidics/Hydraulic_resistance_and_capacity

where the pressure drop (ΔP) across the device is equal to the hydraulic resistance (R_h) times the volumetric flow rate.

. $$\Delta P = R_h Q \qquad \textbf{(3.1)}$$

The hydraulic resistance for a rectangular channel is given as follows:

$$R_h \sim \frac{12\mu L}{wh^3\left((1-0.630^h)/w\right)} \qquad \textbf{(3.2)}$$

where μ is the solution viscosity, L is the channel length, w is the channel width, and h is the channel height.

The resistance in two channels in series is: $R_h = R_{h1} + R_{h2}$ **(3.3)**

The resistance in two channels in parallel is: $\frac{1}{R_h} = \frac{1}{R_{h1}} + \frac{1}{R_{h2}}$ **(3.4)**

The dimensions for all of the channels leading to the channel to which the syringe pump was attached, i.e. channel 5 in Figure 3.1, were used to calculate the total fluidic resistance according to the equations above. The fraction of the total resistance for the separation channel,

i.e. channel 4 was then calculated and the flow from that channel compared to the flow from the rest of the channel network was determined. The fluidic resistances in the channel manifold were designed so that the overall flow out of the separation channel was only about 3% of the flow going into channel 5 (Figure 3.1B).

3.3.4 Calculation of Diffusion Coefficient

Consecutive frame grabs of the cell lysis video were used to determine the flow rate and migration times of the lysate in the separation channel. These values were then used to calculate the diffusion coefficient which is simply the slope of the line in a graph of the spatial variance vs. the migration time (Figure 3.3). The experimentally determined apparent diffusion coefficient was 1.1×10^{-5} cm^2/s. The predicted apparent diffusion coefficient was 2.8×10^{-6} cm^2/s.[105] The diffusion coefficient is ~3 times that of a molecule of similar size. Considering the contributions from diffusion and the hydrodynamic (parabolic) flow in the separation channel, and given the crude and indirect nature of these measurements, the agreement is remarkably good and shows that the separations are behaving as expected.

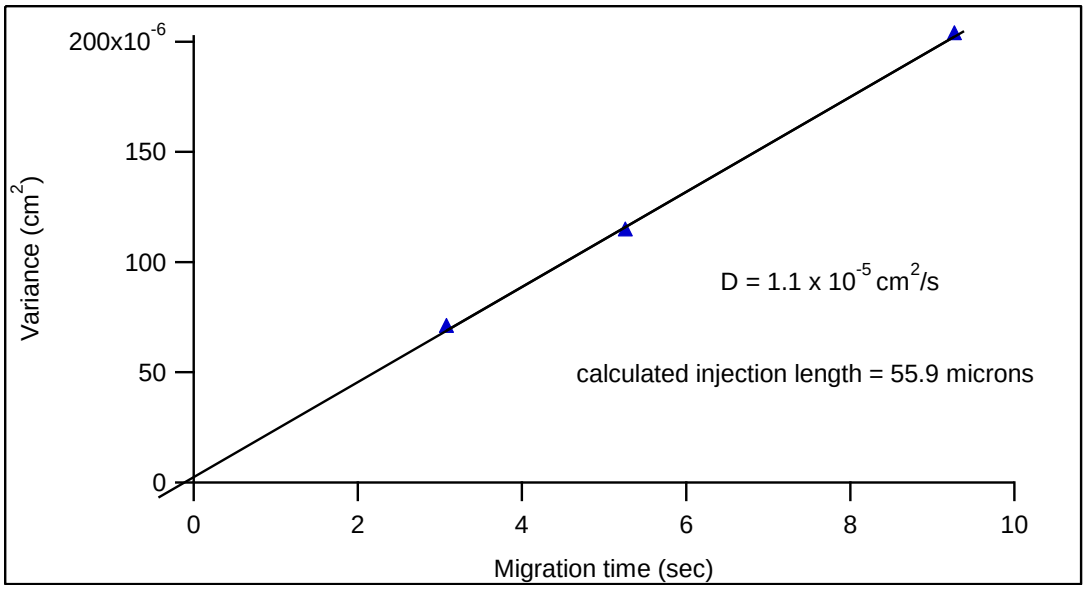

Figure 3.3. Determination of diffusion coefficient of fluorescently labeled species in cell lysate. Frame grabs from a video of the separation channel were used to determine distance traveled and hence migration time.

3.3.5 Measurement of Nitric Oxide Production in Jurkat Cells

The optimized device described above was used to examine nitric oxide production in Jurkat cells. The production of nitric oxide by these cells was measured in bulk previously by our groups using microchip electrophoresis with LIF detection, making direct comparison of the bulk cell measurements with those of single cell distributions possible.[74]

The cells were stimulated with lipopolysaccharide (LPS) which increased the expression of induced nitric oxide synthase (iNOS) and resulted in increased NO production. Control cells were treated in the same manner but were not exposed to LPS. The intracellular production of nitric oxide in the cells was measured using DAF-FM diacetate. The cells were also co-labeled with 6-CFDA. 6-CFDA was used as an internal standard to account for variation in fluorescence intensity when using different microchips and to account for cell size (volume) differences. The fluorescence yield of 6-CFDA was not affected by the presence of intracellular nitric oxide.

The analytes present in the cell lysates were detected using laser-induced fluorescence at a distance of 5mm from the intersection on the separation channel. Figure 3.4 shows a typical electropherogram obtained for stimulated cells. We designed the experiment so that data was collected for 120 s per run.

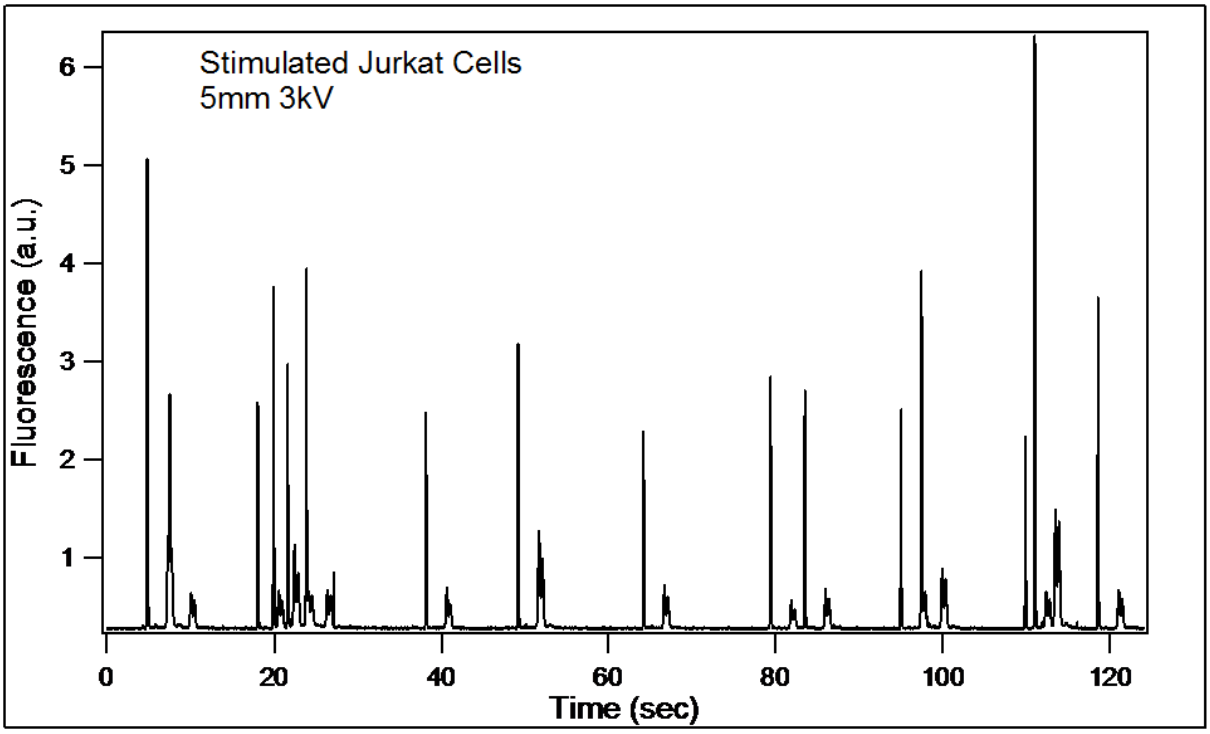

Figure 3.4. Typical electropherogram obtained from stimulated cells.

Portions of the electropherogram in Figure 3.4 were expanded to get more detail on the peak characteristics. Figure 3.5 shows the expanded portions for electropherograms from experiments with native (A) and stimulated (B) cells. Three distinct peaks are observed. The first tall peak is partially hydrolyzed 6-CFDA (6-CFp). The second peak is the completely hydrolyzed 6-CFDA (6-CF). The last peak is the benzotriole derivative of DAF-FM (DAF-FM T).

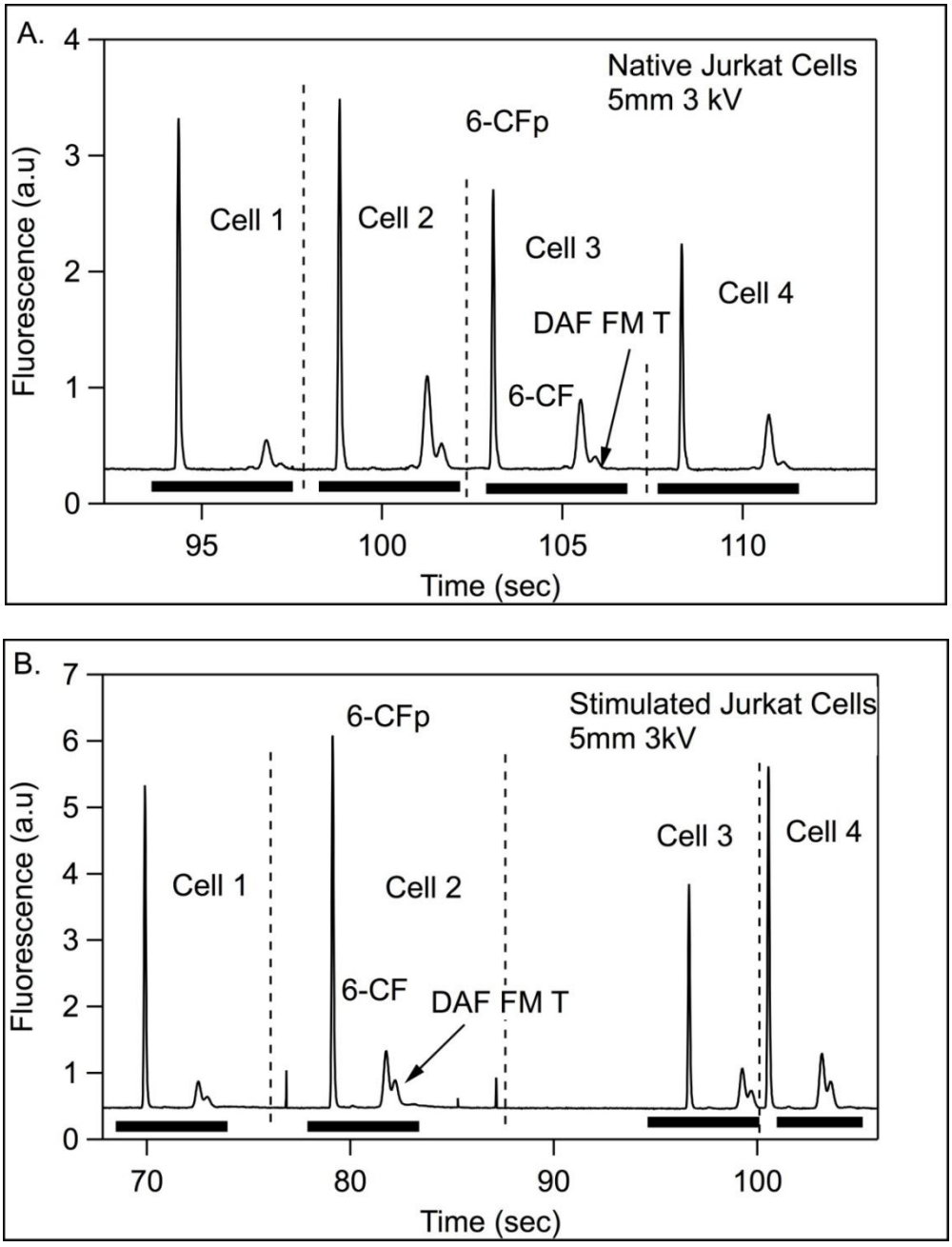

Figure 3.5 Electropherophoretic separation of dyes released from individual cells. These are 20 s and 30 s segments from a 120 s run. Each cell produced a peak envelop consisting of one tall peak due to partially hydrolyzed 6-CFDA (6-CFp) and a shorter doublet due to fully hydrolyzed 6-CFDA (6-CF) and DAF-FM T, that came ~3 s later.[69] There is a marked increase in DAF-FM T peak height relative to the 6-CF peak following stimulation.

The peak identities were verified by labeling a separate batch of cells with individual dyes. Lysate from individual cells generated two peaks (Figure 3.6), the taller one due to partially hydrolyzed 6-CFDA and the shorter due to 100% hydrolysis of 6-CFDA.[69]

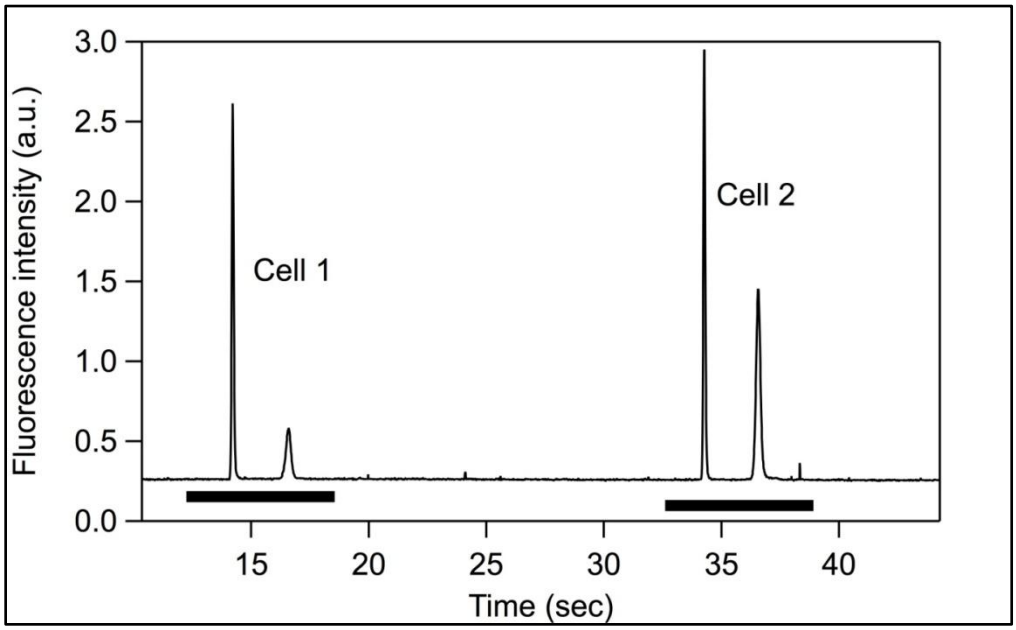

Figure 3.6. Electropherogram of cells labeled with 6-CFDA only.

The device was then used for the analysis of populations of control and stimulated cells. Due to the lack of a "cell standard", it was not possible to directly quantitate the amount of NO produced in these experiments. However, the ratio of DAF-FM to the products of the 6-CF hydrolysis could be used to evaluate the relative change in NO production in basal versus stimulated cells.

Table **3.1** shows the DAF-FM T, 6-CF and 6-CFp peak height and peak area ratios. As can be seen by this table, the ratio of the two products of 6-CF does not change upon stimulation but the ratio of DAF-FM T to either of these "internal standards" doubles (

Table **3.1**).

Table 3.1 Average peak ratios. The upper table contains the average peak area ratios while the lower table contains the average peak height ratios.

Peak Area Ratio	**6-CF/6-CFp**	**DAF-FM T/6-CF**	**DAF-FM T/6-CFp**	**Number of cells**
Native Cells	0.46(±0.26)	0.39(±0.34)	0.16(±0.12)	100
Stimulated Cells	0.48(±0.15)	0.72(±0.21)	0.34(±0.12)	100
Mean stimulated/mean native ratio	1.0(±0.30)	1.8(±0.40)	2.1(±0.17)	
Peak Height Ratio	**6-CF/6-CFp**	**DAF-FM T/6-CF**	**DAF-FM T/6-CFp**	**Number of cells**
Native Cells	0.21±0.31	0.26±0.08	0.054±0.073	100
Stimulated Cells	0.17±0.05	0.61±0.13	0.10±0.03	100
Mean stimulated/mean native ratio	0.8(±0.31)	2.3(±0.15)	1.9(±0.079)	

The cells were then stimulated by LPS. After 1 h incubation with LPS at a concentration of 1.5 µL/mL of cell suspension, no measurable increase in NO was observed. However after 3 h, measurable levels were seen as shown in Figure 3.5B. The addition of LPS resulted in an increase in NO production as shown by the relative increase in the DAF-FM T peak compared to the CF and CFp peaks. To better quantitate this change in NO production, the ratio of the DAF-FM T/6-CFp and DAF-FM T/6-CF peak heights and areas were calculated for 100 native and 100 stimulated cells, respectively. The distribution of the DAF-FM T/6-CF ratios is shown in Figure 3.7.

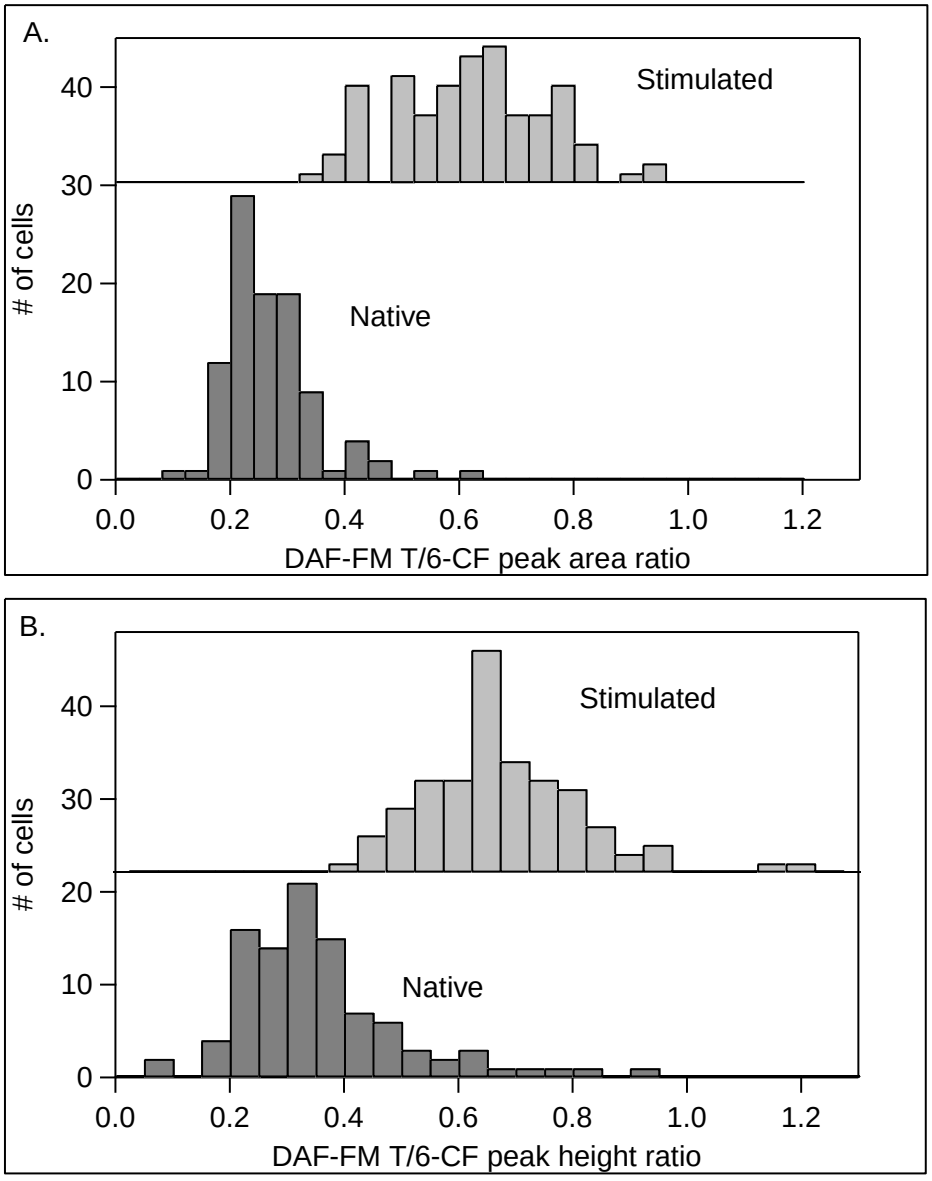

Figure 3.7 A is a histogram of DAF-FM T/6-CF peak area ratios calculated for 100 native cells (dark grey) and stimulated cells (light grey). B is a histogram of peak height ratios of the same cells. The peak ratios of cells increase due to increased NO expression following stimulation of Jurkat cells with LPS for 3 hours. Also included in B is data from analysis of bulk cell lysate.

Using equation 3.5 below, the relative increase in NO production for the stimulated cells was calculated.

$$\left(\frac{\left[\frac{DAF-FM\ T}{66-CFDA}\right]_{stimulated}-\left[\frac{DAF-FM\ T}{6-CFDA}\right]_{native}}{\left[\frac{DAF-FM\ T}{6-CFDA}\right]_{native}}\right)\times 100\% \qquad \textbf{(3.5)}$$

Both the peak height and peak area ratios indicate a 2-fold increase in NO concentration following 3 h stimulation of cells with LPS. (

Table **3.1**). Histograms of the ratios calculated from the various peaks are shown in Figure 3.8. A and B show the distribution of 6-CF/ 6-CFp peak height and area ratios respectively. Since the CFDA dye is not influenced by changes in concentration of NO, the distribution remains largely the same despite the cells increased NO expression. C and D are distributions of and DAF-FM T/ 6-CFp peak height and area ratios respectively . This ratio increased following increased NO expression by the LPS stimulated cells. A similar increase is observed in the distribution of DAF-FM T/ 6-CF, shown in E and F.

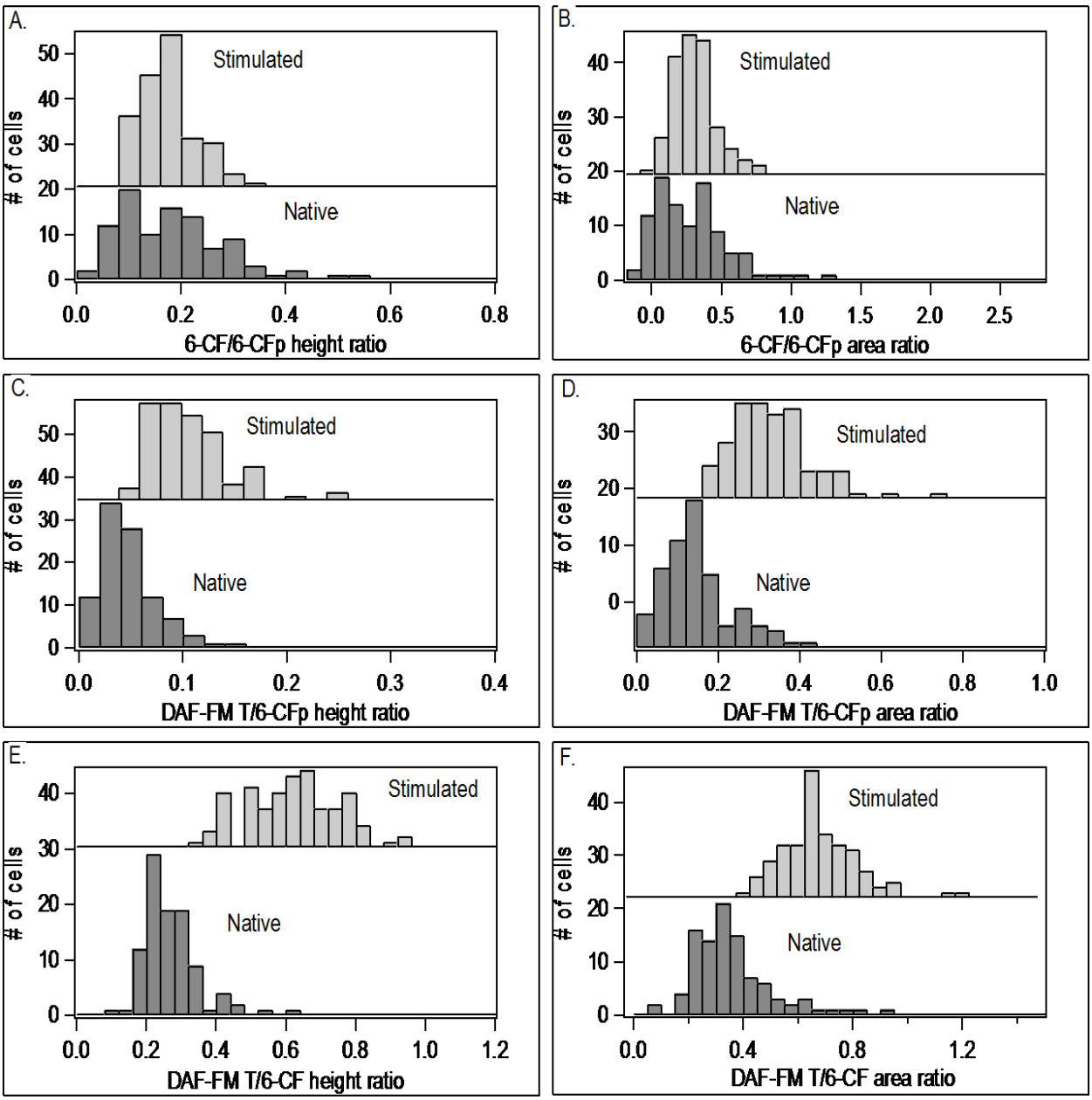

Figure 3.8. Comparison of peak heights and areas obtained from experiments with native cells (dark grey) and LPS-stimulated cells (light grey).

It is important to note that cells produce NO under stress and so we were careful to perform experiments with cells that were in the same log normal growth phase. It is for this reason that all the experiments were performed on the second day after cell passage.

3.3.6 Bulk vs. Single Cell Analysis

In addition to the single cell analysis reported above we recently published a report on the NO levels in native and stimulated Jurkat cells using microchip electrophoresis with LIF detection.[74] The measurement of the relative increase in the NO production for the bulk cells was carried out in a manner as close as possible to the procedure used in this paper. The bulk cell results were in good agreement with the results shown in figure 4. The DAF-FM T/6-CF peak height ratios are 2.2 times greater for the stimulated cells compared to the native cells. The average single cell results are in remarkably close agreement (2 fold increase) to the bulk cell analysis results.

3.4 Conclusion

We have demonstrated the transport and lysis of cells at a high throughput on an integrated glass/PDMS hybrid microfluidic device. LIF detection of NO was achieved in both bulk and single Jurkat cells labeled with 6-CFDA (an internal standard) and DAF-FM (a NO specific fluorophore). The resulting electropherograms were used to study the increase in NO production following stimulation with LPS. 3 h LPS-stimulation resulted in a two fold increase in NO production in both bulk and single cell analysis. A comparison of bulk and single cell NO measurements were performed and the average NO production in single cells compared well to the increase measured at the bulk cell level. In future studies, we will incorporate electrodes in the bulk and single cell analysis chips for electrochemical detection of NO and peroxynitrite.

Chapter 4 - Rapid and Efficient Micromixing via Actuation of Dielectric Elastomer Actuators

4.1 Introduction

Microfluidics is a field that is rapidly advancing and new applications in a variety of research fields including forensics,[106] DNA and protein analysis,[107,108]and molecular spectroscopy are constantly being reported.[109] In most of the major applications of microfluidic devices, rapid and efficient mixing is fundamental in facilitating the interaction of reactants to form products of interest. This is not trivial in microfluidic channel manifolds where fluid flow is characterized by low Reynolds's numbers (ratio of inertial and frictional forces) and fluid flow is laminar. As a consequence, mixing occurs by diffusion only, and long channels are required to attain sufficient mixing. Over the years, various interventions have been developed to improve mixing in microfluidic devices and they fall into two main categories; active and passive mixing techniques.

In the passive techniques, the channels are intricately designed to cause the laminar fluid streams to stretch and fold resulting in more chaotic flow patterns. This increases the contact surface area and reduces the diffusion path length of the fluid streams thereby increasing the mixing efficiency. Classic examples of passive mixers include split and recombine mixers,[110-113] staggered herringbone mixers.[114-116] and serpentine mixers.[117-119] Other types of passive mixers are designed to have grooves[120,121]and obstacles in their mixing channels,[122-124] that further stretch the fluid streams thereby increasing contact surface area. In this type of devices, external energy is not applied and mixing is improved exclusively by manipulating the flow pattern of the fluid streams. This minimizes the requirement for extra instruments and simplifies the operation of the microfluidic device. However, the designs of a majority of passive mixing devices are

complex and this makes the fabrication and assembly of these mixers difficult and time consuming.

On the other hand, active mixers are dependent on the application of an external source of energy to initiate mixing. Utilization of piezoelectric transducers,[125,126] electrokinetic manipulation,[127,128] and magnetic field,[129,130] have been used to induce chaotic fluid motion that causes rapid mixing of flow streams. Active mixers are often very simply designed and easily operated. These devices, however generally require bulky instrumentation with high energy demand.

In many of these microfluidic mixing devices, poly(dimethylsiloxane), PDMS, has become a popular substitute to glass due to its desirable properties that include flexibility, transparency and ease of fabrication.[131] Indeed, more investigations with complex and intricately designed PDMS-based microchips have been performed with ease. There is one property of PDMS, however, that has not been fully exploited in the area of microfluidics and that is PDMS's ability to act as a dielectric elastomer (DE). DEs are examples of electroactive polymers (EAPs) which are characterized by shape deformation when placed in an electric field. Actuation of an EAP is achieved by sandwiching a thin layer of the EAP between two electrodes provided that at least one of the electrodes is compliant. In the presence of an electric field, like charges accumulate on the opposite surfaces of the polymer. The attractive force generated by the opposite charge compresses the polymer. At the same, the repulsive force due to like charges stretches the polymer in its lateral plane. These attractive and repulsive forces constitute Maxwell stress which is defined by the equation below;[132]

$$p = k\varepsilon_o E^2 = k\varepsilon_o \left(\frac{V}{z_o}\right)^2 \qquad \textbf{(4.1)}$$

where k is the dielectric constant of the EAP, ε_o is the permittivity of free space, V is the potential applied across the EAP and z_o is the unstrained thickness of the EAP layer. Silicones, which are dielectric elastomers undergo a more non-linear stress often described by the Mooney-Rivlin model described as follows;[133]

$$W = \sum \left[c_1 \alpha_i^2 + \frac{C_2}{\alpha_i^2} \right] \qquad \textbf{(4.2)}$$

where W is the strain-energy density function, C_1 and C_2 are constants, and α_i is the stretch ratio in the x-, y-, or z-direction, which is the ratio of the strained EAP length to the unstrained EAP length. The equations (4.1) and (4.2) above demonstrate that as the electric field increases, the amount of strain on the polymer also increases.

In the experiments reported below, the run buffer in the fluidic channels of the microfluidic device served as the compliant electrode. Photolithography was used to pattern the other electrodes on a chrome-coated glass substrate. A thin layer of PDMS spun on this substrate acted as the EAP. In our group, we have utilized a similar design in a μTAS to perform non-biased sample injections for electrophoretic separations on a microfluidic device.[134,135] Below, we demonstrate that the EAP property of PDMS can be used to improve mixing in microfluidic device. Initial experiments in our lab investigated the influence of the compliant electrode size on mixing efficiency. The experiment involved varying the size of the patterned electrode on the glass substrate. This would in turn vary the length of the fluidic channel layer above the electrode. We initially thought that the larger the channel under the patterned electrode was, the larger the PDMS actuation and therefore the greater the folding of the fluid streams.[136] There was no marked improvement in mixing with the initial designs. A possible explanation for these observations was given by finite element analysis simulations by Soulimane, *et al*[137] that predicted the electromechanical behavior of EAP during actuation. Their findings showed that

the greatest deformation occurred on the corners and edges in that order, and the least deformation was experienced at the center of the EAP (Figure 4.1).

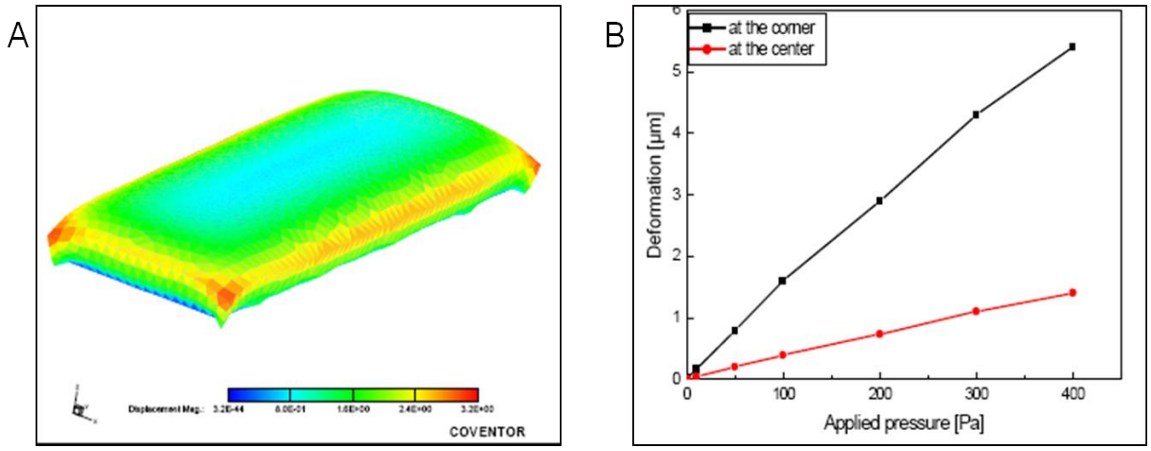

Figure 4.1. A: Finite element analysis structure obtained by ConvectorWare software from applying 200 Pa to a 10 μm thick PDMS using virtual electrodes. B: Comparison of degree of deformation at the corners and center of PDMS when electrostatic pressure is virtually applied.[137]

For this reason, we designed the channels above the patterned chrome electrodes to have the maximum possible corners and edges (Figure 4.2C). This would in turn cause maximum deformation of the channel during EAP actuation.

4.2 Experimental

4.2.1 Chemicals

Sodium dodecyl sulfate (SDS) was purchased from Sigma Chemical Co. (St. Louis, MO). Sodium borate was obtained from Fisher Scientific (Pittsburg, PA). 2'7'-dichlorofluorescein was obtained from Acros Organics (Morris Plains, NJ). PDMS (Sylgard 184 elastomer kit) was obtained from Dow Corning (Midland, MI). SU-8 2010 photoresist was purchased from Microchem Corp. (Newton, MA). The SU-8 developer, 2-(1-methoxy) propyl acetate was obtained from Acros (Morris Plains, NJ). All chemicals were used as received. Silicon wafers, 4 inches in diameter, were purchased from Silicon Inc. (Boise, ID). All solutions were prepared

using distilled, deionized water purified using an E-pure system (Barnstead, Dibuque, IA).Solutions were filtered immediately before introduction to the reservoirs using syringe-driven o.45 μm PVDF filters (Fisher Scientific).

4.2.2 Microchip Fabrication

The device consisted of three distinct parts; the fluidic layer, the actuation layer and the patterned electrode substrate. The mask designs required for the fluidic layer and patterned electrode substrate were created in AutoCAD2006LT (Thompson Learning, Albany NY) and photo plotted at 40,000 dpi (dots per inch) by Fineline Imaging (Colorado Springs, CO) on a photomask.

4.2.3 Electrode Fabrication

The electrode substrates were fabricated from 4 × 4 × 0.4 in. white crown glass coated with chrome (120 nm) and AZ1500 positive photoresist (530 nm), supplied by Telic Co. (Valencia, CA). The procedure used was based on a previously published method.[27] Briefly, the photomask bearing the electrode design was placed on the coated glass and exposed to UV radiation from a UV flood exposure system (Newport Oriel, Stratford, CT). Unpolymerized photoresist was then developed in a potassium hydroxide bath. The exposed chrome was then etched away in a ceric sulfate solution. After a thorough rinse with ultrapure water, the residual photoresist was removed by rinsing with ethanol, acetone and ethanol, in that order (Figure 4.2A).

4.2.4 Device Fabrication

Established soft lithography techniques utilizing SU-8 negative photoresist were used to prepare the fluidic layer mold.[26] The height of the features on the mold was measured with a XP-2 profilometer (Ambios Technology, Santa Cruz, CA). 20:1 PDMS elastomer base to curing

agent (Sylgard 184) was spun at 2000 rpm for 45 s onto the glass slide with the patterned electrodes, to produce an electroactive polymer (EAP) layer that was ~40 µm thick (Figure 4.2B). The now PDMS-coated patterned electrode glass substrate was cured for 6 min at 80^{o}C. A 10:1 PDMS mixture was poured onto the fluidic layer mold and partly cured for 14 min at 80^{o}C. Next, the PDMS was peeled off the mold and layered over the coated patterned electrode surface so that the cross-shaped regions on the sample channels were directly above the electrodes as shown in Figure 4.2C. The assembled device was then cured at 80^{o}C for 50 min after which excess PDMS was trimmed off and reservoirs punched to access the channels in the fluidic layer. Epoxy was used to fix wires to provide electrical contact between the patterned chrome electrode and the high voltage supply.

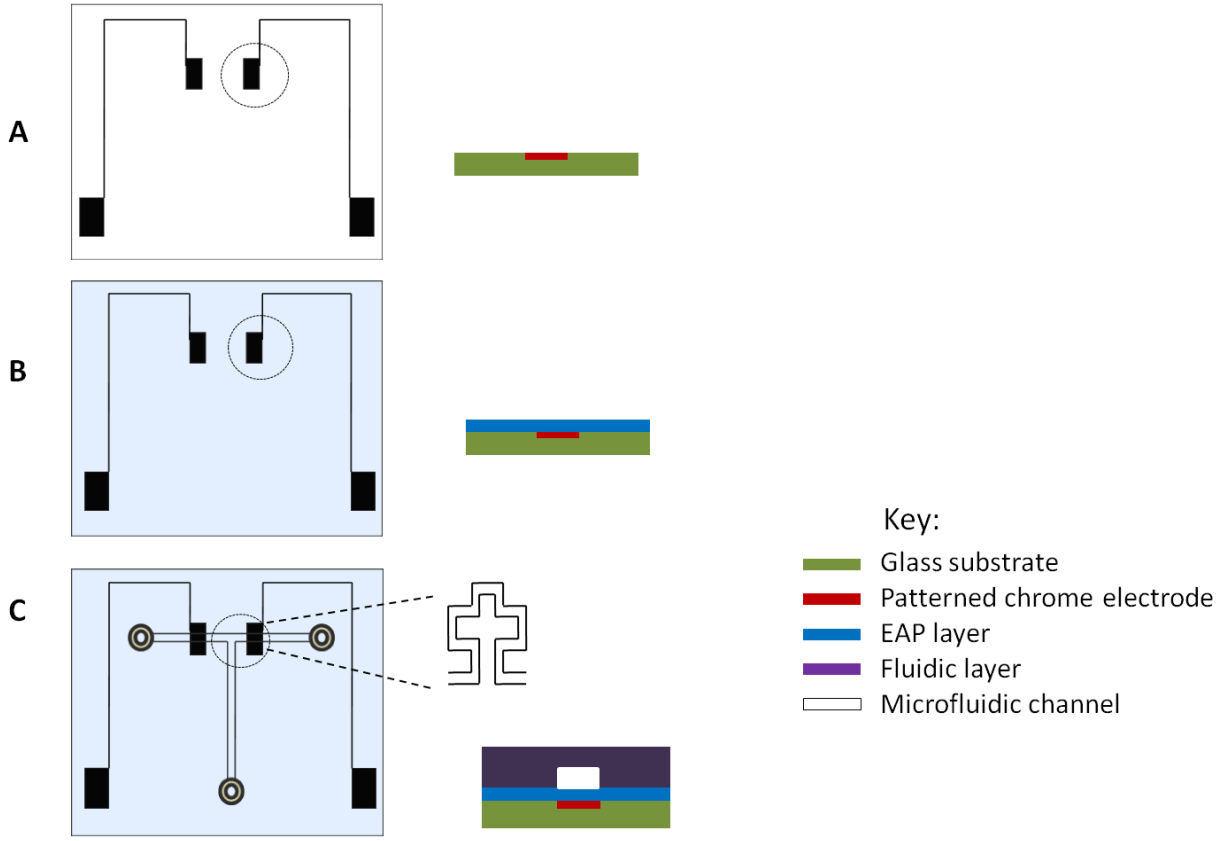

Figure 4.2. Fabrication of microfluidic mixing device. A illustrated the electrode design prepared by photolithography. In B, a thin layer of PDMS is spin-coated onto the electrode substrate. C shows the

assembly of fluidic layer onto EAP-coated glass substrate. The cross sections of the region in the dotted circles are shown on the corresponding right side of the drawings.

4.2.5 Microscopy

The microfluidic device was placed on the stage of a TE2000-U inverted microscope. A Bertan high voltage (0-10 kV) power supply (Hicksville, NY) controlled by an in-house Labview software program (National Instruments, Austin, TX), was used to apply voltage to the reservoirs. 450-490 nm light was then shone onto the microfluidic device through a 10× objective (Nikon) and subsequent emission collected by the same objective and captured by a high resolution Sony camera or Roxio Videowave creation software. Images were analyzed using ImageJ (NIH).

4.2.6 Experimental Details

The chip was filled with the run buffer comprising of 5mM sodium borate and 1.5mM SDS at pH 9.15 by applying negative pressure on one of the reservoirs. To visualize the mixing, the reservoir on the left arm of the T-mixer was replaced with buffer containing 2'7'-dichlorofluorescein. An in-house program written in LabView (National Instruments, Austin, TX) was used to apply voltages to the reservoirs and patterned electrodes (PE). Based on Kirchhoff's laws, voltage was applied on the reservoirs on the arms of the T-mixer while the reservoir at the end of the mixing channel was grounded. Voltage was also applied to the PE via the wire connections on the device so that there was a potential difference across the EAP i.e, voltage in the channel above PE was not equal to voltage on PE ($V_{channel} \neq V_{PE}$). As a consequence, the EAP above the electrode was actuated resulting in increased volume of the channel above the PE. When the potential difference was dropped back to 0 ($Vchannel = V_{PE}$), the EAP relaxed back to its original shape and the channel returned to its original volume, and in the process, the extra buffer was ejected toward the mixing channel due to electroosmotic flow

(Figure 4.2A). When the actuators on either side of the T mixer were actuated and relaxed at 180^{o} out of phase, buffer was ejected into the mixing channel alternately, creating a wavy motion of the streams (Figure 4.2B). As a consequence, there was an increase in contact surface area and decreased diffusion distance of the fluid streams. Mixing efficiency was best improved when the EAP was actuated at 20Hz. To quantitate the mixing efficiency, the following expression was used:

$$Mixing\ Index = \frac{\sigma}{c_{ave}} = \sqrt{\frac{1}{N-1}\sum_{i=1}^{N}\left(\frac{c_i - c_{ave}}{c_{ave}}\right)^2} \qquad \textbf{(4.3)}$$

Where N is the total number of pixels along a line segment, σ is the standard deviation, c_{ave} is the average intensity over N pixels and c_i is the intensity of pixel i. When perfect mixing occurs, the mixing index is equal to zero since c_i=c_{ave}. Mixing is considered complete if mixing index ≤ 0.1.

4.3 Results and Discussion

The aim of the experiments performed was to induce efficient mixing of two fluid streams by increasing the surface contact area and reducing the diffusion distance of the fluid streams. Fluid transportation was achieved by applying a field strength of 500V/cm in the fluidic channels. This was accomplished by applying 2.2 kV on the reservoirs on the arms of the T-mixing device and grounding the reservoir at the end of the mixing channel. The Reynolds's number was determined to be 164. This low value indicates that the flow in the channels was laminar and therefore mixing occurs largely by diffusion. The laminar flow is verified by the distinct streams of fluorescently dyed buffer and dye-free buffer as shown in Figure 4.3B.

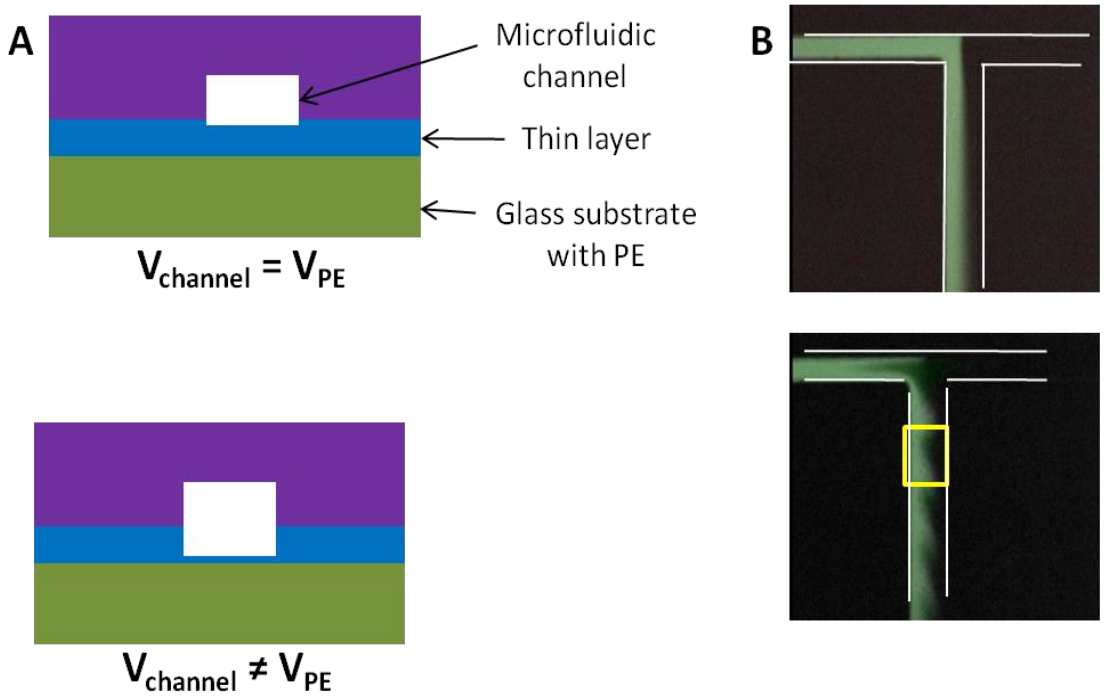

Figure 4.3. A is an illustration of EAP actuation. When the potential difference across the EAP is 0, no actuation occurs (top). In the presence of potential difference, the EAP is actuated, leading to increased channel volume (bottom). B shows images from grabbed frames of videos of the mixing device containing fluorescently dyed buffer on the left horizontal channels and dye-free buffer on the right channel The top image was obtained without EAP actuation while the bottom image was captured during actuation at 20Hz and 180^0 out of phase. The yellow box shows the region used to calculate mixing efficiency.

By applying voltage to the patterned electrodes such that there was a potential difference across the EAP, actuation occurred and this caused the volume of the channel directly above the patterned electrode to increase. Subsequently, when the potential difference dropped back to zero, the EAP relaxed back to its original shape and the channel volume reduced with the extra buffer being ejected towards the intersection. The EAP on either side of the T-mixer were actuated at 180^o out of phase and buffer was ejected alternately form the channels on the arms of the T-mixing device. The result was a wavy flow (Figure 4.3) that caused stretching and folding of the fluid streams which increased the contact surface area and reduced diffusion distances of the mixing species. To quantitatively analyze the mixing efficiency, images of the mixing

channel were acquired with and without EAP actuation, using a high resolution CCD camera (Roper Scientific, Inc., NJ). ImageJ (NIH) software was then used to obtain the pixel intensities in regions of the mixing channel containing a 360^{o} wave (region in yellow box Figure 4.3) a few mm below the T-intersection. To do this, the line profile of the pixel intensity was obtained. Figure 4.4 shows the line profiles at 2.5 mm below the T-intersection on the mixing channel before and during EAP actuation. Decreased pixel intensity was observed during actuation because the fluorescently dyed buffer diffused and mixed better with the non-labeled buffer. The region between the asterisks in the profile in Figure 4.4 was used to calculate the mixing index.

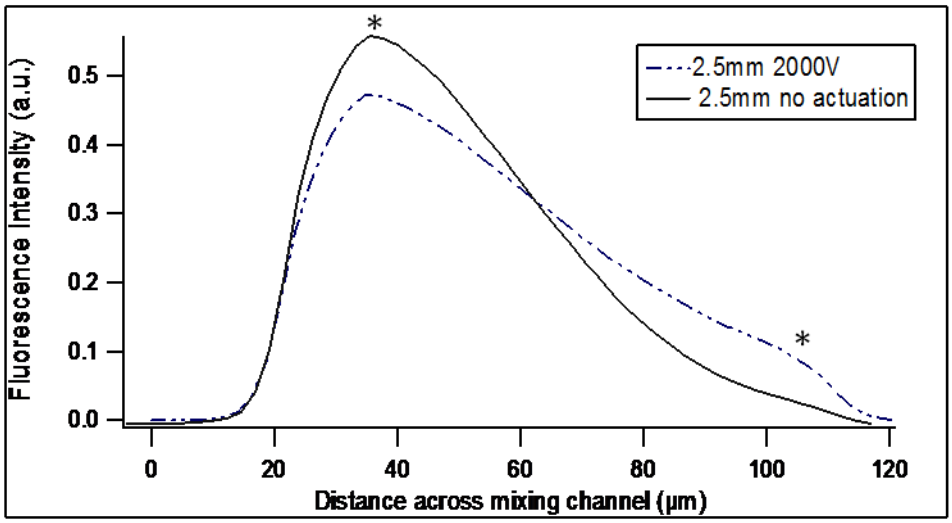

Figure 4.4. Fluorescence intensity profile of mixing channel at 2.5mm below the T-intersection with 20Hz actuation (blue) and without actuation (black). The potential difference across the EAP layer was 2000V.

A data analysis program, Igor, was used to calculate the average pixel intensity and standard deviation between the two asterisks in Figure 4.4. The mixing index was determined by the standard deviation/average pixel intensity ratio. We performed experiments at different actuation frequencies to determine what actuation frequency yielded the most efficient mixing. The results from at least 2 experiments each are summarized in Figure 4.5. The trend observed suggested that lower EAP actuation frequencies yielded better mixing. We chose to work with

20Hz instead of because the area selected for mixing analysis would be smaller (smaller sinusoidal wave). From this point, all results discussed were performed at 20Hz unless stated otherwise.

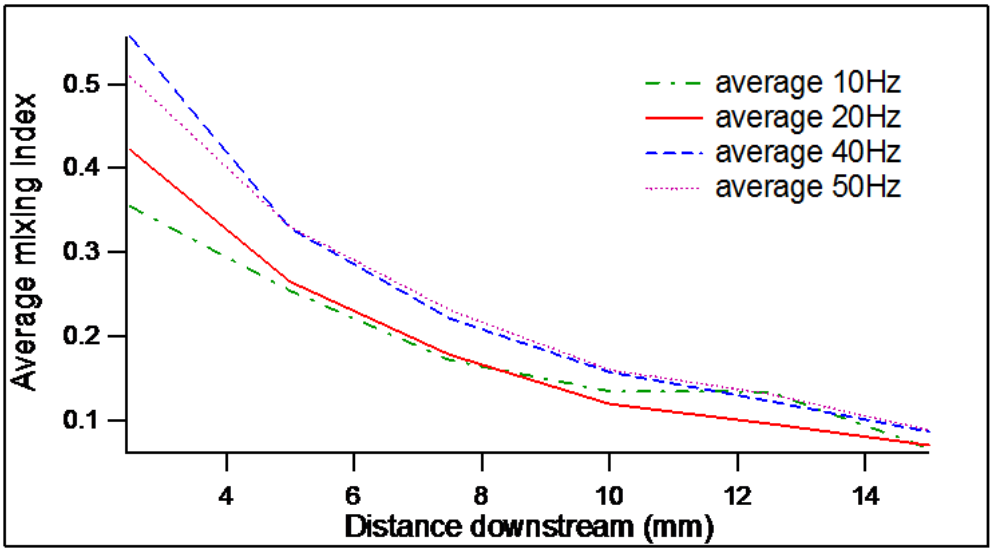

Figure 4.5. Mixing index measurements at different actuation frequency. For distances up to 7.5mm below the intersection, the mixing index improved with lower EAP actuation frequency.

At higher actuation frequencies, the mixing was poorer. We speculate that this was due to the reduced folding and stretching of the fluid streams caused by the insufficient injection of buffer into the mixing channel. When actuation is too fast, the EAP the volume change in the channel is very rapid and the excess buffer gets sucked back into the horizontal section before it gets a chance to be injected into the mixing channel.

The mixing index was determined at several distances downstream, with and without EAP actuation. The profiles below (Figure 4.6 and Figure 4.7) were obtained from 5.0, 7.5, 10.0 and 15mm below the intersection on the mixing channel. It was observed that at shorter distances below the T-intersection, the two streams from either side of the arms of the T-shaped mixing device were distinct. This is illustrated by the high fluorescence intensity on the left of the

profiles and very low intensities on the right (Figure 4.3 and Figure 4.4). Perturbation of the streams due to actuation of the EAP resulted in obvious fluid disturbance hence the less steep gradients in the actuation profiles. On the other hand, the fluid streams were not as distinct further down the mixing channel. The fluorescent dye molecule, fluorescein, has a high diffusion coefficient and the fluid streams had already mixed substantially by diffusion. The profiles at these distances had smaller gradients and EAP actuation minimally influenced the mixing index (Figure 4.7).

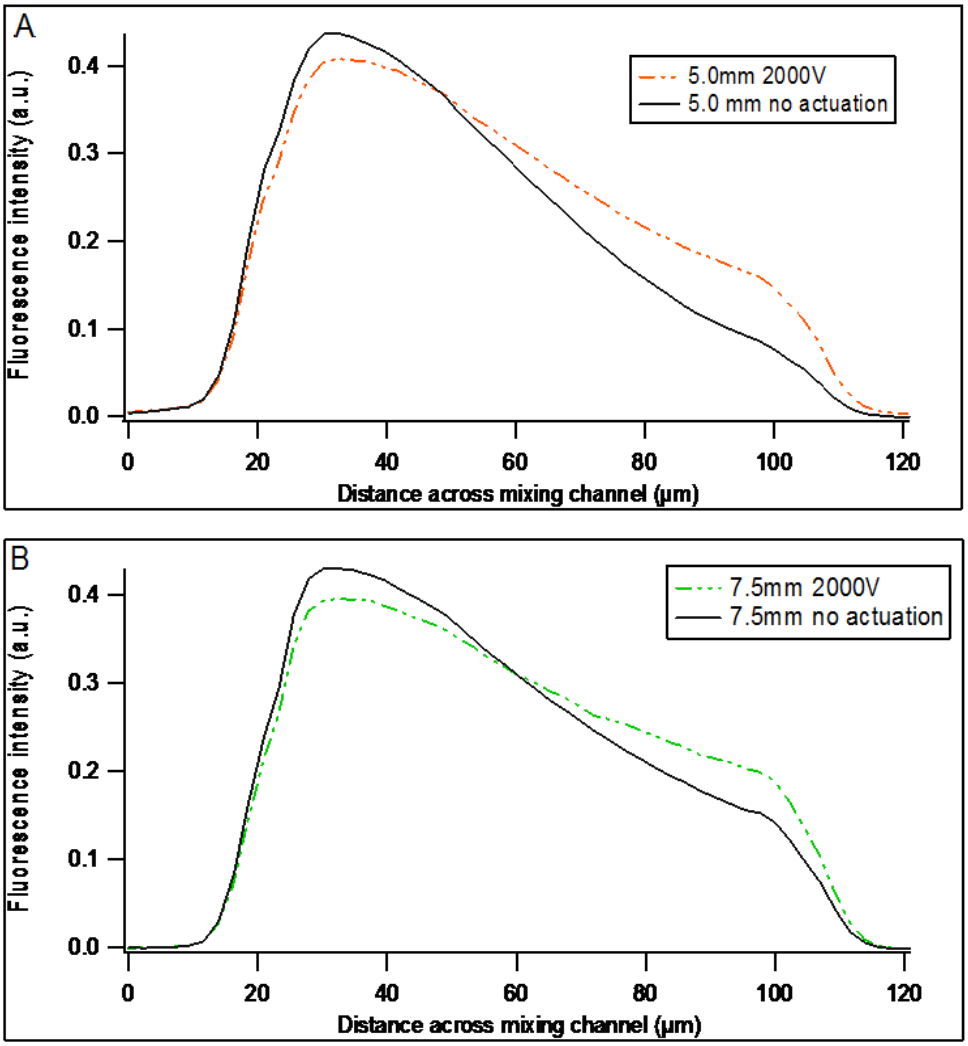

Figure 4.6. Profiles obtained from 20Hz EAP actuation at 5.0mm (A) and 7.5mm (B) below the intersection.

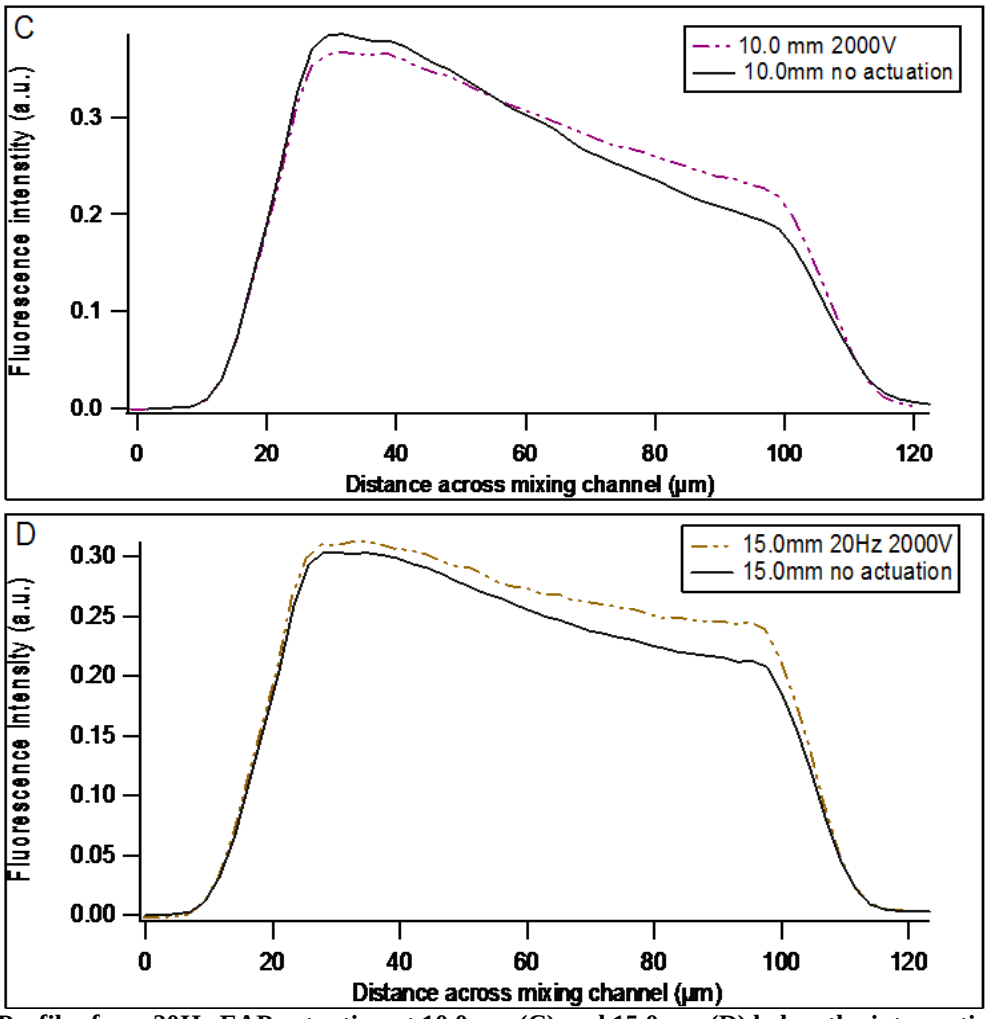

Figure 4.7. Profiles from 20Hz EAP actuation at 10.0mm (C) and 15.0mm (D) below the intersection.

To better determine the improvement in mixing, the experiment was performed in triplicate. Profiles were collected from the designated distances from the intersection on the mixing channel during EAP actuation and without actuation. The average mixing index was determined and plotted on a graph (Figure 4.8).

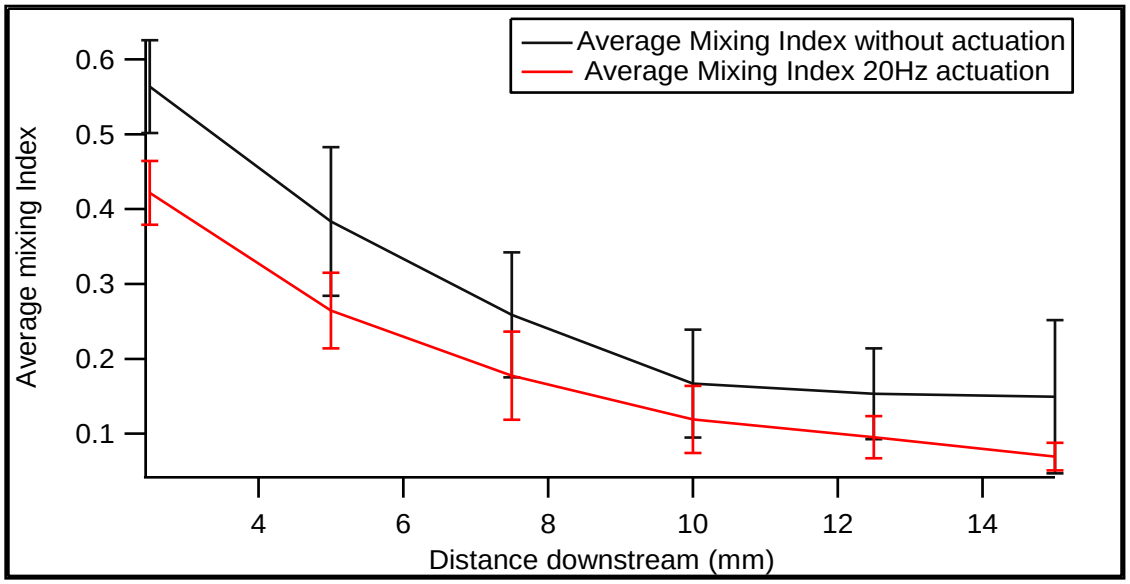

Figure 4.8. Plots of average mixing indices with (red) and without (black) EAP actuation. A general improvement in mixing is indicated by the reduced value of average mixing index.

As is observed in Error! Reference source not found., there was a general improvement in ixing i.e reduced mixing index values but this was not sufficient especially in the regions close to the intersection. We tried a bifurcated channel design (Figure 4.9) with the hope that the fluid streams would be split and recombine to create multiple streams and therefore reduce diffusion distance required for complete mixing to be accomplished. Unfortunately, the mixing index values were worse than those obtained with the original chip design.

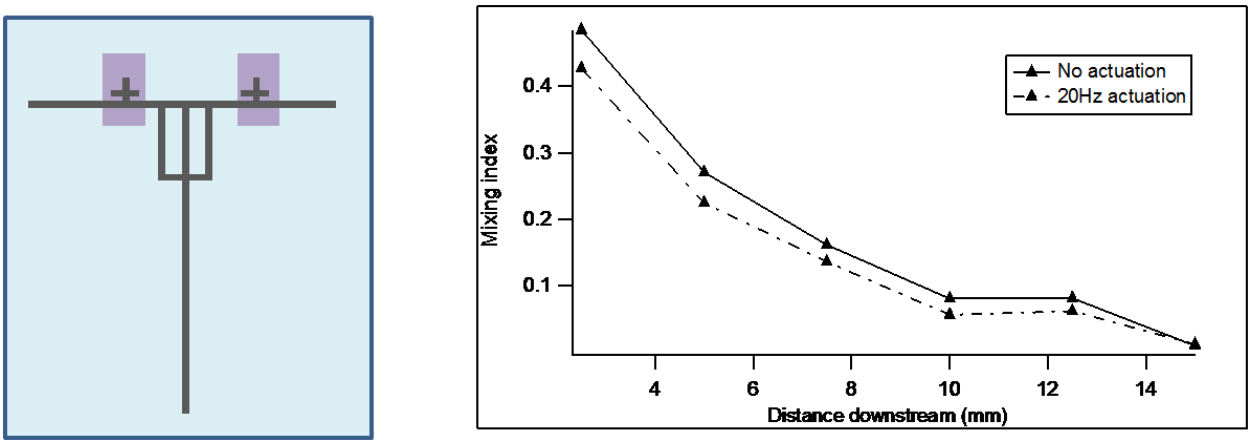

Figure 4.9. Right: Bifurcated design of fluidic layer. The solid gray lines represent the fluidic channels. The purple region over the 'cross' on the horizontal channels represents the patterned chrome electrodes. Left: Plot of calculated mixing indexes with actuation (broken line) and with actuation (solid line), at designated distances on the mixing (vertical) channel.

4.4 Conclusion

PDMS is now routinely used in the fabrication of microfluidic devices due to its favorable properties that include flexibility, transparency, ease of fabrication and low cost. However, its property as an electroactive polymer (EAP) has not been extensively exploited. EAPs change shape in the presence of an electric field and this can be accomplished by placing a thin layer of PDMS between two electrode surfaces, with at least one of the electrodes being flexible. We have employed this property to develop a microfluidic device that is capable of improving fluid mixing in microfluidic channels. The T-type microfluidic mixer consists of a thin layer of PDMS sandwiched between a glass substrate patterned with chrome electrodes and a PDMS layer containing the fluid channels. The patterned electrodes were positioned on the horizontal channels of the T-shaped mixer. The electrolyte buffer in the channels acted as the flexible electrode. When voltage was applied across the thin PDMS layer under the patterned electrode, its shape changed and as a result, the volume of the buffer in the channel increased.

By applying voltage to the patterned electrodes at 180° out of phase, fluids from the two arms of the T-type mixer were alternately injected into the mixing channel, creating a wavy flow of the fluid streams. The subsequent stretching and folding of the streams increased the contact surface area and decreased the diffusion distances of the components of the fluid streams. Admittedly, the improvement in mixing was not impressive and the use of a bifurcated design for the fluidic layer did not yield any better results.

I would like to thank Dr. Alexander Price and Kevin McDaniel for their valuable help with setting up the experiments.

Chapter 5 - Future Directions and Outlook

5.1 Separation and Identification of Serine Proteases

We have demonstrated in our experiments, the potential of immunoaffinity chromatography in analyzing small volume samples of hemolymph. The batch method of performing these experiments made it possible have all the eluted protein in one discrete volume and at a higher concentration. Another advantage of the batch method was that it was very simple to perform and required less preparation time. The online format has the potential for automation, which is the goal of this project. The advantage of using a column is that there will be minimum loss of sample since the injections and buffer changes would be seamless. Extra caution has to be taken to avoid loss of sample through non-specific binding on the plumbing system. An easy and fast way would be to add a surfactant to the buffer. Tween-20 is a popular option for such a task. A downside of Tween-20 is that it causes problems during the MS experiments. The liquid chromatography pre-concentration step utilizes a C18 reverse phase column and since Tween-20 is a non-ionic surfactant, it also gets retained alongside the analytes. Furthermore, its concentration is orders of magnitude more than that of the analytes and is therefore, its signal masks all the others from the target analytes.

More experiments need to be performed to further verify the identities of the proteases that interact with SRPN2. Since the protease form covalent complexes with the serpins, it is possible that trypsin digestion produces a peptide fragment containing peptides from both the serpin and protease. If this is the case, then it would be possible to ascertain the identity of the proteases these serpins bind to. If this can be accomplished, then these experiments can be used to routinely study serpins and identify the proteases they interact with.

An easier way of verifying that the identified proteases do indeed interact with SRPN2 would be to analyze the elution fractions of the immunoaffinity experiment with SDS-PAGE followed by Western immunoblotting using antibodies to the proteases rather than SRPN2 antibody. If the complex band at ~62 kDa is observed on Western blots with both antibodies, then, this would be proof of the protease-SRPN2 interaction.

Ion exchange chromatography can be utilized to further separate the SRPN2-protease complex from the free SRPN2. The masses of the two are quite close and size-exclusion chromatography might not separate them sufficiently. This added step might however lead to further loss of precious sample.

5.2 Single Cell Analysis of NO on Microfluidic Devices

Our improved device has shown great promise in the analysis of single cells. The biggest challenge with these experiments was the control of flow. It takes a significant amount of time for the flow in the channels to equilibrate after the flow rate on the syringe pump is changed. Experiments are on-going in our lab to design an on-chip pumping system that utilizes micro-peristaltic pumps that are controlled by LabView software. We predict that the flow will be easier to control and take significantly less time to equilibrate.

The experiments we performed are comparative studies and we could not determine quantitatively the concentration of NO in each cell. Our collaborators in University of Kansas determined the concentration of NO in bulk cell lysate. It is possible to incorporate electrodes further down the separation channel so that electroanalytical techniques like amperometry can be used to quantitate NO from single cells, if the detection limit of these techniques permits it.

These experiments worked quite well with non-adherent cells (Jurkat cells). We did a few experiments with adherent cells but had frequent blockages due to sticky cell debris. The

attractive feature with PDMS-based chips however is their cost and ease of fabrication. When a device got clogged, pulling it apart and washing the fluidic channels with a surfactant got rid of the clog and after re-assembly; the device could be used for more experiments.

These devices lay a good foundation for the development of easy-to-use gadgets that can be applied in early detection biomarkers for diseases that are difficult and expensive to manage when at advanced stages.

Chapter 6 - REFERENCE

(1) Miller, J. M. *CHROMATOGRAPHY Concepts and Contrasts*; Second ed.; John Wiley and Sons: Hoboken, New Jersey, 2005.

(2) Jacobson, S. C.; Culbertson, C. T.; CRC Press LLC: 2006, p 19.

(3) Giddings, J. C. *Unified Separation Science*; Wiley, 1991.

(4) Tiselius, A. *Transactions of the Faraday Society* **1937**, *33*, 524.

(5) Brishammar, S.; HjertÃ©n, S.; Hofsten, B. v. *Biochimica et Biophysica Acta* **1961**, *53*, 518.

(6) Raymond, S.; Weintraub, L. *Science* **1959**, *130*, 711.

(7) Ornstein, L. *Annals of the New York Academy of Sciences* **1964**, *121*, 321.

(8) Davis, B. J. *Annals of the New York Academy of Sciences* **1964**, *121*, 404.

(9) Laemmli, U. K. *Nature* **1970**, *227*, 680.

(10) Jorgenson, J. W.; Lukacs, K. D. *Analytical Chemistry* **1981**, *53*, 1298.

(11) Jorgenson, J. W.; Lukacs, K. D. *Clinical Chemistry* **1981**, *27*, 1551-3.

(12) Jorgenson, J. W.; Lukacs, K. D. *Journal of Chromatography A* **1981**, *218*, 209.

(13) Jacobson, S. C.; Culbertson, C. T.; Daler, J. E.; Ramsey, J. M. *Analytical Chemistry* **1998**, *70*, 3476.

(14) Griffiths, S. K.; Nilson, R. H. *Analytical Chemistry* **2000**, *73*, 272.

(15) Kenndler, E. *Chem. Anal. (N. Y.)* **1998**, *146*, 25.

(16) Sterward, M. W. *Antibodies: their structure and function*; 1 ed.; Chapman and Hall: London and New York, 1984.

(17) Norberto, A. G.; Timothy, B.; Terry, M. P. *ELECTROPHORESIS* **2008**, *29*, 3259-3278.

(18) Anderson, N. L.; Anderson, N. G. *ELECTROPHORESIS* **1998**, *19*, 1853.

(19) Skoog, A. D. H., F. J.; Nieman, T. J. *Principles of Instrumental Analysis*; 5 ed.; Brooks/Cole, 1998.

(20) Walther, T. C.; Mann, M. *The Journal of Cell Biology* **2010**, *190*, 491-500.

(21) Yin, H.; Marshall, D. *Current Opinion in Biotechnology* **2012**, *23*, 110.

(22) Oita, I.; Halewyck, H.; Thys, B.; Rombaut, B.; Vander, H. Y.; Mangelings, D. *Anal. Bioanal. Chem.* **2010**, *398*, 239.

(23) Ahmadi, M.; Yeow, J. T. W.; Shahini, M.; CRC Press: 2012; Vol. 2, p 269.

(24) Capretto, L.; Cheng, W.; Hill, M.; Zhang, X. *Top. Curr. Chem.* **2011**, *304*, 27.

(25) Whitesides, G. M. *Nature* **2006**, *442*, 368.

(26) Duffy, D. C.; McDonald, J. C.; Schueller, O. J. A.; Whitesides, G. M. *Analytical Chemistry* **1998**, *70*, 4974.

(27) Price, A. K.; Anderson, K. M.; Culbertson, C. T. *Lab on a Chip* **2009**, *9*, 2076.

(28) Abraham, E. G.; Jacobs-Lorena, M. *Molecular and population biology of mosquitoes* **2004**, *34*, 667.

(29) Osta, M. A. *The Journal of experimental biology* **2004**, *207*, 2551.

(30) Read, A. F.; Lynch, P. A.; Thomas, M. B. *PLoS Biol* **2009**, *7*, e1000058.

(31) Christensen, B. M.; Li, J.; Chen, C.-C.; Nappi, A. J. *Trends in Parasitology* **2005**, *21*, 192.

(32) An, C.; Budd, A.; Kanost, M.; Michel, K. *Cellular and Molecular Life Sciences* **2011**, *68*, 1929-1939.

(33) Michel, K.; Budd, A.; Pinto, S.; Gibson, T. J.; Kafatos, F. C. *EMBO Rep* **2005**, *6*, 891.

(34) Michel, K.; Suwanchaichinda, C.; Morlais, I.; Lambrechts, L.; Cohuet, A.; Awono-Ambene, P. H.; Simard, F.; Fontenille, D.; Kanost, M. R.; Kafatos, F. C. *Proceedings of the National Academy of Sciences* **2006**, *103*, 16858-16863.

(35) Paskewitz, S. M. L. S. *Insect Biochemistry and Molecular Biology* **2005**, *35*, 815-824.

(36) Beckage, N. E.; Academic Press: Amsterdam; Boston;Heidelberg;London;New York;Oxford;Paris;San diego;Singapore;Sydney;Tokyo, 2008.

(37) Osta, M. A.; Christophides, G. K.; Vlachou, D.; Kafatos, F. C. *J Exp Biol* **2004**, *207*, 2551.

(38) Cerenius, L.; Söderhäll, K. *Immunological Reviews* **2004**, *198*, 116.

(39) Suwanchaichinda, C.; Kanost, M. R. *Gene* **2009**, *442*, 47.

(40) An, C.; Lovell, S.; Kanost, M. R.; Battaile, K. P.; Michel, K. *Proteins: Structure, Function, and Bioinformatics* **2011**, *79*, 1999.

(41) Tong, Y.; Jiang, H.; Kanost, M. R. *Journal of Biological Chemistry* **2005**, *280*, 14932-14942.

(42) Wang, Y.; Jiang, H. *Insect Biochemistry and Molecular Biology* **2004**, *34*, 387.

(43) Silverman, G. A.; Bird, P. I.; Carrell, R. W.; Church, F. C.; Coughlin, P. B.; Gettins, P. G. W.; Irving, J. A.; Lomas, D. A.; Luke, C. J.; Moyer, R. W.; Pemberton, P. A.; Remold-O'Donnell, E.; Salvesen, G. S.; Travis, J.; Whisstock, J. C. *Journal of Biological Chemistry* **2001**, *276*, 33293-33296.

(44) Huntington, J. A.; Read, R. J.; Carrell, R. W. *Nature* **2000**, *407*, 923.

(45) Ragan, E. J.; An, C.; Yang, C. T.; Kanost, M. R. *Journal of Biological Chemistry* **2010**, *285*, 29642-29650.

(46) Ishihama, Y.; Oda, Y.; Tabata, T.; Sato, T.; Nagasu, T.; Rappsilber, J.; Mann, M. *Molecular & Cellular Proteomics* **2005**, *4*, 1265-1272.

(47) Hunter, M. J.; Ludwig, M. L. *Journal of the American Chemical Society* **1962**, *84*, 3491.

(48) Volz, J.; Osta, M. A.; Kafatos, F. C.; MÃ¼ller, H.-M. *Journal of Biological Chemistry* **2005**, *280*, 40161-40168.

(49) Paskewitz, S. M.; Andreev, O.; Shi, L. *Insect Biochem. Mol. Biol.* **2006**, *36*, 701.

(50) Volz, J.; Müller, H.-M.; Zdanowicz, A.; Kafatos, F. C.; Osta, M. A. *Cellular Microbiology* **2006**, *8*, 1392.

(51) Gorman, M. J.; Andreeva, O. V.; Paskewitz, S. M. *Insect Biochemistry and Molecular Biology* **2000**, *30*, 35.

(52) Tymvios, C.; Moore, C.; Jones, S.; Solomon, A.; Sanz-Rosa, D.; Emerson, M. *British Journal of Pharmacology* **2009**, *158*, 1735.

(53) Tiscornia, A.; Cairoli, E.; Marquez, M.; Denicola, A.; Pritsch, O.; Cayota, A. *Journal of Immunological Methods* **2009**, *342*, 49.

(54) Yasuda, H. *Nitric Oxide-Biology And Chemistry* **2008**, *19*, 205-216.

(55) Muller, G.; Morawietz, H. *Antioxidants & Redox Signaling* **2009**, *11*, 1711-1731.

(56) Avci, A.; Tüzüner-Öncül, A. M.; Gökcan, M. K.; Namuslu, M.; Öztürk, A.; Durak, İ. *Journal of Oral Pathology & Medicine* **2009**, *38*, 304.

(57) Punathil, T.; Tollefsbol, T. O.; Katiyar, S. K. *Biochemical and Biophysical Research Communications* **2008**, *375*, 162.

(58) Assumpção, C. R. L.; Brunini, T. M. C.; Pereira, N. R.; Godoy-Matos, A. F.; Siqueira, M. A. S.; Mann, G. E.; Mendes-Ribeiro, A. C. *Blood Cells, Molecules, and Diseases* **2010**, *45*, 338.

(59) Lee, C.-H.; Wei, Y.-W.; Huang, Y.-T.; Lin, Y.-T.; Lee, Y.-C.; Lee, K.-H.; Lu, P.-J. *Journal of Cellular Biochemistry* **2010**, *110*, 112.

(60) Chung, K. K. K. *Neurosignals* **2006**, *15*, 307.

(61) Ram Kumar, K.; Madhu, D. *Annals of Neurosciences* **2005**, *12*.

(62) Contestabile, A.; Monti, B.; Contestabile, A.; Ciani, E. *Current Medicinal Chemistry* **2003**, *10*, 2147.

(63) Sorrenti, V.; Di Giacomo, C.; Salerno, L.; Siracusa, M. A.; Guerrera, F.; Vanella, A. *Nitric Oxide-Biology And Chemistry* **2001**, *5*, 32-38.

(64) Siripin, D.; Fucharoen, S.; Tanyong, D. I. *Asian Pac. J. Allergy Immunol.* **2011**, *29*, 102.

(65) Spence, D. M.; Torrence, N. J.; Kovarik, M. L.; Martin, R. S. *Analyst* **2004**, *129*, 995.

(66) Chen, Z.; Li, Q.; Sun, Q.; Chen, H.; Wang, X.; Li, N.; Yin, M.; Xie, Y.; Li, H.; Tang, B. *Analytical Chemistry* **2012**, *84*, 4687.

(67) Yang, Q.; Zhang, X.; Bao, X.; Lu, H.; Zhang, W.; Wu, W.; Miao, H.; Jiao, B. *Journal of Chromatography A* **2008**, *1201*, 120.

(68) Lindström, S.; Mori, K.; Ohashi, T.; Andersson-Svahn, H. *ELECTROPHORESIS* **2009**, *30*, 4166.

(69) McClain, M. A.; Culbertson, C. T.; Jacobson, S. C.; Allbritton, N. L.; Sims, C. E.; Ramsey, J. M. *Analytical Chemistry* **2003**, *75*, 5646.

(70) Wang, Y.; Chen, Z.-z.; Li, Q.-l. *Microchimica Acta* **2010**, *168*, 177.

(71) Sims, C. E.; Allbritton, N. L. *Lab On A Chip* **2007**, *7*, 423-440.

(72) Blaise, G. A.; Gauvin, D.; Gangal, M.; Authier, S. *Toxicology* **2005**, *208*, 177.

(73) Cecala, C.; Rubakhin, S. S.; Mitchell, J. W.; Gillette, M. U.; Sweedler, J. V. *Analyst (Cambridge, U. K.)* **2012**, *137*, 2965.

(74) Mainz, E. R.; Gunasekara, D. B.; Caruso, G.; Jensen, D. T.; Hulvey, M. K.; Fracassi, d. S. J. A.; Metto, E. C.; Culbertson, A. H.; Culbertson, C. T.; Lunte, S. M. *Anal. Methods* **2012**, *4*, 414.

(75) Ye, X.; Xie, F.; Romanova, E. V.; Rubakhin, S. S.; Sweedler, J. V. *ACS Chem. Neurosci.* **2010**, *1*, 182.

(76) Ye, X.; Kim, W.-S.; Rubakhin, S. S.; Sweedler, J. V. *J. Neurochem.* **2007**, *101*, 632.

(77) Kim, W.-S.; Ye, X.; Rubakhin, S. S.; Sweedler, J. V. *Analytical Chemistry* **2006**, *78*, 1859.

(78) Cruz, L.; Moroz, L. L.; Gillette, R.; Sweedler, J. V. In *J Neurochem* 1997; Vol. 69, p 110.

(79) Moroz, L. L.; Dahlgren, R. L.; Boudko, D.; Sweedler, J. V.; Lovell, P. *J. Inorg. Biochem.* **2005**, *99*, 929.

(80) Floyd, P. D.; Moroz, L. L.; Gillette, R.; Sweedler, J. V. *Anal. Chem.* **1998**, *70*, 2243.

(81) Amatore, C.; Arbault, S.; Bouton, C.; Coffi, K.; Drapier, J.-C.; Ghandour, H.; Tong, Y. *ChemBioChem* **2006**, *7*, 653.

(82) Jiang, D.; Sims, C. E.; Allbritton, N. L. *ELECTROPHORESIS* **2010**, *31*, 2558.

(83) Price, A. K.; Culbertson, C. T. *Analytical Chemistry* **2007**, *79*, 2614.

(84) Halpin, S. T.; Spence, D. M. *Analytical Chemistry* **2010**, *82*, 7492.

(85) Li, X.; Chen, Y.; Li, P. C. H. *Lab on a Chip* **2011**, *11*, 1378.

(86) Lion, N.; Reymond, F.; Girault, H. H.; Rossier, J. S. *Current Opinion in Biotechnology* **2004**, *15*, 31.

(87) Phillips, K. S.; Lai, H. H.; Johnson, E.; Sims, C. E.; Allbritton, N. L. *Lab on a Chip* **2011**, *11*, 1333.

(88) Liu, Y.-M.; Zhao, S.; Alterman, M. A.; Hunziker, P.; Walker, J. M., Ed.; Humana Press: 2012; Vol. 828, p 351.

(89) Hosokawa, M.; Hayashi, T.; Mori, T.; Yoshino, T.; Nakasono, S.; Matsunaga, T. *Analytical Chemistry* **2011**, *83*, 3648.

(90) Lai, H.-H.; Quinto-Su, P. A.; Sims, C. E.; Bachman, M.; Li, G. P.; Venugopalan, V.; Allbritton, N. L. *Journal of The Royal Society Interface* **2008**, *5*, S113-S121.

(91) Trouillon, R. l.; Passarelli, M. K.; Wang, J.; Kurczy, M. E.; Ewing, A. G. *Analytical Chemistry* **2013**, *85*, 522.

(92) Kovarik, M. L.; Gach, P. C.; Ornoff, D. M.; Wang, Y.; Balowski, J.; Farrag, L.; Allbritton, N. L. *Analytical Chemistry* **2012**, *84*, 516.

(93) Wu, M.; Perroud, T. D.; Srivastava, N.; Branda, C. S.; Sale, K. L.; Carson, B. D.; Patel, K. D.; Branda, S. S.; Singh, A. K. *Lab on a Chip* **2012**, *12*, 2823.

(94) Li, M. W.; Martin, R. S. *Analyst* **2008**, *133*, 1358.

(95) Reid, K. R.; Kennedy, R. T. *Analytical Chemistry* **2009**, *81*, 6837.

(96) Dishinger, J. F.; Reid, K. R.; Kennedy, R. T. *Analytical Chemistry* **2009**, *81*, 3119.

(97) Greif, D.; Galla, L.; Ros, A.; Anselmetti, D. *Journal of Chromatography A* **2008**, *1206*, 83.

(98) Xu, C.-X.; Yin, X.-F. *Journal of Chromatography A* **2011**, *1218*, 726.

(99) Zhu, L.; Lu, M.; Yin, X. *Talanta* **2008**, *75*, 1227.

(100) Zhang, X.; Li, Q.; Chen, Z.; Li, H.; Xu, K.; Zhang, L.; Tang, B. *Lab on a Chip* **2011**, *11*, 1144.

(101) Yu, L.; Huang, H.; Dong, X.; Wu, D.; Qin, J.; Lin, B. *ELECTROPHORESIS* **2008**, *29*, 5055.

(102) Hargis, A. D.; Alarie, J. P.; Ramsey, J. M. *Electrophoresis* **2011**, *32*, 3172.

(103) Phillips, K. S.; Lai, H. H.; Johnson, E.; Sims, C. E.; Allbritton, N. L. *Lab on a Chip* **2011**, *11*, 1333.

(104) Shah, D. *Biomicrofluidics* **2012**, *6*, 014111.

(105) Culbertson, C. T.; Jacobson, S. C.; Michael Ramsey, J. *Talanta* **2002**, *56*, 365.

(106) Zhu, K.; Leung, K.; Ting, A.; Wong, Z.; Ng, W.; Choi, R.; Dong, T.; Wang, T.; Lau, D.; Tsim, K. *Analytical and Bioanalytical Chemistry* **2012**, *402*, 2805.

(107) Lin, B.; Njoroge, S.; Chen, H.-W.; Witek, M. g.; Soper, S. In *Microfluidics*; Springer Berlin Heidelberg: 2011; Vol. 304, p 203-260.

(108) Reedy, C. R.; Hagan, K. A.; Marchiarullo, D. J.; Dewald, A. H.; Barron, A.; Bienvenue, J. M.; Landers, J. P. *Analytica Chimica Acta* **2011**, *687*, 150.

(109) Horrocks, M. H.; Li, H.; Shim, J.-u.; Ranasinghe, R. T.; Clarke, R. W.; Huck, W. T. S.; Abell, C.; Klenerman, D. *Analytical Chemistry* **2012**, *84*, 179.

(110) Neerincx, P. E.; Denteneer, R. P. J.; Peelen, S.; Meijer, H. E. H. *Macromolecular Materials and Engineering* **2011**, *296*, 349.

(111) Chen, Y.-T. *Microfluidics and nanofluidics* **2011**, *11*, 339.

(112) Schonfeld, F.; Hessel, V.; Hofmann, C. *Lab on a Chip* **2004**, *4*, 65.

(113) Lu, Z. *Sensors and actuators. B, Chemical* **2010**, *144*, 301.

(114) Hossain, S.; Husain, A.; Kim, K.-Y. *Chemical Engineering Journal* **2010**, *162*, 730.

(115) Sunghoon Baek and Simon, S. *Journal of Micromechanics and Microengineering* **2011**, *21*, 077001.

(116) Stroock, A. D.; Dertinger, S. K. W.; Ajdari, A.; MeziÄ‡, I.; Stone, H. A.; Whitesides, G. M. *Science* **2002**, *295*, 647-651.

(117) Jeon, W. *Chemical engineering journal* **2009**, *152*, 575.

(118) Malecha, K. *Sensors and actuators. B, Chemical* **2009**, *143*, 400.

(119) Li, J. M.; Liu, C.; Liu, J. S.; Xu, Z.; Wang, L. D. *Journal of Materials Processing Technology* **2009**, *209*, 5487.

(120) Jian Chen, J.; Ren Lai, Y.; Tang Tsai, R.; Der Lin, J.; Yang Wu, C. *Chemical Engineering Science* **2011**, *66*, 2164.

(121) Howell, J. P. B.; Mott, D. R.; Fertig, S.; Kaplan, C. R.; Golden, J. P.; Oran, E. S.; Ligler, F. S. *Lab on a Chip* **2005**, *5*, 524.

(122) Nguyen, T. N. T.; Kim, M.-C.; Park, J.-S.; Lee, N. E. *Sensors and Actuators B: Chemical* **2008**, *132*, 172.

(123) Miranda, J. M.; Teixeira, J. A.; Vicente, A. A.; Correia, J. H.; Minas, G. In *Engineering in Medicine and Biology Society, 2009. EMBC 2009. Annual International Conference of the IEEE* 2009, p 7034.

(124) Lin, Y.-C.; Chung, Y.-C.; Wu, C.-Y. *Biomed Microdevices* **2007**, *9*, 215.

(125) Ahmed, D.; Mao, X.; Shi, J.; Juluri, B. K.; Huang, T. J. *Lab on a Chip* **2009**, *9*, 2738.

(126) Yang, Z.; Matsumoto, S.; Goto, H.; Matsumoto, M.; Maeda, R. *Sens. Actuators, A* **2001**, *A93*, 266.

(127) Salmanzadeh, A.; Shafiee, H.; Davalos, R. V.; Stremler, M. A. *Electrophoresis*, *32*, 2569.

(128) Yan, D.; Yang, C.; Miao, J.; Lam, Y.; Huang, X. *Electrophoresis* **2009**, *30*, 3144.

(129) Liu, C. *Proceedings - Electrochemical Society* **2003**, *2002-27*, 188.

(130) Lu, L.-H.; Ryu, K. S.; Liu, C. *J. Microelectromech. Syst.* **2002**, *11*, 462.

(131) McDonald, J. C.; Duffy, D. C.; Anderson, J. R.; Chiu, D. T.; Wu, H.; Schueller, O. J. A.; Whitesides, G. M. *ELECTROPHORESIS* **2000**, *21*, 27.

(132) Pelrine, R. E.; Kornbluh, R. D.; Joseph, J. P. *Sensors and Actuators A: Physical* **1998**, *64*, 77.

(133) Macosko, C. W. *Rheology: principles, measurements and applications*; VCH Publishers Inc: New York, 1994.

(134) Price, A. K.; Culbertson, C. T. *Anal. Chem. (Washington, DC, U. S.)* **2009**, *81*, 8942.

(135) Price, A. K.; Culbertson, C. T. *Analytical Chemistry* **2009**, *81*, 8942.

(136) McDaniel, K. J., Kansas State University, 2008.

(137) Soulimane, S.; Al Ahmad, M.; Matmat, M.; Camon, H. In *Thermal, Mechanical and Multi-Physics Simulation and Experiments in Microelectronics and Micro-Systems, 2008. EuroSimE 2008. International Conference on* 2008, p 1.

Appendix A

A.1 Immunoaffinity Chromatography Experiments in Online Format

A fused silica capillary with an internal diameter of 300µm and a length of 30 cm was placed between two pairs of neodymium iron boride rare earth metal magnets (K&J Magnetics, Jamison, PA) arranged in attraction configuration. To do this, the magnets were placed on a 5.08cm x 37.62cm glass slide (Corning Inc. NY). The magnet pairs were glued to the surface using a few drops of superglue and held in place with paper clips until dry. The magnet pairs were arranged so that there was adequate space to fit a fused silica capillary between them. Standard 10:1 ratio poly(dimethylsiloxane), PDMS (Sylgard 184: Dow Corning- Midland, MI) was then poured over the magnets and the rest of the glass slide, followed by baking at 80^{o}C for 1 hr, to cure the PDMS.

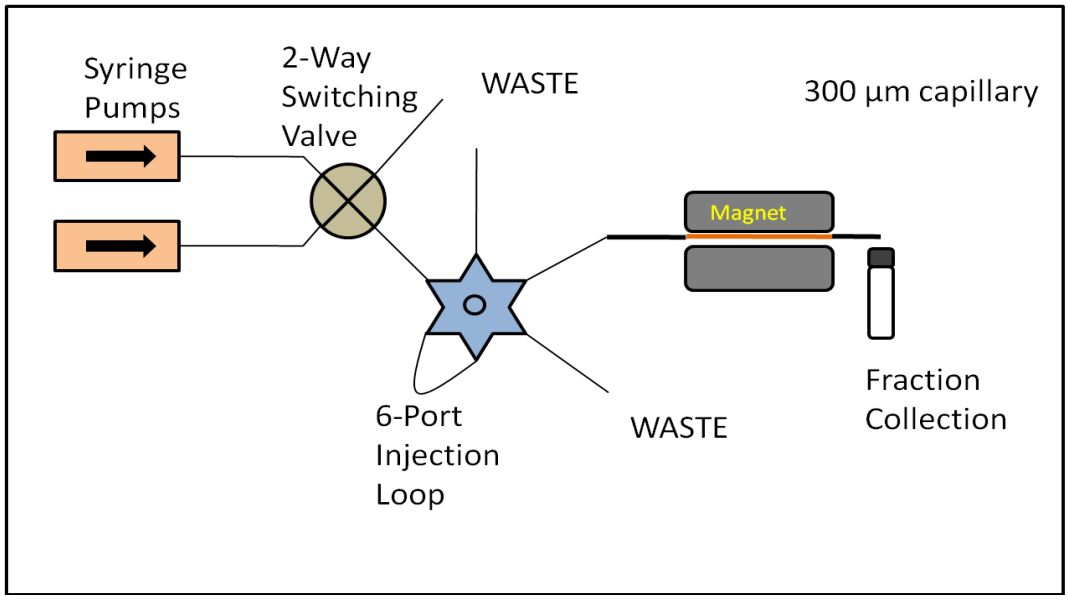

Figure A.1. Schematic diagram of capillary IAC using magnetic beads

A.1.1 Magnetic Beads Column Packing

Packing the column required the use of two syringe pumps, a two way switching valve, and a 6-port manual injector. All these components were connected to each other with PEEK^{TM} tubing (Upchurch Scientific, Oak Harbor, WA). The experimental set up is shown in Figure A.1. First, the capillary was filled with binding buffer (100mM sodium phosphate, 0.01% Tween-20, pH 8.2). Magnetic bead slurry, prepared by diluting the bead suspension fivefold in binding buffer, was placed at the end of the capillary column labeled 'sample collection'. One of the syringes, whose flow was connected to the fused silica capillary, was set to withdrawal mode, with a flow rate of 10µL/min. This way the bead slurry was sucked into the capillary and trapped between the magnets. Once the region between the magnets was fully occupied by beads, the flow was switched back to the forward direction and the column was flushed with the binding

buffer to remove any beads that were not trapped and to get rid of air bubbles. The total length of the magnetic beads column was 2.5cm.

A.1.2 Antibody Binding and Crosslinking

The purified SERPIN-1 antibody solution was injected through the sample injection port on the 6-port injector valve when in loading mode. The handle on the injection valve was switched to injection mode which resulted in the antibody solution being swept into the flow toward the packed column bed. The flow rate was slowed down to 1 µL/min for 20 min so that the antibodies received adequate time to interact with protein A on the beads. The binding buffer was then flushed through for about 10 minutes at µL/min to wash out any unbound antibodies. The flow through was saved for analysis of binding efficiency. The bound antibodies were crosslinked to protein A using a cross linking buffer (200mM triethanolamine pH 8.2) containing 20mM dimethyl pimelimidate (DMP), flowed through the column for 30 minutes, at 10µl/min. This was followed by a 10- minute quenching step using quenching buffer (50mM Tris pH 7.5). The quenching step blocks the sites where the antibody did not bind to. After equilibration with binding buffer, the column was now ready to isolate serpins from samples. To store the column, a storage buffer consisting of binding buffer containing 0.01% NaN_3 was flushed through the capillary. The capillary was then disconnected at the union (Figure A.1) and fitted to vials containing the storage buffer via a rubber septum, and stored at 4^{o}C. Crosslinking the antibodies to the beads ensured that only serpins and serpin protease complex were recovered in the elution process. This way, background from the otherwise large amount of antibody is avoided.

A.1.3 Application of Hemolymph and Subsequent Elution of Bound Proteins

The column was equilibrated to room temperature and binding buffer was flushed through the capillary at a flow rate of 20 µL/min. Frozen hemolymph samples were placed on ice to thaw. If necessary, the samples were diluted with appropriate volumes of binding buffer before application to the column. Next the hemolymph sample was injected at the sample injection valve in the same way as the antibody solution By considering the volume of the plumbing between the injection port and the head of the bead column, it was possible to determine how long the sample plug took to get to the bead column. At this point, the flow rate was switched to 1 µL/min so that the sample plug spent a longer time interacting with the antibody-coated beads. After 30 min, the flow was switched back to 20 µL/min. The flow through was collected at the end of the capillary. The column was then washed for at least 10 min. Aliquots of the wash flow through were collected. Next, the flow was switched to the elution buffer (50mM glycine, pH 2.5). 1 min elution fractions were collected at the end of the fused silica capillary and labeled appropriately. Each of the fractions was neutralized with 1 µL of sodium phosphate, pH 7.4. Finally, the flow was switched back to binding buffer to equilibrate the column. A final rinse with storage buffer was performed before storing the column at 4^{o}C. The fractions collected were analyzed with SDS-PAGE, Western blotting, silver staining and ESI-MS.

A.2 Determination of Binding Capacity of Immunoaffinity Column

The volume of the packed bed, determined by the dimensions of the fused silica capillary and rare earth magnets and information provided by the magnetic beads manufacturer was used to calculate the binding capacity (*B*) of the bead column. The magnetic beads were spherical and

measured 2.8 µm in diameter. The bead concentration was 30 mg/ mL and the binding capacity factor was 8 µg IgG per milligram of beads (information from manufacturer). Equation 2.1 below was used to calculate the theoretical binding capacity of the bead column;

$$B = 0.75\pi r_c^2 l_c \rho B_{cap}$$

where r_c is the capillary radius, l_c is the capillary length occupied by beads, ρ is the density of the beads and B_{cap} is the binding capacity factor. For a column whose length was 1.85 cm, B was calculated as 10.2 µg of human IgG. This translated to 6.8×10^{-11} moles of IgG (MW = ~150 KDa). Since IgG is divalent, it should bind twice the moles of serpin i.e 1.36×10^{-10} moles, which is equivalent to 6.12 µg of serpin (MW= ~ 45 KDa). If the column performed at 50% efficiency, the purified protein eluted would be abundant enough to easily detect with western immunoblotting or mass spectrometry.

The actual binding capacity could only be determined by performing experiments. The degree of binding efficiency was determined by applying known concentrations of recombinant serpin protein to the column and subsequently eluting the retained proteins. The elution fractions as well as washes were then loaded and ran on a gel alongside serpin protein standards. In the initial online experiments, a total of 1.8 µg of purified SERPIN1 antibody were applied and crosslinked to the protein A magnetic beads column as previously detailed in the experimental section. The theoretical binding capacity of this column was calculated as 540 ng of SERPIN1C. In the first experiment, 10 µL of 0.6 µg/ µL of serpin1C protein solution were injected onto the column. This was just over 10-fold of the maximum calculated binding capacity. The flow-through fractions were collected following sample injection and buffer column washing. 2 min elution fractions were collected after applying the elution buffer (100 mM glycine, pH 2.5) at a flow rate of 10 µL/ min. The procedure of loading the column with recombinant protein and then eluting the bound protein was repeated two more times on the same column. SDS-PAGE followed by western immunoblotting was performed on the sample fractions collected. A scan of the western blot membrane of the elution fractions is shown in Figure A.2.

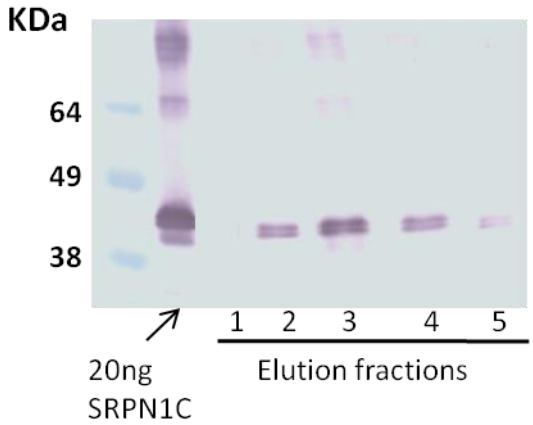

Figure A.2. Analysis of elution fractions from capillary immunoaffinity chromatography column packed with SERPIN-1 antibody coated magnetic beads. The captured and subsequently eluted recombinant SERPIN-1C in the elution fractions (the puprle bands on lanes numbered 1-5) was detected on a Western blot performed with rabbit anti SERPIN-1. column.

The results shown here indicated that antibody was indeed immobilized on the protein A magnetic beads and that the antibody successfully captured recombinant SERPIN-1C from a solution, and the retained protein was subsequently eluted from the beads. It was possible to

reuse the column two more times but the binding efficiency was compromised with increasing number of uses, probably due to prolonged exposure to the low pH elution buffer.

The preliminary experiments with recombinant SERPIN1C demonstrated that purified antibody was crosslinked to protein A on the magnetic beads and that the resulting column was capable of binding detectable amounts of serpin1C from a solution despite the low efficiency. Possible reasons for this low binding capacity included inefficient antibody binding to protein A on the magnetic beads, poor crosslinking of antibody to protein A, and/or non-optimal conditions for the antigen-antibody interactions. However, most immunoaffinity columns have binding efficiencies ranging between 10-100%. Given the small sample size we used, the antibody bound to the beads would be sufficient to isolate detectable amounts of the target proteins.

A.3 Experiments with M .sexta Hemolymph

In the online format, beads were first incubated with the antibody solution in a centrifuge tube followed by crosslinking to protein A, prior to loading the beads onto the fused silica capillary. 10 µL of hemolymph sample was diluted 10 fold. 10 µL of this solution was then injected onto the column and the flow rate reduced to 0.5 µL/min. At this slow flow rate, the hemolymph interacted with the antibody-coated beads longer. All unbound proteins were washed off by flowing 0.1M phosphate buffer at a rate of 20 µL/min for 20 min. The flow was switched to 50 mM glycine-HCl, pH 2.5 and the bound proteins were eluted in 10, 1 min elution fractions. The scan of the silver stain gel (Figure A.3) demonstrated that the immunoaffinity column was capable of purifying and concentrating serpin from hemolymph. This was very encouraging considering the fact that hemolymph was a very complex matrix, as evidenced by the numerous bands in the hemolymph lane in Figure A.3. However, it was evident that the eluted protein diffused over many fractions and this meant that the fractions would have to be larger and more dilute if all the protein was to be collected in fewer fractions.

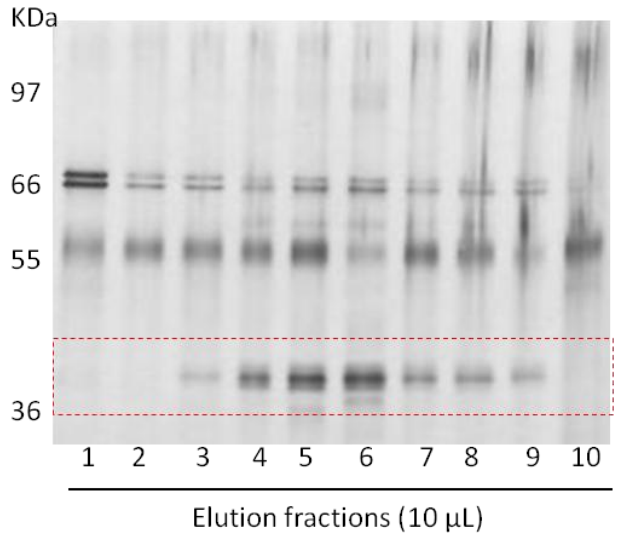

Figure A.3. Silver stain gel of subseequent, 1-min elution fractions following injection and incubation of 1uL of *M. sexta* hemolymph onto antibody-coated magnetic bead column. The lanes marked 1-10 are the elution fractions in that order. The bands in the dotted red box are serpin1 proteins eluted from the column. Fractions 4, 5 and 6 contained the most serpin.

Appendix B

B.1 Experiments with denatured SRPN2 samples

Urea was used as an alternative denaturant to the SDS-containing reducing buffer. 0.4 mL of 8M urea containing 8 µL of β-mercaptoethanol was added to 0.1 mL of SRPN2 (0.4 µg/µL) and incubated at room temperature for 1 h. The sample was then dialyzed into 10mM phosphate buffer. 100 µL of the dialyzed sample was then incubated with ab-coated beads. the bound proteins were then eluted in 20 µL of 0.1M glycine buffer (pH 2.5). SDS-PAGE and western blotting was performed on saved fractions and the resulting membrane is shown in Figure B.1.

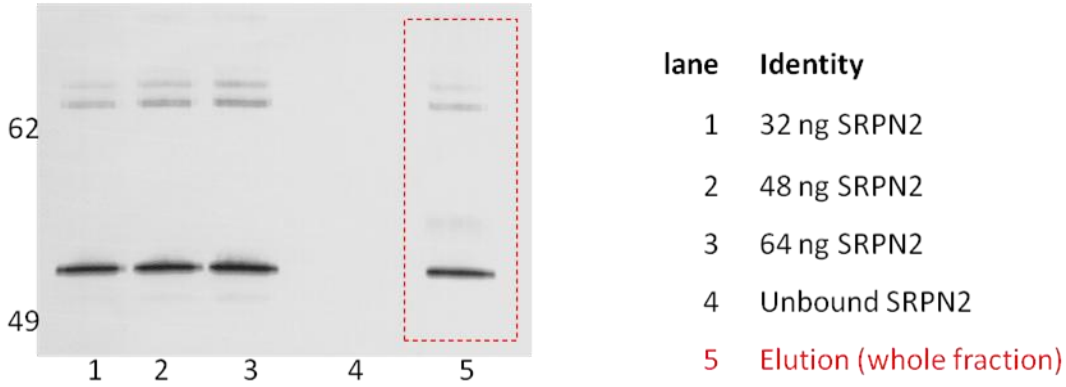

Figure B.1. Western immunoblot membrane of fractions from immunoaffinity experiment with urea-denatured recombinant SRPN2.

An intense elution fraction band was observed (lane 5). This was ~ 20% of the total mass of protein initially applied to the beads. This looked promising and we wanted to verify this finding. We denatured two batches of protein, one with 8M urea only and the other with 8M urea containing β-mercaptoethanol. Samples of the denatured proteins were added to Ab-coated beads and the retained proteins subsequently eluted in 30 µL of 01M glycine buffer pH 2.5. To better estimate how much antibody we were losing following crosslinking, we saved the glycine wash after the quenching the crosslinking reaction. The western blot membrane scan below (Figure B.2) shows the results obtained with 'urea-β-mercaptoethanol' denatured SRPN2;

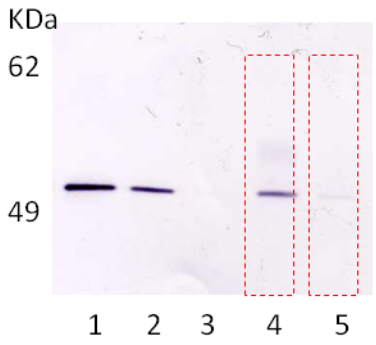

lane	Identity
1	75 ng SRPN2 (denatured)
2	'Urea-β-me' denatured SRPN2 unbound
3	Wash 1
4	Elution 1 (50%)
5	Elution 2 (50%)

Figure B.2. Immunoaffinity experiments with SRPN2 denatured with 8M urea containing β-mercaptoethanol.

It is noted here that most of the antibody initially bound to protein A did not get crosslinked and got eluted during the glycine wash step. This may explain why very little protein is recovered in the elution steps. Experiments with 'urea-only' denatured proteins were not very different in terms of amount of protein in the elution step (Figure B.3).

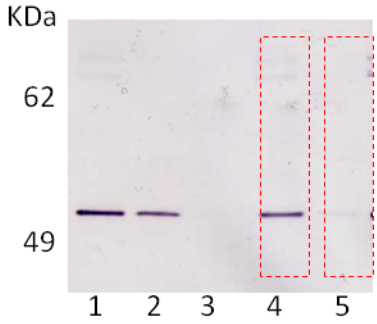

lane	Identity
1	75 ng SRPN2 (denatured)
2	'Urea -only' denatured SRPN2 unbound
3	Wash 1
4	Elution 1 (50%)
5	Elution 2 (50%)

Figure B.3. Immunoaffinity experiments with SRPN2 denatured with 8M urea only.